CHARACTERIZATION OF THE LOCAL MECHANICAL PROPERTIES OF INTERFACES IN HETEREGENEOUS MATERIALS

A Dissertation

Presented to

the Faculty of the Department of Material Science

University of Houston

In Partial Fulfillment

of the Requirements for the Degree

Doctor of Philosophy

in Materials Science and Engineering

by

Jean-Baptiste Giouse

December 2018

CHARACTERIZATION OF THE LOCAL MECHANICAL PROPERTIES OF

INTERFACES IN HETEREGENEOUS MATERIALS

Jean-Baptiste Giouse

Approved:

Chair of the Committee, Pradeed Sharma, Professor, UH Mechanical Engineering

Committee Members:

Ken White, co-advisor, Professor, UH Mechanical Engineering

Robert Vajtai, Associate Research Professor, Rice University

Yashashree Kulkarni, Associate Professor, UH Mechanical Engineering

Krishnaswamy Ravi-Chandar, Professor, UT Austin

Christophe Tromas, co-advisor, Professor, Université de Poitiers

Marc Bird, PhD-PE, Baker Hughes

Ludovic Thilly, Professor, Université de Poitiers

Suresh K. Khator, Associate Dean, Cullen College of Engineering

Alamgir Karim, Professor and Director of the Interdisciplinary Program in Material Science and Engineering

Acknowledgements

Because this work is the results of numerous collaborations, meetings, discussions and exchanges throughout those 4 years, I want to start this dissertation by thanking all the people that helped me and shared their time, help and knowledge with me.

Firstly, I would like to thank my supervisors, Ken WHITE and Christophe TROMAS, for their continuous trust and help. Above all, I want to thank Christophe who accepted to join us later on this program as a co-advisor. Without his efforts, constant support and guidance, I do not think the quality and interest of this work would have been the same. I want to thank Ken for his continuous help and efforts to keep this collaboration alive.

I want to thank Krishnaswamy RAVI-CHANDAR and Robert VAJTAI for accepting to review this dissertation. I also want to thank sincerely Pradeed SHARMA, Ludovic THILLY, Yashashree KULKARNI and Marc BIRD for accepting to be part of my defense committee.

I want also to acknowledge the program LABEX INTERACTIFS, which funded all my travels and stays in Poitiers.

This project has not always been the way it is now. The first year or so has somehow been very unstable and I want to truly thank Ludovic THILLY for continuously fighting for

me and helping me so this project could come to an end (and to a beginning actually). I realize the efforts and time you put into this and I really appreciate it.

Several people generously helped me and made this period of my life a great experience. It is going to be difficult to thank all of them. However, when thinking about those people, Matthieu AUMAND has to come first. We started it together and finished together. At time, it was not that obvious that we will be both standing here, as doctors. So thank you for supporting me in this windowless and depressing basement. Without your presence, this PhD would have definitely been less enjoyable. I want to thank as well all the students (PhD or not) and people who helped me at the University of Houston. It includes Ali KHAMIDALLA, Mejdi KAMMOUN and everyone else who helped in one way or another.

The people of the Prime institute have a special place in those acknowledgements. Even though I only spent 10 months, I can say without a doubt say that my times there were the most enjoyable ones. All the students and staff always welcomed me and helped me the best they could. Among those people, Anne-Marie Archambault comes first. She has been continuously helping me in the preparation of my samples. We spent several hours polishing our samples together and her help has been exceptional. Dominique Eyidi has also been very important as he never refused to help and has been an amazing SEM teacher.

I want to thank Anne JOULAIN, Frederique PAILLOUX, Denis BERTHAUD, David MELLIER, Marc TOULMINET, and Guillaume AMIARD who generously helped on several and various experiments.

I also would like to thank Alicia Lecesve. I spent countless hours in her office talking and talking and talking. Thank you for your constant laughs and thank you for helping me through those infamous administrative rules.

I also thank all the PhD students I met including Ahmed, Max, Florian, Romuald, Julien, Benjamin D., Benjamin B., Thomas, Florent and the others I probably forgot. I will see you very soon hopefully.

Finally, I want to thank all the people I forgot to mention but helped me at one point of my work. As I said in the beginning, this was a collaborative effort and nothing would have been possible without all of them.

CHARACTERIZATION OF THE LOCAL MECHANICAL PROPERTIES OF INTERFACES IN HETEREGENEOUS MATERIALS

An Abstract

of a

Dissertation

Presented to

the Faculty of the Department of Material Science

University of Houston

In Partial Fulfillment

of the Requirements for the Degree

Doctor of Philosophy

in Materials Science and Engineering

by

Jean-Baptiste Giouse

December 2018

Abstract

The notion of "interface" is a universal topic of research in material sciences. Interfaces are responsible for many of the magnetic, electrical, optical and mechanical properties of materials and therefore need to be characterize. The focus of this work is to bring a new understanding of the interfacial mechanical properties of materials by characterizing two industrial components which properties are governed by their interfaces. First, we address the notion of coating and adhesion by characterizing the hardness and microstructure of a 17-4PH steel substrate subjected to a grit blasting surface treatment followed by the deposition of a cermet coating by high velocity oxy-fuel (HVOF). The hardness was characterized using nanoindentation and the microstructure was imaged by optical and electron microscopy. The results showed a strong impact of the surface treatment on the interfacial microstructure and hardness of the substrate revealing a potential weakening of the interfacial adhesion because of it. Then, in light of the results gathered, a similar method was applied to the characterization of an aluminum foam. However, the aluminum foam is a much more complex material and requires a multiscale approach. The structure and microstructures were characterized by several techniques to account for the multiscale nature of the material. Similarly, the mechanical properties were determined by diverse procedures. The results unveil a particularly inhomogeneous material at all scales resulting in non-uniform mechanical properties. The strong interdependence of the macroscopic and microscopic properties is highlighted and gives a better understanding of the mechanical behavior of the foam.

Table of contents

List of Figures

List of Tables

CHAPTER ONE

General introduction

Interfaces are responsible for many of the magnetic, electrical, optical and mechanical properties of materials. The focus of this work is to bring a novel approach in the characterization of the local mechanical properties of interfaces. It was developed based on the assessment that, at a local scale, mechanical properties are inseparable from the microstructure. Therefore, if one wants to determine and understand the nature of these interfaces, an approach coupling both the characterization of the mechanical properties and the microstructure is necessary. A second focus of this work was to apply our approach to concrete cases. Therefore, this work addresses industrial issues and investigates materials commercially available. The benefit of that is the use of "real materials" as opposed to ideal, laboratory samples, which are not necessarily representative. On the other hand, it adds complexity to the study since the materials are not specifically designed for our experiments. It is also important to note that all materials used are proprietary and controlling the manufacturing parameters was not possible. Thus, this work is oriented to the validation of

our method to characterize the local mechanical properties of interfaces rather than optimizing existing processes.

The approach couples nanoindentation cartography and microscopy imaging techniques. First, the notion of coating and adhesion is addressed by characterizing the hardness and microstructure of a 17-4PH steel substrate subjected to a grit blasting surface treatment followed by the deposition of a cermet coating deposited by high velocity oxy-fuel (HVOF). Thermal spraying by HVOF involves high kinetic energy of the powder particles producing high quality coatings with low porosity (typically 1% and below), little oxidation and superior adhesion to the substrate. Cermet Cr_3C_2-NiCr coatings are resistant against corrosion and abrasion and can operate at relatively high temperatures up to 900°C. The material used in this work is used to protect metallic parts against wear and corrosion damages in extreme mechanical and chemical environments. Prior to deposition of the coating, substrate surface modification treatments, such as grit blasting may optimize the local roughness to favor the mechanical interlocking of the coating. This common surface treatment sends high velocity particles (usually angular shaped alumina or silicon carbide grit) onto the substrate surface in order to cause impact damage. Grit blasting with alumina particles offers a conventional substrate surface preparation method intended to improve the adhesion of thermal spray coatings. However, the associated microstructural modifications to the substrate may, in fact, reduce the integrity of the interface. The nanoindentation cartography method was used in cross section to correlate the microstructural modifications

induced by the grit blasting to the resulting local mechanical properties of the substrate in the vicinity of the interface.

The characterization of a "simple" interface, i.e. a bi-material interface, is fairly straightforward since the interface is defined as the separation region between the two dissimilar materials. However, some materials present more complex structures with various interfaces of different nature. One characteristic example is cellular materials. The term "cellular material" includes metallic foams, which possess a macroscopic cellular structure and low density, due to their high porosity, which give them interesting thermal, mechanical and electrical properties. They are versatile materials which applications range from structural components for the automobile industry to architectural and design applications of facades. The mechanical properties of aluminum foams are defined by the cellular structure as well as by the parent material properties of the foam. Many studies were conducted to identify the mechanical behavior of metallic foams relative to their relative density or chemical composition. Yet, it continues to be a challenge as manufacturing a foam remains an imprecise process, which lacks the ability to make foams of a constant quality with pre-defined parameters. Therefore, metallic foams are very complex materials and requires a sophisticated multiscale approach. The metallic foam in this work is mainly used in multilayer composite for its energy absorption properties. Various techniques were used to account for the multiscale nature of the material and a complete procedure was developed to assess the mechanical properties of the foam. The structure and microstructures were characterized by several techniques including X-ray tomography, scanning and transmission

electron microscopy. The compressive behavior was characterized by uniaxial compression and in situ X-ray tomography. The local mechanical properties were also investigated by nanoindentation cartography and by looking at the crystallographic defect within the cell walls. The results unveil a particularly inhomogeneous material at all scales resulting in non-uniform mechanical properties. The strong interdependence of the macroscopic and microscopic properties is highlighted and gives a better understanding of the mechanical behavior of the foam.

The first chapter reflects the two materials studied and present fundamental knowledge associated with both. The second chapter provides a detailed record of the procedures that were followed when completing the experiments discussed in the dissertation. The third chapter presents the results of the characterization of the 17-4PH steel substrate coated with the cermet Cr_3C_2-NiCr coating. The characterization includes microstructural observations of the substrate, coating and interface as well as measurement of the hardness by the nanoindentation cartography method. The impact of grit blasting and coating deposition on the substrate are discussed and in the light of the results presented, the role of grit blasting on the adhesion is discussed as well. The fourth chapter presents the results of the characterization of the aluminum foam. It is divided in three sections. One section is focused on the characterization of the structure and microstructures while the other is focused on the characterization of the mechanical properties. Finally, in light of the results presented, the relationship between the microstructural properties (microstructure and mechanical properties) and the macroscopic behavior of the foam is examined.

Finally, a conclusion summarizes the important results and proposes interesting perspectives capable of completing this work.

CHAPTER TWO

Bibliography

The first chapter reflects the two materials studied and presents fundamental knowledge associated with both. The first part of this chapter addresses the notion of the coating and adhesion. The fundamentals of the HVOF deposition process and the coating structure are first presented. Then, a review of the current knowledge of the impact of grit blasting on the properties of the substrate and the mechanisms of adhesion is presented. The second part presents the current understanding of aluminum foams. Important microstructural features of the aluminum alloys and matrix metal composites are presented followed by a presentation of the foams from their manufacture to the characterization of their mechanical properties.

1. Introduction to interfaces

1.1. Understanding interfaces

The notion of "interface" is a universal topic of research in material sciences. From welding of alloys to the diffusion processes in the membrane of a cell, every object or material

must, at all length scales, deal with the concept of interface. An interface is defined as the region where two chemically dissimilar materials or structurally dissimilar materials (phases) interact with each other. A surface is a special form of interface where one of the medium is the surrounding atmosphere. Therefore, interfaces must always exist in real materials. Further, interfaces contribute to the magnetic, electrical, optical and mechanical properties of materials. Modern interface science is mainly focused on the micro and nanoscale issues associated with atomic rearrangements along grain and phase boundaries and the associated diffusion processes.

An interface is often represented as a plane where two dissimilar materials connect at an atomic level but as defined by P. Delmon [1], the reality is much more complex. In most systems, the actual interface needs to be understood as a transition zone where some of the properties are significantly different compared to those of the bulk (**Figure 2-1**). The size of this transition region can be limited to a few atomic planes in the case of grain boundaries or hundreds of microns in the case of diffusion-controlled processes. The mechanical properties of the interphase region differ from those of the bulks and are critical for the overall mechanical properties of the composite material [2]–[4] since the interphase region governs the load transfer from one phase to another. The interphase is also a preferential site for failure when the material is subjected to mechanical loading [5].

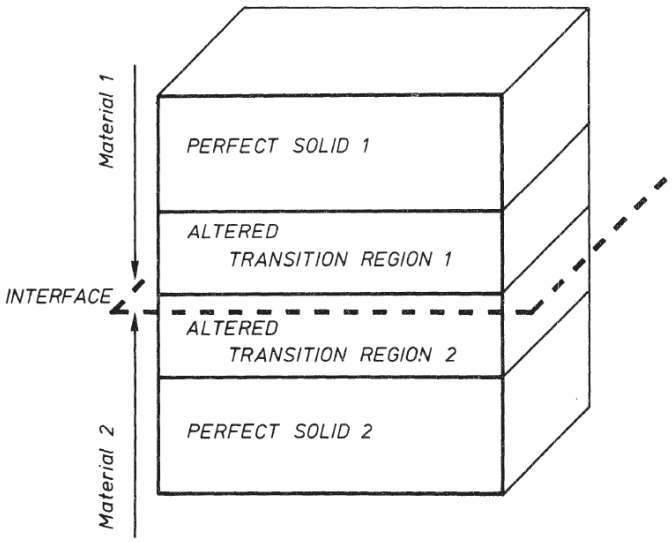

Figure 2-1. Interface and transition regions in materials [6]

1.2. Characterization of interfaces

With access to increasingly smaller scales of observation and characterization, interfaces have taken a prominent place in defining materials properties. For instance, it was only thanks to the increase of resolution of microscopes that scientists have been able to observe and understand the importance of the lipid bilayer structure of cell membranes [7]. More related to the topic of this study, the development of new imaging and characterization techniques such as scanning probe microscopes or nanoindentation have also given scientists access to a new scale of comprehension where small scale phenomenon clarify macroscopic behaviors [8]–[11].

It is important to note that the characterization of interfaces is often more challenging than characterizing surfaces. Firstly, because of the structure itself of an interface, it can be difficult to have access to a 3D characterization and often, only one "side" is observable.

Also because several mechanisms of different nature are responsible for the formation of an interface. The example of the adhesion mechanisms of a thermally sprayed coating on a substrate is indicative of this complexity. Indeed, both mechanical and chemical bonding mechanisms occur in the formation of a strong coating/substrate interface through the role of substrate roughness but also through diffusion-controlled mechanisms. In this particular case, different techniques, each of them having specific constraints, need to be used to obtain a full characterization and understanding of the adhesion mechanisms. Moreover, the measurements of mechanical or electric properties could be desired and would add to the complexity of the characterization of the interface.

Imaging an interface can be challenging because it requires careful preparation to preserve the integrity of the material. In a lab environment, common procedures include cutting and embedding in a resin the sample to expose the interface (investigation are often performed in cross section) followed by successive steps of grinding and polishing to reveal the microstructural details of the surface. However, every material behaves differently during polishing and specific constraints are associated with the characterization techniques employed. Developing distinct preparation procedures is therefore required.

In terms of imaging, scanning electron microscopy (SEM) is the most common tool. It gives the experimenter an easy access to high-resolution details of the interfaces at low and high magnifications. However, the preparation of the surface for SEM imaging is not straightforward and, as mentioned in the previous paragraph, demands attention.

Qualitative information about the topography and composition of the interface are also accessible through this technique. X-ray based techniques such as tomography and diffraction are also useful because they are nondestructive and, because X-rays penetrate deeper into the material, a higher volume is scanned.

Nowadays, interfaces are studied through powerful modeling methods [12]–[14] leading to a better understanding of the fundamental mechanisms of formation of interfaces. It also delivers predictions for optimized thin film structures and coatings without the need of complex experiments. However, such modeling techniques are often limited to ideal cases and experimental observations are necessary to verify and drive the simulations.

The characterization of the mechanical properties followed the same development and most of the efforts are now oriented towards the local mechanical properties of interfaces [15]–[17]. Researchers developed specific procedures and apparatus to investigate the mechanical properties and only test the contribution of the interface. In fiber reinforced composites, it is common to pull out individual fibers to quantify the shear strength of the fiber/matrix interface [18], [19]. In the field of coatings, several tests were developed to measure the cohesion or adhesion strength of the interface [20]–[22]. More recently, instrumented indentation, i.e. nanoindentation, has been employed to characterize the hardness and modulus of interfaces [23], [24]. In recent years, nanoindentation grew into a powerful and conventional technique to characterize interfaces.

2. The HVOF process

The fundamentals of the HVOF process will first be discussed followed by a presentation of the associated adhesion mechanisms. Finally, the discussion will focus on the grit blasting process and its impact on the adhesion of the coating.

2.1. Fundamentals

A coating lifetime is often limited by the failure of the coating/substrate interface. The vicinity of the interface is therefore a subject of intense investigations to understand the mechanisms of adhesion and develop new coatings having extended lifetime. Several techniques exist to deposit one material on top of another producing coating as thin as few atomic layers up to few millimeters.

Thermal spray processes allow the deposition of non-metallic coatings on the surface of a material, mainly steel, to enhance its anti-wear and anticorrosion properties. It relies on the projection at high temperature of melted or semi-melted powder or wire form materials to cover the surface of a substrate. Among the thermal spraying processes, HVOF is very recent as it is commercially available since the 1980's and the development of the Jet Kote HVOF spray system by the Browning Engineering Co in the U.S.A. The main advantages of HVOF over other spraying systems are the high speeds and moderate temperatures achievable, leading to very dense coatings with very low porosity (less than 1%). It is also widely used for deposition of cermet materials, which requires high velocities and temperatures.

A schematic of the HVOF system is shown **Figure 2-2**. Oxygen and the fuel gas (hydrogen, propylene, propane or kerosene) are introduced together inside the combustion chamber. Ignition inside the chamber initiates the combustion and the exhaust gas, formed by a nozzle, pass through the barrel and emerge in the open atmosphere [25]. The coating material is in a powder form and is injected inside the accelerated stream of exhaust gas.

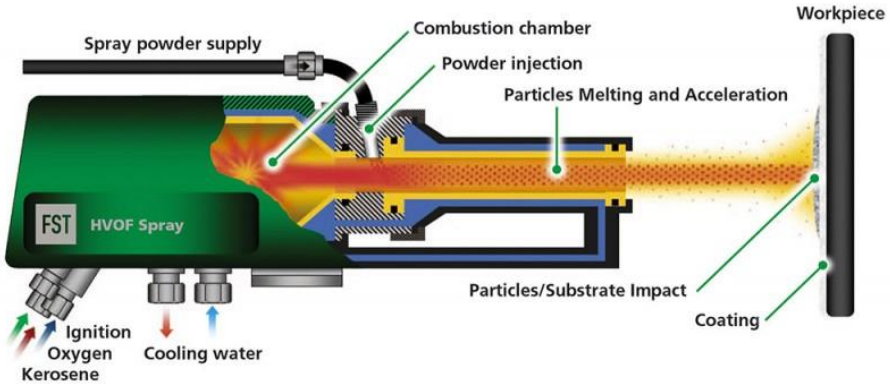

Figure 2-2. Schematic of the HVOF system [26]

2.2. Coating deposition

Coating is build up from molten or semi molten particles striking the substrate surface and forming splats. Some incoming particles remain solid but are detrimental for the coating performance as they are usually poorly bounded to the coating. The coating structure and microstructure result directly from the deformation and solidification of the impinging particles. If the incoming particles remain too cool to deform plastically, the local microstructure will suffer an inhomogeneous void or low strength region. Numerous parameters influence the final microstructure of the coating. Obviously, the gun parameters are essential as they control the speed and temperature of the particles. The substrate

temperature and roughness are important, as they will influence the deformation and solidification of the particles. **Figure 2-3** clearly summarizes the parameters controlling the formation of the interfacial zone. The contribution of chemical and mechanical interactions to the adhesion is also highlighted.

Adhesion mechanisms can be of various origins: mechanical, physical and chemical. Physical interactions comprise van der Waals forces while chemical interactions comprise metallurgical interactions between the coating and the substrate. But both have been proven to contribute little to the adhesion of the coating [25], [27], [28]. On the other hand, mechanical interaction between the coating and the substrate is crucial. Mechanical interaction is the result of the interlocking of the particles to the asperities of the substrate surface as shown on **Figure 2-3**. Substrate roughness is probably the most important and commonly studied parameter governing adhesion between the coating and the substrate. It can be optimized using blasting or chemical methods. It is specifically designed to improve the mechanical interaction of the coating and substrate.

The next section will discuss the impact of grit blasting on the substrate, in terms of roughness modification of course but also in terms of other effects associated with blasting a surface with high kinetic energy particles.

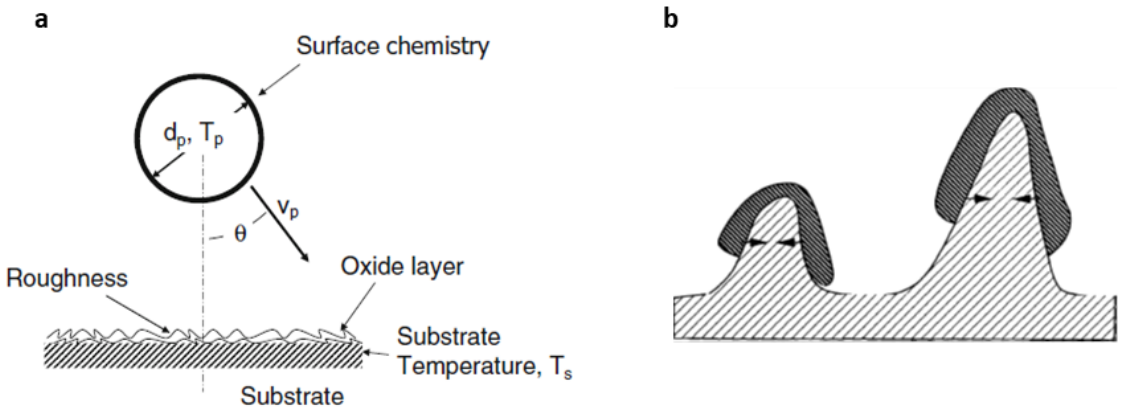

Figure 2-3. (a) Impacting particle and substrate parameters controlling particle flattening and solidification [27] (b) Mechanical anchorage of splats to irregularities of the substrate surface [25]

2.3. Impact of grit blasting on substrate roughness and microstructure

Before deposition of the coating, surface modification treatments like grit blasting are used on the surface substrate to prepare the surface for the deposition of the coating. It consists in sending high velocity particles (usually angular shaped and usually alumina or silicon carbide grits) onto the surface of the substrate in order to modify its surface properties. The main purpose is to optimize the roughness to favor the mechanical anchoring of the coating particles onto the substrate surface. However, the modification of roughness also goes along with a modification of microstructure and stress state of the subsurface. Additionally, despite the surface being flame cleaned after blasting, the presence of residual embedded particles has been observed [29]–[31].

Optimizing the roughness of the substrate surface to improve adhesion is the main reason for grit blasting. Several authors have quantified the effect of roughness on the adhesion [27], [32], [33]. In [33], Wang et al. studied the effect of roughness for a molten NiCrBSi coating

and a solid/liquid two phases WC-Co cermet coating. Both coatings were deposited on mild steel substrates of different roughness. The modification of roughness was achieved by both polishing (for low roughness) and sandblasting. The adhesion of the coating was measured using a standard pullout test. It is shown that the adhesion start increasing for Ra= 1.7μm and the adhesion is almost doubled when Ra=10μm.

Fauchais et al. [27] conducted a review of the formation of splats on low and high roughness for different coating/substrate systems (inferior or superior to Ra=0.2μm respectively). Their conclusion is similar to Wang et al. in that adhesion increases with increasing roughness. For low roughness, physical and chemical adhesion mechanisms are promoted. On the other hand, for high roughness, the flattening of the droplets is limited by the asperities, resulting in smaller and thicker splats. Mechanical interlocking is then the primary mechanisms for adhesion as shown on **Figure 2-3b**. Physical bonding can also be promoted because of the increased surface area associated with higher roughness.

In addition to optimizing the roughness, a compressive residual stress layer is often formed in the subsurface region. Microstructural changes due to sandblasting have also been reported [34]–[39]. This modified layer has a substantial effect on wear, corrosion and fatigue properties. Wang and Li [39] reported substantial increase in wear and corrosion resistance of a sandblasted 304 stainless steel substrate compared to non-grit blasted specimens. A similar trend was observed on the high cycle fatigue strength of pure Ti modified by sandblasting while Hanlon et al. reported a decrease of fatigue crack growth properties in

the case of ultra-fine crystalline Ni. The resistance of certain materials to fatigue crack initiation and propagation is known to be influenced significantly by grain size [40]. A finer microstructure is usually associated with higher strength and therefore is less sensitive to fatigue crack initiation (see **Figure 2-4a**).

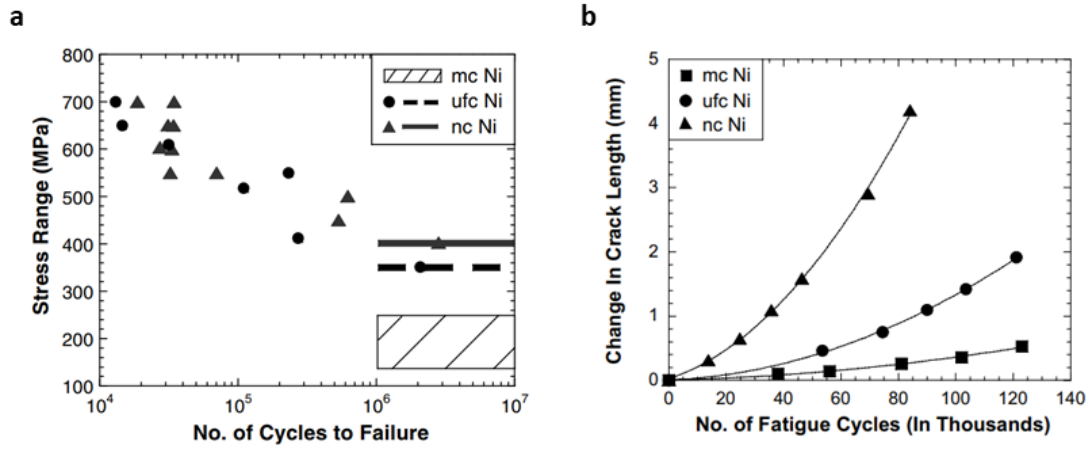

Figure 2-4. A comparison of fatigue properties for nanocrystalline (grain size < 100nm), ultra-fine crystalline (grain size ranging from 100nm to 1μm) and microcrystalline (grain size > 1μm) pure Ni. (a) S–N fatigue response showing the stress range versus number of cycles to failure. The endurance limit for MC pure Ni is way below the one of UFC and NC pure Ni. (b) A comparison of the variation of fatigue crack length as a function of the number of fatigue cycles. The crack fatigue crack length increases at a much faster rate with fatigue cycling in the NC Ni than in the UFC or MC Ni under identical loading conditions [41]

Moreover, the surface compressive stresses usually induced along with the microstructure refinement increase the crack initiation resistance and decrease the crack propagation rate. On the other hand, a coarse microstructure offers an increase of fatigue crack growth compare to a finer one (see **Figure 2-4b**) because a finer microstructure become more sensitive to flaws and defects in the metals, leading to catastrophic propagation of the crack once a microcrack initiates from the flaws [42].

Inducing a nanocrystalline layer is not the main purpose of the grit blasting and other methods are more efficient to achieve that. Most of the literature revolves around SMAT or shot peening processes where the main goal is to develop a nanocrystalline layer at the surface of the material to improve the surface properties of a material. Nevertheless, the mechanisms involved in the SMAT and shot peening processes are similar to those involved in grit blasting. All surface preparation techniques involve high strains at very high strain rates, inducing a large amount of defects in the material.

In the case of grit blasting used prior to a coating deposition, the refinement of microstructure must be taken into account. Indeed, the refinement of microstructure is usually associated with an increase of hardness. The hardness of the substrate is an important parameter for adhesion as it often corresponds to an increase of brittleness and modifies how the splats behave when impinging the substrate. Gao, et al. conducted a study on the influence of hardness on the deposition of single coating splats. Here, deposited cermet WC-Co coatings on steel and Ni based substrates emphasize the contribution of deformation of the substrate toward adhesion mechanisms, especially for hard coatings like Cermet ones. For soft substrates like stainless steel ones, sufficient deformation is achieved to promote adhesion. However, for Ni based substrates, corresponding to higher hardness than the stainless steel substrates, deformation may not be sufficient, as the particles rebound elastically from the substrate surface. Trompetter et al. [43] also studied the effect of substrate hardness on the deposition behavior of a NiCr coating using HVAF. They demonstrate that soft substrates presented more solid particles while hard substrates

presented a higher amount of molten or semi-molten particle. Indeed, in the case of a coating particle impinging a soft substrate, the kinetic energy of the particle is converted mainly into strain energy that will drive the plastic deformation of the surface. On the other hand, when a coating particle impinges a hard substrate, the kinetic energy will be more likely converted into heat energy, hence the higher number of molten and semi-molten particles.

After the blasting process, the roughened substrate is cleaned. However, some researchers have shown that blasting materials remain on the substrate. Those particles are adhered or embedded in the substrate surface. In the case of adhered residual grits, they degrade the adhesion of the coating by modifying the wetting properties of coating particles, creating thermal residual stress because of the thermal mismatch between the substrate and the grit residues and by blocking any interactions between the coating and the substrate. Embedded residual grits result from an important deformation of the substrate overlaying the grit, thereby imposing a complex stress state around this particle.

Summary of the HVOF system

Depositing a coating using HVOF offers very high deposition speeds and produces relatively dense coatings with low porosity. Grit blasting is the primary method to prepare the substrate surface before deposition as it favors the mechanical interaction between the substrate and the coating by modifying the substrate roughness. However, one drawback is its impact on the substrate mechanical properties and microstructure. Grit blasting involves high kinetic energy particles affecting the substrate surface. Therefore, high stresses and

strains are induced in the substrate. It leads to a complex compressive stress state as well as grain refinement similar to what is observed during severe plastic deformation. Moreover, the process leaves residual particles that can be embedded in the substrate surface. Several articles assessed this problem and described the detrimental effect on the fatigue properties in titanium alloys used for prosthesis. It was shown that those particles decrease the fatigue life by acting as preferential crack nucleation sites.

Therefore, an accurate characterization and understanding of the impact of grit blasting on the mechanical properties of the substrate at the interface is important to shed a light on some of the parameters controlling the coating/substrate adhesion.

3. Al-Si alloys

Aluminum-Silicon alloys are used for many industrial applications because of their excellent casting properties. As part of this work, an aluminum foam made of an A359 Al-Si-Mg alloy was characterized. The foam was manufactured using the melt gas injection process that will be explained in a following section. This process is associated with particular solidification conditions and requires the addition of insoluble particles resulting in unconventional alloys and microstructures leading to specific elastic, plastic and fracture behaviors.

Because of that, it seems appropriate to give some elements of understanding about aluminum alloys and their microstructures as well as about the mechanisms of formation of

the microstructures that will be later observed in aluminum foams. For that, the role of alloying elements in aluminum alloys and more specifically Al-Si alloys is addressed. Then, the microstructure of such alloys is presented followed by a review of the refinement mechanisms in Al-Si alloys. Finally, the role of the addition of insoluble particles will be addressed by reviewing the formation of the microstructure of metal matrix composite (MMC) materials made of casting alloys.

3.1. Alloying elements in aluminum alloys

Silicon is the second most common impurity in aluminum after iron, due to its high concentration in bauxite through silica and silicates. The addition of silicon in aluminum reduces its melting temperature and increase its fluidity which make Al-Si based alloys the most used aluminum alloys for casting and welding. Additionally, Si solidifies primarily into a pure silicon phase, which imparts very good wear properties to the alloy. Therefore, they have replaced ferrous alloys in numerous applications in the automotive, aerospace or transportation industries for structural components where costs and weight are critical.

Other impurities and alloying elements have an effect on the microstructure and properties of Al-Si alloys. Iron is the main impurity in aluminum alloys and is well known for increasing casting defects by the formation of Fe-rich intermetallic phases [44]. It is difficult to remove and its concentration is kept as low as possible. Titanium or various combinations of titanium and boron are identified as grain refiners of the α-Al phase [45], [46]. Manganese as well as other elements are used for their beneficial effect on casting defects

because of their interaction with Fe-rich intermetallic phases [47], [48]. As indicated by Mondolfo [49], copper is added to increase the strength and fatigue resistance of the alloy at the expense of the corrosion resistance. Zinc has a minor impact on the properties aluminum when used alone and Al-Zn alloys have quickly been replaced by Al-Cu alloys [49]. An increase of the coefficient of thermal expansion was observed in Al-Zn alloys because of the lower CTE of zinc ($\approx 39.10^{-6}\,°C^{-1}$) compared to aluminum ($\approx 23.10^{-6}\,°C^{-1}$) [50]. The addition of Zn shows greater influence when associated with Mg or Cu as it modifies the precipitation and age hardening properties [51], [52]. Other elements like phosphorus and strontium can be added for their modification of the shape and distribution of the eutectic Si phase.

Magnesium is a very important alloying element in the Al-Si alloy system (as well as Cu) because of its beneficial effect on tensile and creep properties. The presence of Mg makes the alloy responsive to heat treatments by precipitation hardening mechanisms. When a certain amount of Mg is added, precipitates Mg_2Si would form in the Al matrix. The effect of magnesium is very significant on the mechanical properties and the ageing process needs to be accurately controlled for optimal properties. **Figure 2-5** shows the effect of ageing time on the hardness for two Al-Si-Cu and Al-Si-Mg alloys. The curves reveal a sharp increase of hardness until a peak is reached for 7h of ageing. The hardness then decreases to reach a plateau corresponding to the formation of the equilibrium βMg2Si precipitates. The plateau value is about 50% higher than the hardness before ageing.

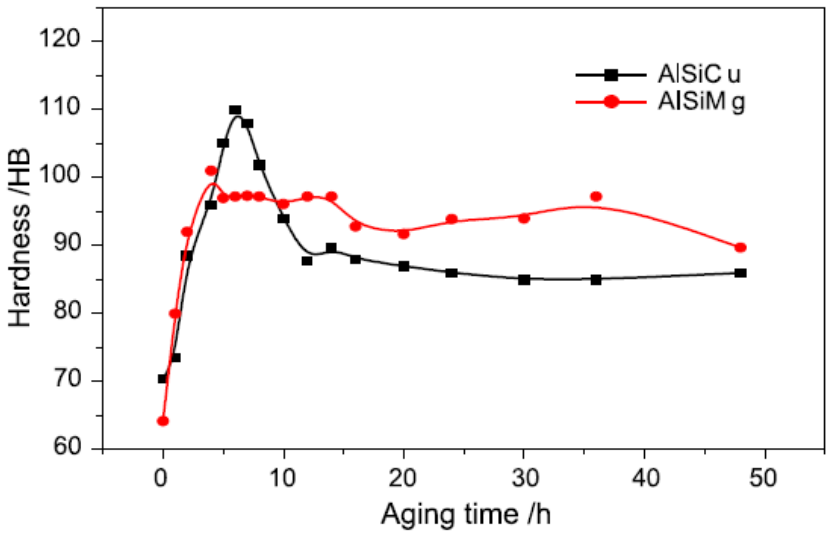

Figure 2-5. Age-hardening curves of Al–Si–Mg and Al–Si–Cu alloys aged at 175°C [9]

The precipitation of Mg is very similar to the one of Cu observed in Al-Cu alloys (duralumin) simultaneously by Guinier and Preston in 1938 [53], [54]. However, the precipitation sequence of Al-Si-Mg alloys is not completely understood and has been extensively investigated. Disagreements exist about the clustering process of Mg and Si during the first stage of ageing. Edwards et al. proposed a sequence that is now accepted as a reference. Yet, the author specifies that the alloy used in the study is different from other authors [55] and therefore could explain the different precipitation sequences proposed in the literature. The precipitation process proposed by Edwards et al. is as follow:

Al Solid Solution	$\rightarrow$	Clusters of Si atoms Clusters of Mg Atoms	$\rightarrow$	Dissolution of Mg atoms	$\rightarrow$	Formation of Mg/Si co-clusters	$\rightarrow$
Precipitates of unknown structure	$\rightarrow$	β'' precipitates	$\rightarrow$	B´ and β'' precipitates	$\rightarrow$	βMg_2Si precipitates	

with B´ and β˝ being the unstable phases and β the equilibrium phase. B´ precipitates forms concurrently to β´ but possess different shape and crystallographic characteristics and formed predominantly in the 6061 alloy studied by Edwards et al. hence the presence of B´ in the precipitation sequence.

3.2. Solidification and phase diagram

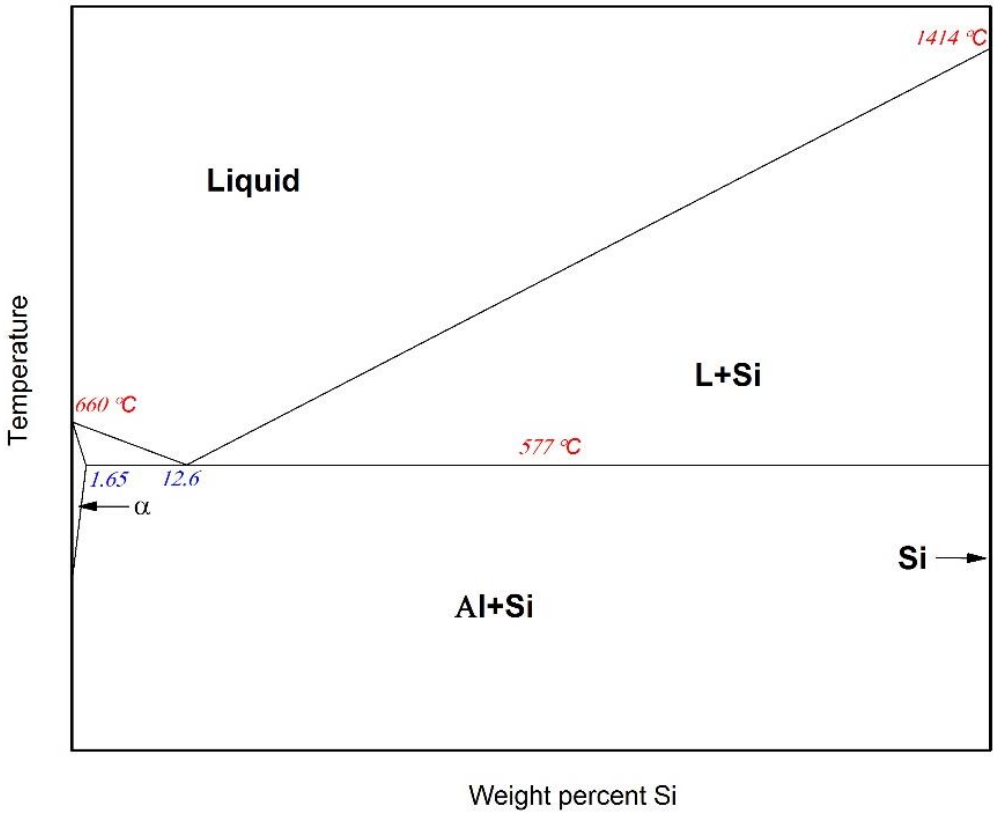

Figure 2-6. Schematic phase diagram of the Al-Si binary alloy

The phase diagram of the binary Al-Si system is a simple eutectic one and is shown in **Figure 2-6**. The eutectic temperature is 577°C and the eutectic point is at 12.6 wt.% of Si. There are hypoeutectic and hypereutectic alloys depending whether they have a Si

concentration below or above the eutectic point respectively. The maximum solubility of Si in Al is 1.65 wt.% of Si at the eutectic temperature and fall down to 0.05 wt.% of Si at 300°C [56]. The solubility of Al in Si is close to zero with a peak of 0.016 wt.% of Al at 1190°C.

Hypoeutectic Al-Si alloys solidify by precipitation of primary α-Al dendrites while hypereutectic alloys form primary Si crystals. In hypoeutectic alloys, the dendrites grow along the <001> directions. The dendritic structure is characterized by a primary dendritic arm along which several secondary and ternary arms can grow along the <001> directions. The size of the dendrite is associated to the secondary dendrite arm spacing (SDAS). **Figure 2-7** shows the SDAS and an optical micrograph of the dendritic structure in an Al-Si-Mg alloy.

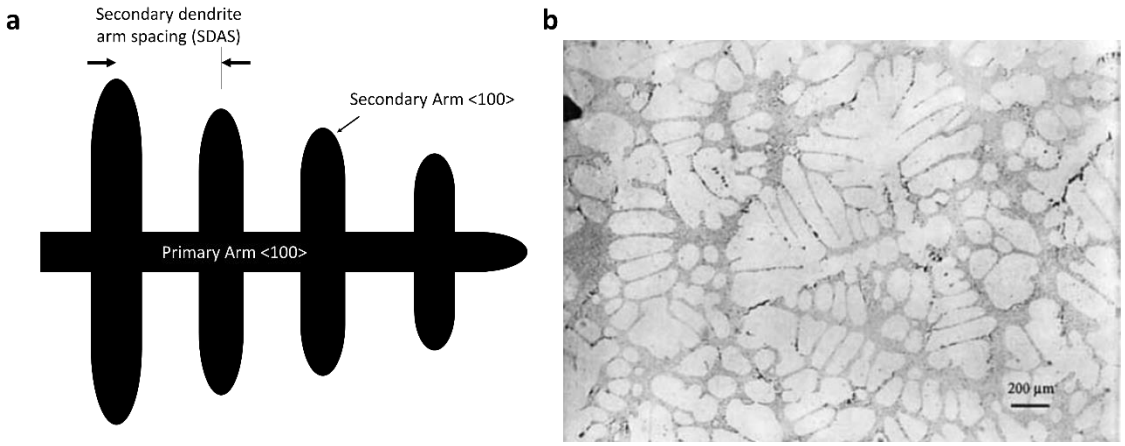

Figure 2-7. (a) Schematic representation of a dendrite with secondary dendrite arms spacing (SDAS) (b) Dendritic structure in an Al-7%Si alloy [57]

The solidification continues with the formation of a eutectic Al-Si phase. During the eutectic solidification, two phases of Al and Si precipitate simultaneously from the liquid at

constant temperature. For silicon contents below and above the eutectic point, the eutectic phase precipitates in presence of primary aluminum and primary silicon crystals respectively. For an alloy at the eutectic concentration (12.6 wt.%), the eutectic phase nucleates from the liquid phase.

Several microstructural features affect the ductility of aluminum castings. The ductility is known to be sensitive in various degrees to the dendrite cell size and silicon particle size. Those two features can be tailored through different process parameters.

3.3. Microstructure refinement in Al-Si alloys

3.3.1. Primary aluminum modification

The effect of SDAS on the mechanical properties has been intensively investigated in the literature [58], [59]. It has been shown to have favorable effects on the ductility by inducing a fracture mode transition from a transgranular fracture at high SDAS to an intergranular fracture mode at low SDAS corresponding to higher ductility [60]. Refining the microstructure is also favorable through a grain boundary strengthening similar to the Hall-Petch mechanism.

Refinement of the dendritic structure is achieved by three means:

- Thermal method by adjusting the solidification rate
- Chemical method by adding refiners into the melt
- Mechanical method by agitating the melt during solidification

Thermal modification is achieved by increasing the solidification rate. The effect of cooling rate has been observed from the 1920's by comparing the microstructure of sand and iron cast alloys [61]. The iron cast alloy corresponding to higher cooling rates exhibited a finer microstructure compared to its sand cast counterpart. Following those observations, several studies have confirm this dependence [62], [63]. The mechanism explaining the refinement of the dendrite is to be found on the effect of the cooling rate on the diffusion of solute element during solidification. For high cooling rates, there is not enough time for the atoms to diffuse to the solid/liquid interface and therefore the coarsening of the dendrites does not happen. By stopping the coarsening process of the primary structure, more dendrites form leading to a finer microstructure after solidification.

Chemical modification is achieved by the use of chemical modifiers. Titanium and boron are the main inoculants with Al-Ti-B master alloys added to the melt. The exact mechanisms are different depending on the nature of the master alloy and the Ti/B ratio [45], [46]. However, the main idea is that the presence of those modifiers increase the number of nucleation sites during solidification, which leads to a higher grain density and smaller grains.

Modification by agitation relies on the agitation of the melt during solidification. It can be achieved through mechanical or electromagnetic stirring. The effect of stirring is double and it would seem that the change of flow induced by stirring the melt change the

direction of growth of the dendrites. Additionally, it has been shown to cause fragmentation and transportation of dendrites into the melt [64], [65].

3.3.2. Eutectic Si modification

Silicon is introduced into aluminum alloys not only because of its solubility in (Al), but also due to the formation of the Al-Si eutectic microstructure, which defines many of the Al–Si alloys properties. The Si eutectic particles exhibit two morphologies: a so-called unmodified morphology made of coarse acicular particles and a modified morphology made of fine round particles. The main interest of the transition from unmodified to modified morphology is the increase of the mechanical properties of the alloy, such as fracture toughness and ductility [60], [66], [67], associated with the fibrous particles.

The eutectic silicon phase can be thermally and chemically modified. Although the two methods give similar silicon morphologies, it is important to note that the growth mechanisms are different. Makhlouf and Guthy proposed a very well documented and complete historical review of the growth mechanisms of Si particles for thermally and chemically modified alloy [68].

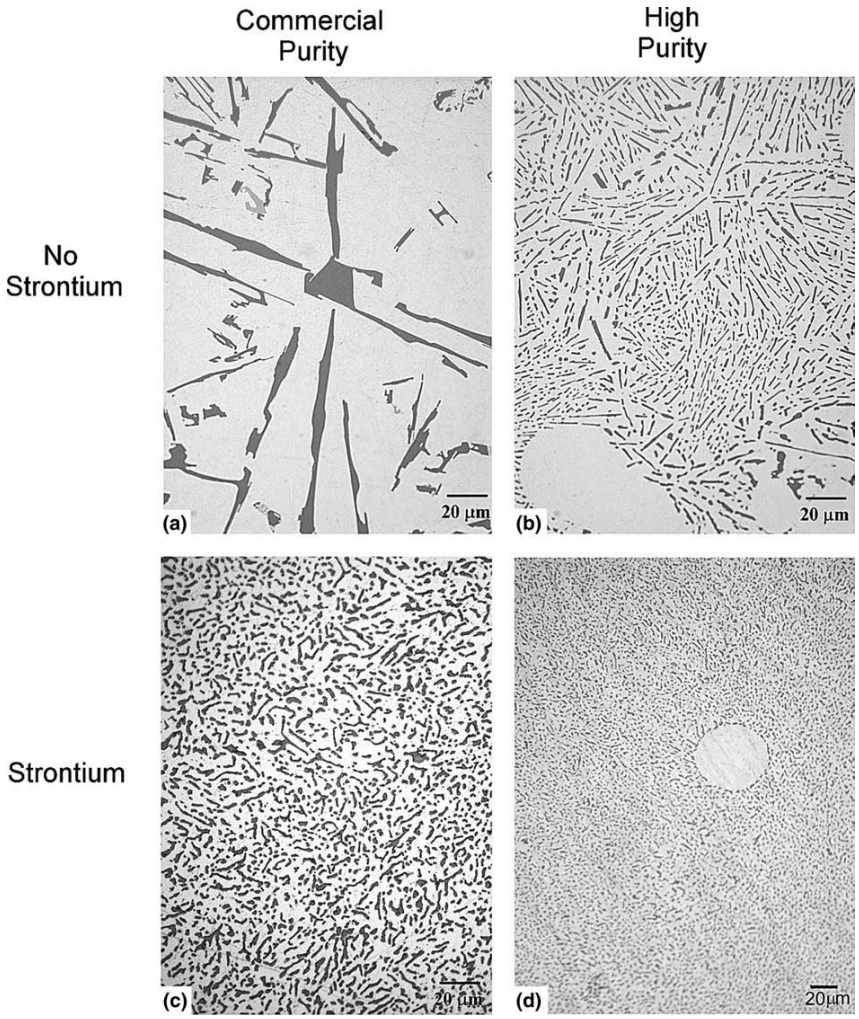

Figure 2-8. Different microstructures of commercial and high purity aluminums with and without addition chemical modifiers (Sr here) [69]

Chemical modification: The effect of addition of so called modifiers on the morphology of Si particles has been reported since the 1920's and the patents of Pacz [70]. From then and until the 1960's sodium was mainly used but because of the difficulty to control its concentration in the melt and because of the fumes emitted during the process, it was eventually replaced by strontium. An example of chemical Si modification by addition of Sr is shown **Figure 2-8** for commercial and high purity aluminum alloys. First, it is interesting to see that the purity of the alloy has a refining effect on the microstructure. Indeed, in both

unmodified and modified alloys, the high purity ones exhibit a finer eutectic microstructure. It is explained by the presence of numerous nuclei in the commercial alloy therefore promoting the growth of coarse Si particles. Second, the addition of strontium resulted in a finer microstructure and in a transition from acicular to fibrous morphology for both purities.

Eutectic formation is divided into two stages namely nucleation and growth. Nucleation corresponds to the clustering of few Si atoms into nuclei. Then, by further addition of Si atoms from the liquid phase, the nuclei increase in size by growth. Until now, the community failed to propose a unified theory explaining the mechanisms of refinement by chemical modification. It seems well accepted that the added atoms have a poisoning effect on the formation of Si particles. However, as clearly shown in [68], this poisoning mechanism remains a matter of dispute in the literature. One view is that the chemical modifiers affect the nucleation of the Si particles while a second view propose that these chemical additives affect the growth kinetics. Most likely, the modifiers influence the kinetics of both nucleation and growth. Lu and Hellawell [71] have reported that the addition of Na to an Al–12%Si alloy generates a silicon eutectic modification due to increased twinning on the silicon particles. We will not go into many details about it since it is not the purpose of this study. However the reader is strongly directed to other publications for more details [46], [68], [69], [71]–[73].

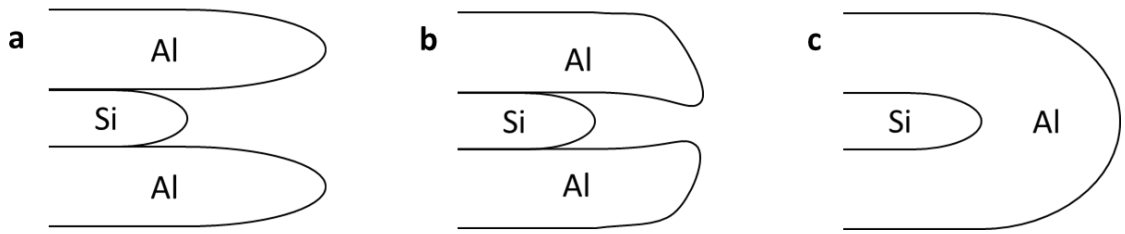

Figure 2-9. Solidification process of the eutectic phase at high cooling rates (a) as the cooling rate is increased, the aluminum solidifies faster than silicon (b) and (c) the aluminum phase encapsulates completely the eutectic silicon crystal and therefore stops its growth. [74]

Thermal modification: The cooling rate during solidification has been shown to have a similar effect on the eutectic microstructure. The higher the cooling rates, the finer the microstructure is. A mechanism of refinement was proposed in the late 1940's by Thall and Chalmers [75] and later reintroduced by Makhouf [68]. The refinement originates from the difference in thermal properties between Al and Si. The latent heats of fusion of Al and Si are 10.7 and 50.21 kJ/mol and their thermal conductivities are 237 and 148 $W/m^{-1}/K^{-1}$ respectively. Because of the large dissimilarities in thermal properties, the aluminum solidifies much more rapidly than silicon when cooling rates increase as shown **Figure 2-9a**. It continues until the aluminum encapsulates completely the silicon crystal as shown **Figure 2-9b** and **c**.

Summary of the Al-Si alloys and their microstructure

Aluminum is rarely used pure and is associated with several alloying elements, which give the alloy specific properties. The addition of silicon in aluminum reduces its melting temperature and increase its fluidity which make Al-Si based alloys the most used aluminum

alloys for casting and welding. Additionally, Si solidifies primarily into a pure silicon phase, which imparts very good wear properties to the alloy.

The microstructure of these alloys can be highly inhomogeneous and contains α-Al dendrites as the main phase and eutectic Si particles. Many intermetallic phases such as Mg_2Si or Fe-bearing phases can also be found. It was shown that the microstructure controls the mechanical properties of the alloy and is highly dependent on the thermal conditions. The size and shape of both the dendrites and Si eutectic particles can be tailored by specific thermal treatments or chemical modification. The mechanisms associated with the modification are yet to be understood.

In particular, a transition from acicular particles to a fibrous morphology of the eutectic Si phase was observed when high cooling rates are achieved or when chemical modifiers are used. This change of shape of the Si particles is associated with higher fracture toughness and higher ductility. A change of the fracture behavior was also reported when the microstructure (dendrites and Si particles) is refined.

3.4. Metal matrix composites

One of the process used to manufacture aluminum foams is the melt gas injection process. In this method, aluminum and SiC particles are poured into a crucible to create a Metal Matrix Composite (MMC) melt. Therefore, this section is aimed at introducing the notion of metal matrix composites and mechanisms of formation of their microstructure.

3.4.1. Definition

A metal matrix composite is a composite material made of two constituents. One is designated as the matrix and must be metallic while the other one is designated as the reinforcement and can be another metal, a ceramic or an organic compound. The role of the reinforcement varies from being purely structural to the improvement of physical and/or mechanical properties like corrosion and wear resistance, thermal conductivity, etc.

3.4.2. Matrix and reinforcement materials

The choice of a matrix alloy for an MMC is dictated by several considerations. Of particular importance is whether the matrix will participate in the composite strength or not. If not, the composite will be continuous and the role of the matrix will be mainly to transfer the load to the reinforcement phase. On the other hand, if the matrix serves as a structural component, high strength and tougher matrix are chosen. The interactions between the matrix and the reinforcements, the CTE mismatch for high temperature applications and fatigue behavior must be taken into account when selecting a matrix material. Matrix materials include aluminum and its alloys, copper, iron or titanium.

The same considerations apply to the reinforcement material. Its compatibility with the matrix regarding the application of the composite is critical. The shape of the reinforcements is very important as well. They can be whiskers, fibers or particles. Fibers will be anisotropic while whiskers and particles will exhibit a more isotropic behavior. Reinforcement materials

include silicon and boron carbide SiC and B_4C as well as alumina Al_2O_3 and more recently graphite.

3.4.3. Microstructure of the MMC made of casting alloys

Microstructures of MMC's are the result of the cooling conditions and are controlled by interaction mechanisms between the insoluble particles and the solid/liquid interface. When a particle is in contact with a moving solid/liquid interface, it can be either pushed or engulfed. A kinetic approach has been used to explain the phenomenon and the concept of critical velocity, above which the particle will be engulfed and below which it will be pushed, has been introduced. The first models assumed a pure matrix with planar interface in contact with one particle. However, in the case of MMC, the matrix is usually an alloy and multiple particles are in contact with the interface. Because of the impurities of the alloy and the influence of the particles, the solid/liquid interface is non-planar and mechanisms of pushing/engulfment are different. **Figure 2-10** shows the influence of interface shape on the interaction with particles. In the case of dendritic growth as in Al-Si alloys, small particles are trapped in the interdendritic region while larger ones are pushed.

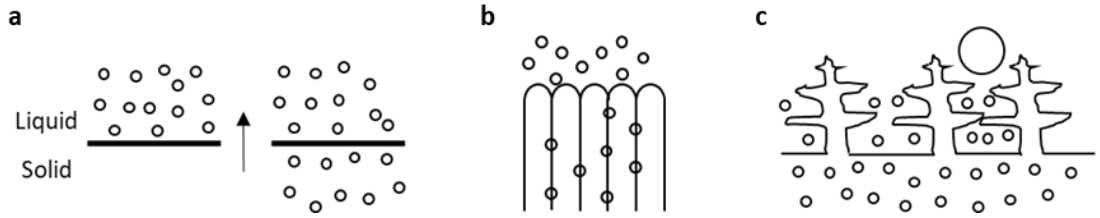

Figure 2-10. Influence of interface shape on particles. (a) Planar interface can result in pushing (left) or engulfment (right). (b) Cellular interface showing pushing at interface and entrapment between cells. (c) Dendritic interface; small particles are entrapped in interdendritic spaces while large particles are pushed [76]

The resulting microstructure of such material is very complex and the distribution of particle is somehow random. For MMC's, the critical velocity is a sum of contributions summarized in **Eq. 2-1** [76] as

$$R_{cr}=f\left(\frac{\Delta\sigma}{\eta\Phi},\frac{1}{r},\frac{K_L}{K_P},G\right), \qquad \text{Eq. 2-1}$$

where $\Delta\sigma$ is the variation of surface free energy when the particle approaches the surface, η the viscosity of the liquid, Φ the volume fraction of particles, r the particle radius, K_L and K_P are the thermal conductivities of the liquid and the particles respectively and G is the temperature gradient.

3.4.4. Note about MMC's in metallic foams

Making metallic foams can be achieved through several manufacturing routes [77]. The melt gas injection process is one of them and involves melting a MMC and injecting gas in it in order to create a cellular structure. The role of the ceramic particles is to increase the viscosity of the melt and to stabilize the cells. However, the concentration and size of the particles must be carefully controlled to ensure optimal properties of the foam as seen on **Figure 2-11**. Too many particles will increase the viscosity of the melt whereas too few particles may reduce the viscosity, perhaps resulting in a non-stable foam.

It is also important to note that the distribution of the ceramic particles is sensitive to the temperature gradient at the solid/liquid interface [76] and that the melt gas injection process results in a non-homogeneous cellular structure leading to density gradients and therefore different cooling histories from one part of the foam to another. Those two factors

combined can lead to local microstructure gradients inside the foam that is areas where the particle concentration is high and other areas where the particle concentration is null.

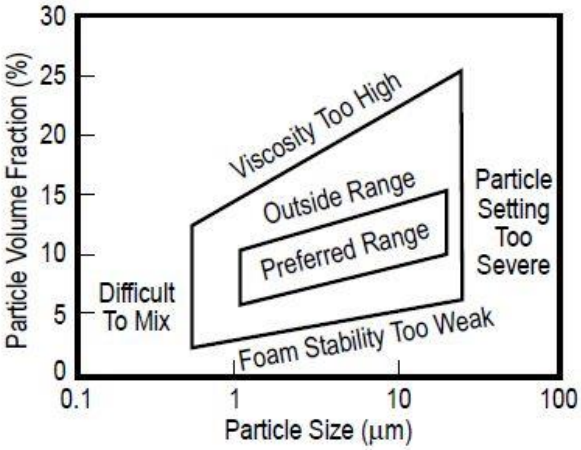

Figure 2-11. Preferable ranges of size and volume fraction of stabilizing particles for manufacturing a foam by melt gas injection [78]

This is of primary importance in ensuring optimal properties of the foam. Indeed, the strengthening effect of the particles have been investigated in several studies [79], [80] and a non-uniform distribution of particles can locally result in lower mechanical properties.

In addition, the presence of particles can also lead to an embrittlement of the foam. Onck et al. [81] characterized the microstructure of three metallic foams, two aluminum closed cell foams and one Ni-Cr open cell foam, before and after in situ fracture tests. The characterization of the two closed cells revealed precipitates or particles dispersed within the microstructure due to the manufacturing process. The Ni-Cr open cell foam showed no precipitates or particles. The results of the fracture tests of those three foams were clear. The open cell foams showed a ductile fracture behavior, revealed by important necking within the microstructure of the cell walls after the tests. On the other hand, the closed cell

aluminum foams exhibit a ductile fracture due to void growth by plastic flow and a brittle fracture due to cleavage of clustered precipitates. The embrittlement of the foam due to the presence of precipitates is clearly demonstrated as the precipitates limit the dissipation of energy by plastic deformation.

4. Aluminum foams

4.1. Introduction and manufacture of metal foams

Metallic foams are engineered materials developed relatively recently. They have multiple air/solid interfaces and a low density due to their high porosity, which give them interesting thermal, mechanical and electrical properties. They are now widely used in the industry and their applications range from structural components to energy absorption and thermal management. Interesting properties of metallic foams include lightweight structures because of their very good stiffness to weight ratio, mechanical damping, energy and acoustic absorption and thermal management.

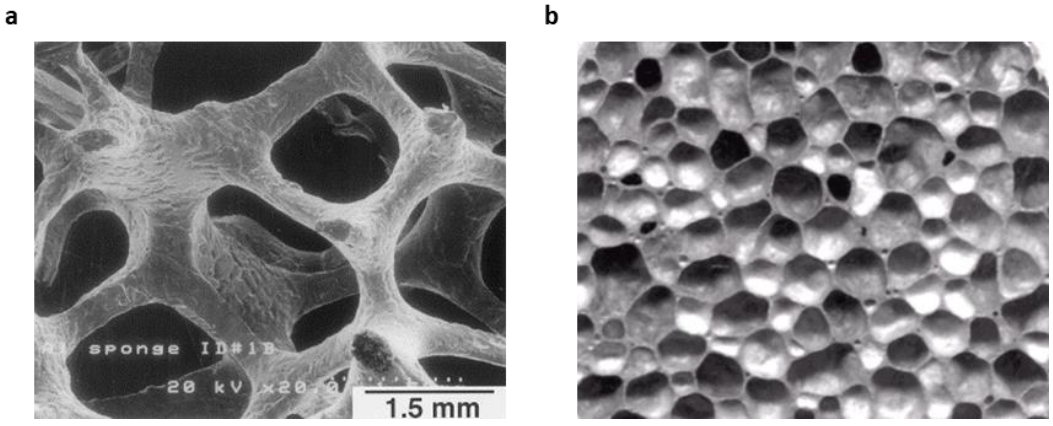

Figure 2-12. Two aluminum foams (a) open cells aluminum foam (b) closed cells aluminum foam

As defined by Gibson and Ashby [82], a cellular material is made up of an interconnected network of solid struts and plates forming the edges and faces of cells. Foams are the 3D representation of those structures and can be differentiated by how the solid is distributed within the cellular structure. When the solid is distributed in the cell edges only, the foam is said to be open-cell (**Figure 2-12a**). If the faces of the cells are solid too, the foam is said to be closed cell and forms a network of unconnected pores (**Figure 2-12b)**. This differentiation is very important as the properties and therefore applications of the foam will be impacted by it.

A critical parameter to determine the properties of the foam is the relative density. It is defined as the ratio of the density of the foam ρ^* divided by the density of the material which makes the foam ρ_S. High relative densities correspond to more solid distributed in the cell walls and therefore more resistant foams.

Metallic foams can be made from a variety of metals but aluminum is the most used one. It is light and possesses good mechanical properties when used in its alloyed forms.

Several manufacturing routes are available to make metallic foams which mainly differ in the way that the pores are generated [77], [83]. It can be achieved by injecting directly the gas into the molten metal, by inducing a gas releasing precipitation or by introduction of foaming agents directly into the melt. The melt gas injection process belongs to the first category of routes.

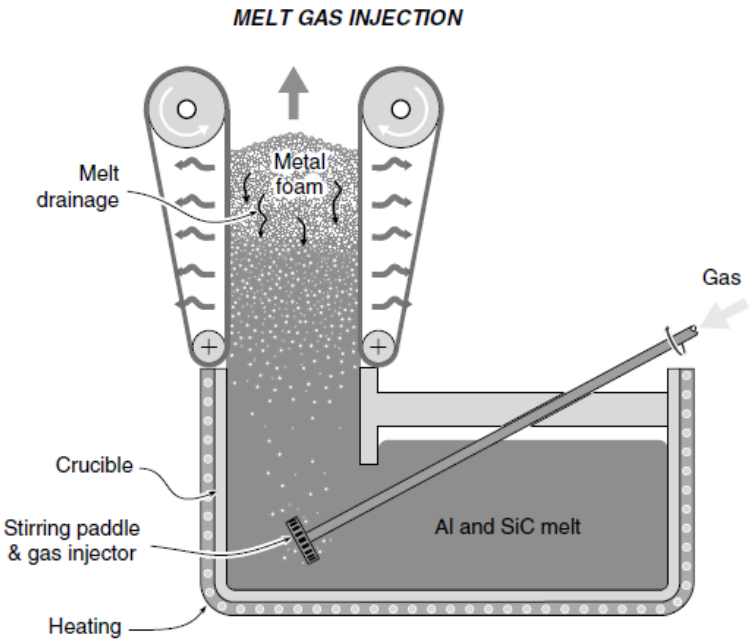

Figure 2-13. A schematic illustration of the manufacture of an aluminum foam by the melt gas injection method (CYMAT and HYDRO processes) [83]

A schematic illustration of the melt gas injection method is shown **Figure 2-13**. It is currently only used for the manufacture of Al foams. In this method, aluminum and SiC particles are poured in a crucible to create a MMC melt. Using only aluminum would result in a non-stable foam and in a very difficult drainage of the foam. However, the addition of insoluble SiC particles provides the required viscosity to the melt for the foam to slowly be drained and solidify. The next step consists in injecting the gas (nitrogen, air, argon) through rotating impellers or vibrating nozzles. It allows very fine and regular bubbles to be generated and evenly distributed in the liquid metal. The addition of SiC particles stabilizes the bubbles at this stage of the process. After injection of gas, the liquid is stable enough to be pulled off from the tank and is cooled down to room temperature.

As specified in [77], the advantage of this method over others is that it allows large amount of material to be produced therefore making it economically very interesting. The drawbacks are that only aluminum foams are produced so far using this technique. The drainage can cause a deformation of the cell structure and favor anisotropy. The addition of insoluble particles must also be carefully monitored to avoid a detrimental impact on the mechanical properties of the foam (see the section 3.4.4 about MMC in foam for more information).

4.2. Mechanical behavior of aluminum foam

Mechanical testing includes compression, tension and shear testing.... Only the compression behavior is discussed here but it is important to note that the properties of a foam in tension can be surprisingly different from the ones in compression. Thus, what is explained in the following section will not apply to a foam solicited in tension or shear.

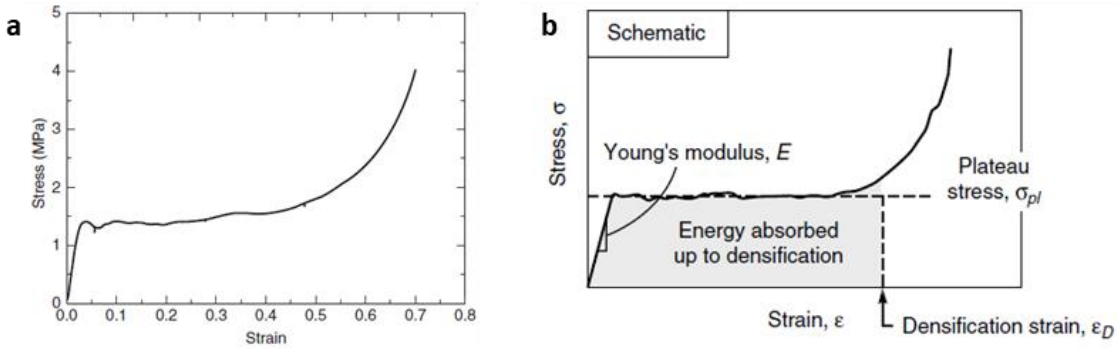

Figure 2-14. (a) Stress–strain curve from a uniaxial compression test on a cubic specimen of a closed-cell aluminum foam [84] (b) Schematic of compression curve for a metal foam showing properties [83]

Sample size and preparation are critical to ensure good results. Machining a foam is damaging to the material and can create defects within the cellular structure. As reported by Ashby [83], cutting foams with a band saw can cause a 15% decrease in mechanical properties.

The properties of metallic foams under compression exhibit a unique behavior, which explains their use as structure components or shock absorbers. A typical example of a stress strain curve of a foam under compression is shown **Figure 2-14**. It shows three domains associated with different deformation mechanisms of the structure [82]–[85]. The first one is a linear elastic domain corresponding to cell wall bending and cell face stretching. Local plasticity makes the unloading curve different from the loading one during this stage. As the stress increases, the structure collapses at a constant load, corresponding to the plateau observed on the curve. This is the plateau region, which explains the desirable energy absorption properties of metallic foams. During this stage, yielding or fracture of the cell walls and membranes occurs at constant applied load. Several authors studied the deformation mechanisms of closed cells aluminum foams and they showed that the onset of the plateau region corresponds to the first appearance of strain concentration inside the structure [85]–[87]. By using strain mapping and tomography, it was shown that the concentration occurs in the weaker cells. The weaker cells are defined here as the elongated cells normal to the direction of loading and the ones having thin or entangled walls [85], [88]. Further increasing the stress results in a propagation of the strain in the neighboring cells and the appearance of a deformation band. Once all the cells in the band have collapsed,

the same chain of events occurs in another area of the structure. The third and final stage of deformation is the densification, beyond which the structure compacts and the stress rises steeply. It appears when all the cells have collapsed and the stress is high enough to force contact between opposing cells faces and walls. On the compression curve, the stress rises sharply.

4.2.1. Influence of foam architecture and its characterization

Understanding the mechanical properties of foams is a complex task. Indeed, several features govern the mechanical response of a cellular material. It is now known that the mechanical behavior of a foam depends on its structure: cell size and shape, local variation of density, curvature of the cells. The most important characteristic of a cellular solid is the relative density [82]. It is defined as the ratio of the density of the foam ρ^* to the density of the solid of which the foam is made ρ_S. The relative density reflects the volume fraction occupied by the solid and therefore its porosity. High density corresponds to higher mechanical properties. Different models have been developed to quantify this influence. The simplest one was proposed by Gibson and Ashby and connects some mechanical properties (elastic modulus, plateau stress, densification strain...) to the relative density. However, those models have failed to predict the behavior of industrial foams. The reason is that it does not take into account the influence of the cell shape and curvature of the cell walls. Indeed, several studies [87], [89], [90] have found evidences that cell geometry more than cell size is of particular importance. Isotropic properties are associated with equiaxed cells. However,

when the cells are elliptical and elongated, the material is anisotropic and its properties highly depend on the direction of testing. The analysis of the deformation mechanisms showed that the elongated cells, perpendicular to the loading direction initiate the failure of the material.

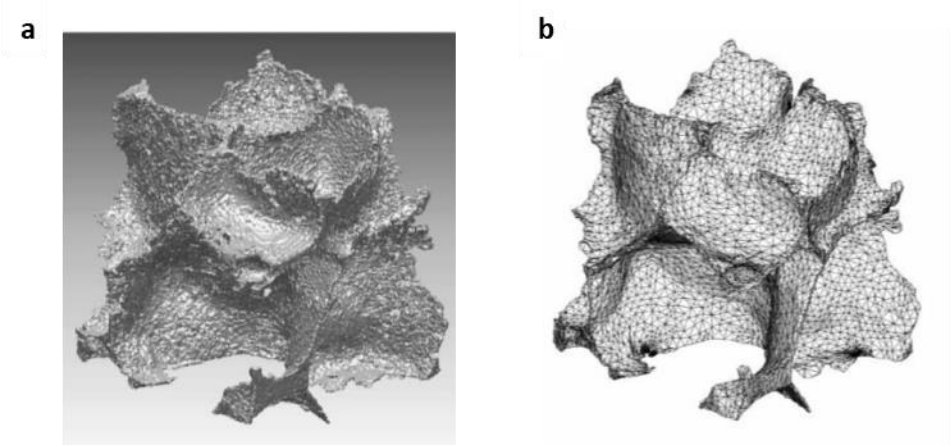

Figure 2-15. (a) Reconstructed volume of an aluminum foam obtained by X-ray tomography (b) 3D finite element of the same volume from tomographic data [91]

The morphology of the foam is mainly determined using microscopy techniques. Optical microscopy and electron microscopy are the most common techniques used. The samples are usually observed in cross section and the microscopy gives 2D information about the cell morphology and density of the foam. However, the observations are limited to cross sectional observations and information about the structure in the volume is difficult to obtain. That is why more advanced techniques based on X-ray tomography are now used. It is a non-destructive method, which gives a 3D presentation of the cellular structure. It also gives valuable information about the geometry of the cells. The resolution of such techniques ranges from tens of microns up to few microns. The study by Bart-Smith is one of the first,

if not the first, to mention the use of tomography to study the deformation behavior of foams. The author used tomography to observe the onset of deformation at the cell level during a compression test [85]. After that, several other studies have mentioned the use of tomography to characterize foams [88], [91]–[95]. Nowadays, the tomographic data are combined with FEM methods [91], [92], [95] to simulate the mechanical response of the foam (see **Figure 2-15**). It allows using a real volume as opposed to using ideal structures.

4.2.2. Influence of cell wall properties and their characterization

Composition of the walls also affect the properties of the foam and several studies investigated the effect of microstructure on the properties of metallic foams [96]–[98]. Markaki and Clyne [96] examined three closed-cell foams having comparable density and morphology but having significantly different compositions and therefore microstructures. Their results showed indeed an effect of the microstructure on the compressive and tensile properties of the foam by tailoring the fracture mechanisms.

Schuler, et al. [97] examined the influence of the microstructure of an AlSi7Mg0.3 aluminum open cell foam on its mechanical properties in tension and compression. Al-Si-Mg bulk alloys are usually subjected to a heat treatment to modify the morphology of the eutectic Si platelets. The change of morphology from coarse, acicular to fine, fibrous eutectic Si platelets is associated with great improvement of the yield stress compared to the as-cast alloy. Thus, they decided to apply the same heat treatments commonly used for bulk alloys to the foam. They showed that the heat treatments have significantly less effect on the

microstructure of the foam than it has on the microstructure of a bulk Al-Si alloy. The shape of the Si platelets was slightly modified and the onset of rounding of Si particles was observed. However, the heat treatment favored the precipitation of fine, spherical precipitates in the Al matrix. While the results of the mechanical characterization revealed the importance of the Si platelet shapes on the fracture mechanisms of the foam, they also revealed the negligible effect of the heat treatment on the mechanical properties. The ductility was slightly improved because of the rounding of the Si platelets but nothing comparable to what is usually observed in bulk alloys. In conclusion, conventional heat treatments are not very effective to modify significantly the microstructure of a foam. Specific heat treatments must therefore be developed for foams.

More recently, Islam et al. [98] examined individual cell walls of an Al-Si closed cell aluminum foam reinforced with Al_20_3 particles. The failure has been observed as combination of little ductile tearing and largely cleavage fracture. The presence of micro-pores and micro-cracks provided a natural path of crack propagation. Specifically, the combination of high void fraction regions and β-AlFeSi was the preferred pathway of crack propagation. The microstructure plays therefore a critical role in the failure mechanisms of cell walls.

4.2.3. About size effect in foams

Aluminum foams are often used in structural sandwich panels. It is then important to understand the effect of specimen size (compared to the cell size) on the mechanical properties. Size effect manifests itself when the material dimensions are close to the length

scale of the structural features, in this case the cell. Andrews et al. [99] were among the firsts to address this issue and their results is now used as a rule to design aluminum foam material. In order to quantify the influence of specimen size, they measured the mechanical properties of foams having a normalized size ranging from 1 to 18. The normalized size is defined as the ratio of the specimen thickness to the average cell size. As shown on **Figure 2-16**, the properties become independent of the sample dimensions when the normalized size exceeds 8. The mechanisms explaining this size effect have to be found in the effect of the decreased constraint at the free surface of the foam, giving a reduced boundary layer stiffness, and the area fraction of cut cell walls at the boundary which remain stress-free [99]. Both contribute to lower the properties observed in **Figure 2-16**.

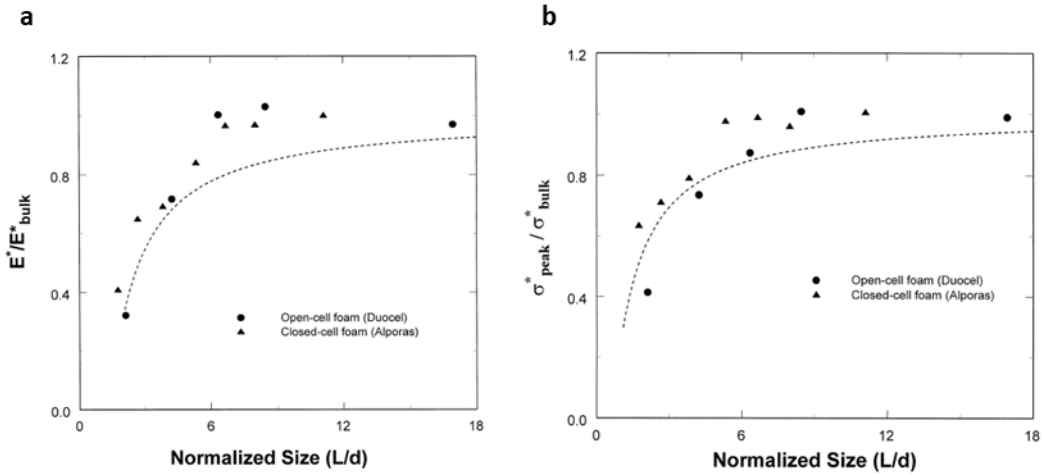

Figure 2-16. The effect of the ratio of specimen size to cell size on (a) Young's modulus and (b) on compressive plateau stress for two aluminum foams. The modulus and strength become independent of size when the sample dimensions exceed about seven cell diameters [83], [99]

Summary of the properties of aluminum foams

Aluminum foams are cellular materials and exist as open or closed cells. Several manufacturing routes are available to make metallic foams, which mainly differ in the way that the bubbles are generated. The melt gas injection process is exclusively used to manufacture aluminum foams and several foam densities can be achieved.

The cellular structure gives foams a unique compression behavior characterized by a linear elastic region during which the structure deforms elastically and very few plastic events occur. As the stress increases, the weakest cell walls deform and the deformation propagates along the sample thickness; this is the plateau region. Once all the structure has failed, the densification takes places, beyond which the structure compacts and the stress rises steeply.

The mechanical properties depend on the cell morphology, which includes the relative density (defined as the ratio of the foam density to the density of the alloy the foam is made of), the cell size and shape. The composition of the cell wall also defines the overall properties of the foam. Thus, as explained by Markaki and Clyne [96], optimization of their performance clearly requires an understanding of the interplay between processing conditions, cell structure, cell wall microstructure and mechanical response under various types of applied load.

CHAPTER THREE

Materials and Experimental Methods

This chapter provides a detailed record of the procedures that were followed when completing the experiments discussed in the dissertation. The first section focuses on the presentation of the materials and the sample preparation procedures. Due to their differences, the samples studied required the development of two distinct surface preparation procedures. It is followed by the discussion of the X-ray tomography technique used for the quantification of the foam morphology and to determine the macroscale compression mechanisms. Subsequently, the working principle and the apparatus are presented. The procedure developed to characterize the cellular structure using the Avizo software is then discussed.

The nanoindentation technique, used to characterize the hardness of the material at the microstructural level, is then extensively explained. Finally, the different microscopy techniques used to image and characterize the microstructures are presented.

1. Material and surface preparation

1.1. Materials

1.1.1. Coating/substrate system

Thermal spray coatings and more specifically HVOF sprayed coatings are industrially used to protect components from wear and corrosion damages. The adhesion between the coating and the substrate is an essential parameter governing the lifetime of mechanical parts. The system presented in this work is commercially available in the manufacture of ball valves for the oil and gas industry. To improve the lifetime of the valve, the coating/substrate interface was investigated. In this end, the exact coating conditions and materials originally used on the commercial products were reproduced on 100x20x5 mm bars as depicted in **Figure 3-1a**. However, the surface treatment and spray parameters are proprietary and thus excluded from this dissertation.

The substrate is a 17-4 precipitation hardening (17-4PH) martensitic steel, the composition and properties of which are shown in **Table 3-1** and **Table 3-2** respectively. The steel is in the H1150 condition meaning that it underwent a heat treatment at 621°C (1150°F) from the solution treated condition. The surface of the steel substrate was prepared in two different ways prior to the coating deposition process. One sample was grit blasted with alumina particles and another one was polished up to 1µm with diamond suspension.

Following the surface treatments, both samples were coated with a cermet material powder made of chromium carbides Cr_3C_2 embedded in a NiCr metallic binder (80% Cr_3C_2

- 20% NiCr) and size −45/+11 µm. The coating is produced by High Velocity Oxy-Fuel (HVOF) spraying and is 250 µm thick. Again, the surface treatment and spray parameters are proprietary and thus excluded from this dissertation.

Table 3-1. Chemical composition of the 17-4PH stainless steel substrate [100]

Name	**Composition**							
	C	Mn	Si	Cr	Ni	P	S	Other
17-4PH	0.07	1.00	1.00	15.5 - 17.5	3.0 - 3.5	0.04	0.04	3.0 - 5.0 Cu; 0.15 - 0.45 Nb

Table 3-2. Selected mechanical properties of the 17-4PH stainless steel substrate [100]

Condition	E (GPa)	UTS (MPa)	Yield strength (MPa)	Hardness HRC	Poisson's ratio
H1150	196	930	725	28	0.272

Samples were embedded in a carbon-filled resin using a hot mounting press following the procedure described in **Figure 3-1**. Two pieces of materials were extracted from a bar provided by the manufacturer in two cross sectional directions as shown on **Figure 3-1a** and **b**. The two pieces were mounted in the same resin and faced each other to ensure a uniform polishing of the coating and substrate (**Figure 3-1c**).

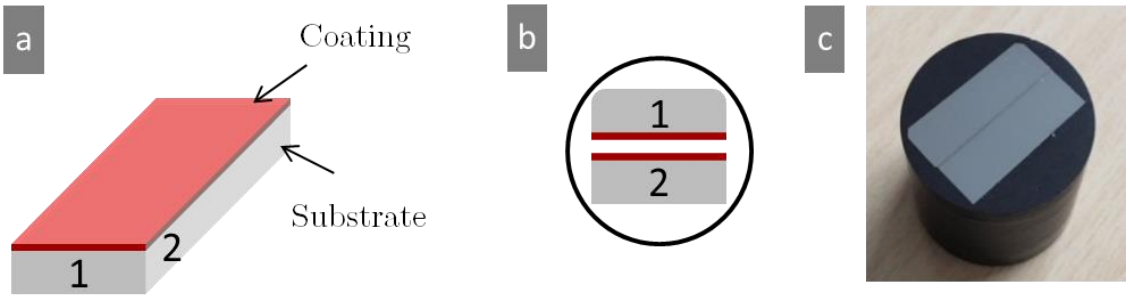

Figure 3-1. (a) Schematic representation of the coated bar as received by the manufacturer. The coating is in red and the substrate in grey. (b) Schematic representation of the samples as mounted in the resin. (c) Photograph of the samples mounted in the conductive carbon filled resin.

1.1.2. Aluminum Foam

A closed cell aluminum foam from Cymat was fabricated using the gas melt injection process explained in Chapter 1 resulting in an absolute density of 440kg/m^3 and a relative density of approximately 0.16. The density of pure aluminum (i.e. 2700kg/m^3) was used for the calculation of the relative density. The foam is made from a metallic matrix composite melt, here, an A359 Al-Si alloy mixed with SiC particles. The chemical composition of the foam is shown in **Table 3-3**.

Table 3-3. Chemical composition of the aluminum foam obtained from the manufacturer

Foam Composition	Al	Cu	Fe	Mg	Mn	Other, each	Other, Total	Si	Ti	Zn	SiCp
Matrix (85% by weight)	rem.	0.10	0.12	0.55 - 0.7	0.10	0.05	0.15	9.00	0.20	0.10	
Reinforcement (15% by weight)	-	-	-	-	-	-	-	-	-	-	100

To ensure and facilitate the penetration of the resin into the cells of the foam, the resin was first melted before applying the full-recommended pressure. **Figure 3-2** shows the foam after being embedded in a conductive carbon filled resin.

Figure 3-2. Photograph of the aluminum foam sample embedded in a conductive carbon filled resin

1.2. Grinding and polishing

The development of good polishing procedures is critical to ensure reproducibility in the observations and the measurements. Moreover, in the case of nanoindentation, the surface needs to be as clean as possible in order to avoid any artifacts in the measured values resulting from the surface preparation. A clean surface means a flat non-deformed surface having a low roughness with no scratches, no residual polishing particles and no work hardening. It was achieved by developing a specific procedure for both the coated material and the foam. All the successive stages in the grinding and polishing process have been performed with an automatic polishing machine MECATECH 234 from PRESI (Figure 3-3). The force applied on the samples, rotating speeds of the plate and the polishing head are controlled for an optimal quality of polishing. The flow of lubricants or abrasives is controlled as well allowing a precise dosage, ensuring perfect reproducibility, whatever the user is.

Figure 3-3. Polishing device Mecatech 234 - PRESI

The procedures involve conventional metallographic preparation with resin bonded diamond discs followed by a polishing with diamond suspension solutions up to 1µm. Finally, chemical mechanical planarization (CMP) using non-crystallizing colloidal silica was used. To remove the excess of colloidal silica, the surface is cleaned with a surfactant solution using a PVA sponge and dried with nitrogen. A final cleaning of the surface is carried out by CO_2 snow blasting. **Table 3-4** summarizes the surface preparation procedures for each material, detailing the polishing cloths and solutions as well as the parameters of the polishing machine employed.

Table 3-4. Polishing procedure for the two materials used in this work

Aluminum Foam							
Surface	MD Piano	MD Piano	MD Piano	Md Largo	MD Plus	MD Nap	MD chem
Grain size	#500	#1200	#2000	9μm	3μm	1μm	0,04μm
Abrasive	Resin bonded diamond	Resin bonded diamond	Resin bonded diamond	Diamond suspension	Diamond suspension	Diamond suspension	Colloidal silica
Lubricant	Water	Water	Water	Distilled water	Distilled water	Distilled water	Distilled water
Plate speed (rpm)	150	150	150	150	100	100	120
Head speed (rpm)	150	150	150	150	100	100	90
Force (N)	10	10	10	10	10	10	10
Time (min)	until flat	4	5	6	8	31	5

Coating/Substrate system								
Surface	MD Piano	MD Piano	MD Piano	MD Piano	Md Dur	MD Dac	FD1N	MD chem
Grain size	#220	#500	#1200	#2000	6μm	3μm	1μm	0,04μm
Abrasive	Resin bonded diamond	Resin bonded diamond	Resin bonded diamond	Resin bonded diamond	Diamond suspension	Diamond suspension	Diamond suspension	Colloidal silica
Lubricant	Water	Water	Water	Water	Distilled water	Distilled water	Distilled water	Distilled water
Plate speed (rpm)	150	150	150	150	150	150	150	90
Head speed (rpm)	120	120	120	120	120	120	120	50
Force (N)	15	15	15	15	10	10	10	10
Time (min)	until flat	until flat	5	5	4	4	5	15

2. Computed tomography

This section introduces the μ-Computed Tomography technique (μCT) in order to explain the benefits for the characterization of foams. It is then followed by a quick presentation of the technique in addition to the working principle of the instrument. Finally, the apparatus and experimental details are presented.

X-ray tomography is a nondestructive technique for imaging of a solid object. It gives access to information about the volume and internal features of the material. The most common way to scan the volume is by performing multiple radiographs while the sample is incrementally rotating. The output of a tomographic scan is a set of slices corresponding to what the material would look like if sliced open along a specific axis. The slices are made of voxels, which can be understood as the 3D version of pixels, and corresponds to a certain thickness of the material being scanned. The volume is reconstructed by stacking all of the slices together.

In materials sciences, μCT is more and more used as a laboratory tool to characterize the internal geometry or assess the internal damages of a structure or a material [101]–[103]. In Finite Element Modeling (FEM), it is used to mesh and perform calculations on a real volume instead of using ideal geometries [92], [104], [105].

For foams, X-ray tomography is mostly used to characterize the morphology of the cellular structure as it gives access to internal 3D information about the size and shape of the cells. In addition, tomography has brought understanding on the deformation

mechanisms of cellular materials by imaging the material when subjected to compression or tension loading [88], [89], [92]–[95].

2.1. Fundamentals

X-ray tomography is based on the interaction between an incident X-ray beam directed at a sample from multiple orientations and collected by a detector placed on the other side as shown in **Figure 3-4**.

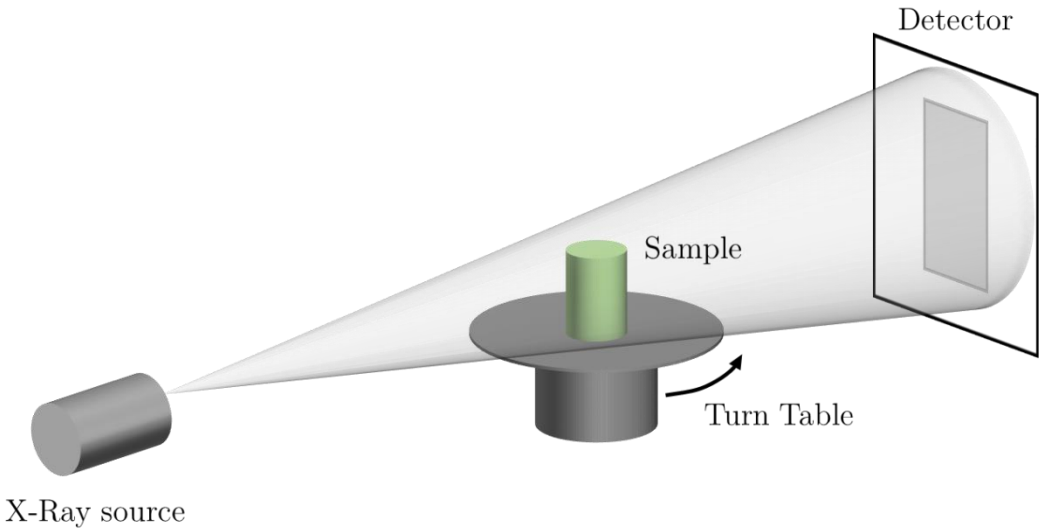

Figure 3-4. Schematic representation of the cone beam transmission tomography (reproduced from [106])

In transmission tomography, the Beer-Lambert law describes the attenuation of the incident X-ray due to the sample as

$$I_1 = I_0 e^{-\mu s}, \qquad \text{Eq. 3-1}$$

where I_0 is the intensity of the incident beam, I_1 is the intensity of the beam transmitted through the sample following the path s and μ is the linear attenuation coefficient which is a function of the density and atomic number of the body being scanned.

2.2. Apparatus

Figure 3-5 shows the UltraTom XL tomograph by RX-SOLUTIONS used throughout this work (Institut Pprime ISAE - ENSMA - Poitiers). It has three divergent X-ray sources: two microfocus X-Ray sources of 150kV, 230kV, and a nanofocus X-Ray source with an acceleration voltage of 160kV. The 160kV nanofocus is used when a high resolution is necessary. We used the 150kV microfocus to determine foam morphology. An attempt to characterize the microstructure of the aluminum foam was also made using the 160kV nanofocus. The sample is installed on a turntable, which rotated the sample during the scan. The glue used to put the sample on the holder must be rigid enough to avoid vibrations during the rotation of the sample. The source/sample and sample/detector distances are a compromise between a good resolution and an acceptable acquisition time.

The reconstruction software Xact is used to reconstruct the volume into a stack of images in the three directions. The image analysis software Avizo is then used to reconstruct the volume from the stack to perform the morphology analysis.

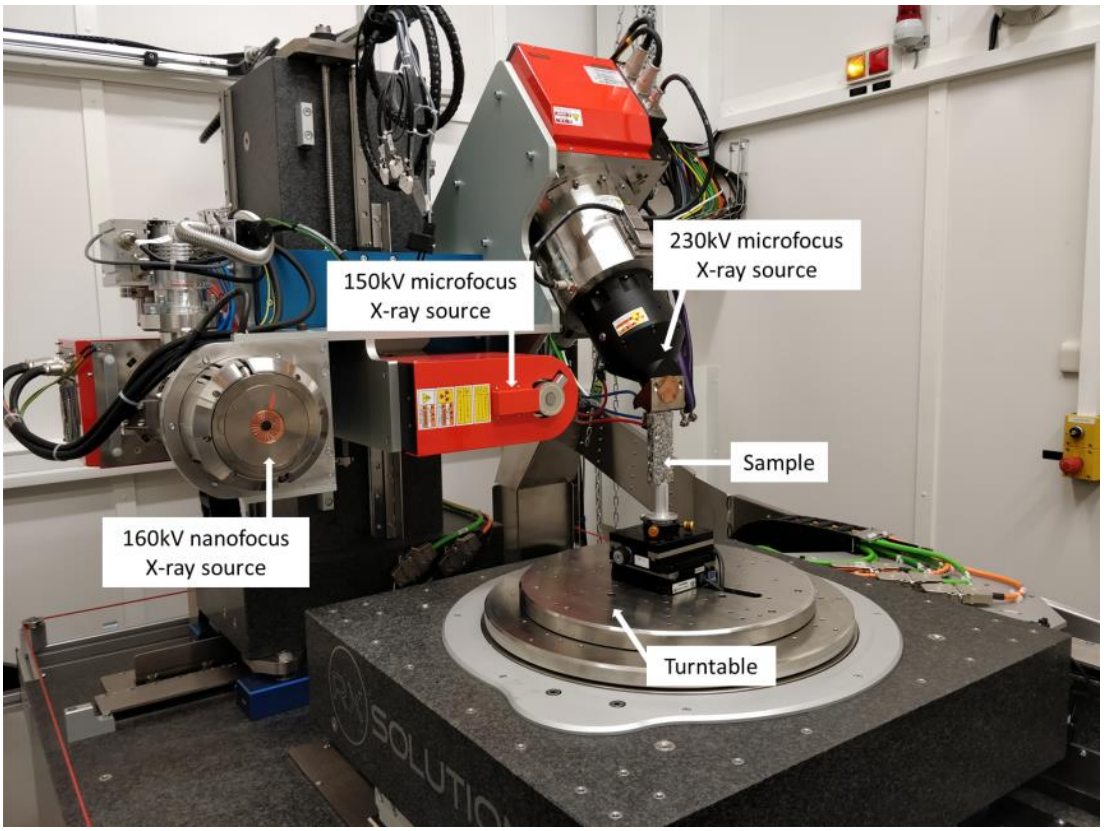

Figure 3-5. RX-SOLUTIONS tomograph from Pprime Institute (ISAE - ENSMA - Poitiers)

2.3. Experimental details and image processing procedure

2.3.1. Tomography experimental details

Two samples were used to characterize the morphology and are shown on **Figure 3-6a** and **b**. The dimensions of the samples were slightly different leading to two different voxel sizes, 30 and 24µm for sample 1 and 2 respectively. The dimensions of the samples are a compromise of a good resolution of the scan, so the details of the structure are captured, and a volume statistically representative of the cellular structure.

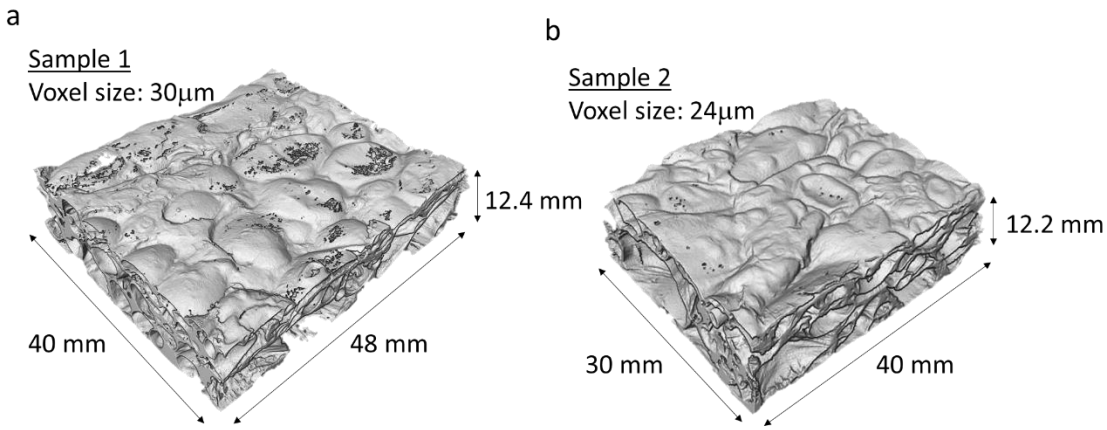

Figure 3-6. Tomographic image of the two samples used to characterize the morphology of the foam. The two samples have different dimensions resulting in different voxel size. (a) Reconstruction of sample 1 (voxel size 30µm) (b) Reconstruction of sample 2 (voxel size 24mm)

2.3.2. Relative density calculation

The relative density was calculated as the percentage of black pixels of the binary image shown in **Figure 3-7b**. A distribution of the relative density along the sample height was obtained by calculating the percentage of black pixels for each slices in the direction of the sample thickness. The binary images and calculations were obtained with ImageJ by using the build-in "MaxEntropy" thresholding method and the "Stack measurements" module.

2.3.3. Cell size quantification

The cell size was analyzed using the Avizo software. It was done by following several steps consisting of cell detection, cell post-processing, and cell measurements. **Figure 3-7** shows the essential steps on how to compute the distribution of cell diameters in the foam. The first thing to do is to detect the cells from the original image (**Figure 3-7a** and **b**) using a threshold binarization tool. In the binary image, all pixels that meet the imposed set

of conditions (here, the condition is pixel intensity within the two bounds set of thresholding) are set to a value of 1 and all other pixels are set to 0. The blue pixels correspond to the voids of the structure while the black ones correspond to the solid material (cell walls and faces).

The post processing treatment is necessary to correct the irregularities of the structure that appear due to poor resolution. **Figure 3-7c** and **Figure 3-7d** show the result of the post processing. Only the cells of interest have been kept and labeled.

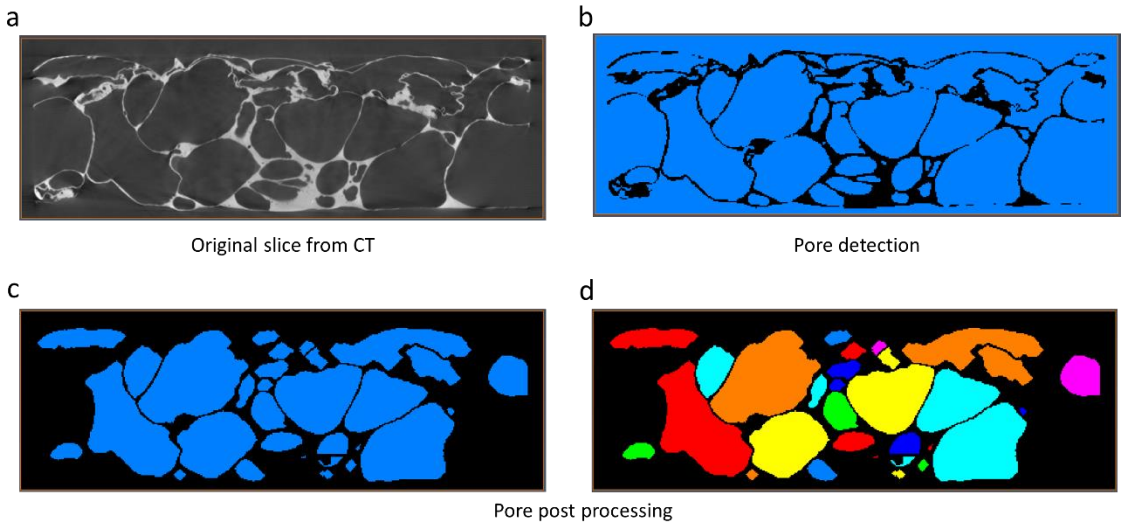

Figure 3-7. Procedure for the analysis of porosity (a) original image as obtained after tomography (b) pore detection after threshold binarization (c) post processing; only the pores of interest are left (d) post processing; each pore is detected and labeled for analysis.

After post processing, only the cells of interest are left and indexed. The morphology of the cells is characterized by calculating the surface and the volume of the cells, the equivalent diameter, corresponding to the diameter of a sphere of the same volume, and the sphericity, describing how spherical an object is.

3. Nanoindentation

Nanoindentation was used to characterize the local hardness and Young's modulus of the materials at the microstructural level. This presents the theory behind classical nanoindentation. The apparatus and experimental details are then presented. Finally, the hardness cartography technique based on the analysis of a large number of indentations is explained.

3.1. Introduction and description of the method

Nanoindentation also called ,instrument indentation testing (IIT) , is an evolution of the regular indentation test and is used to measure mechanical properties at very small scale, which makes it particularly suitable for determining the local mechanical properties of materials. The nanoindentation was developed in the early 1990's following the work of Oliver and Pharr, but earlier studies were performed in the 1970s and 1980s. We can cite the work of Loubet et al. in 1983, who were among the first to propose a modified indenter, which is capable of continuously recording the penetration depth and load.

Compared to regular indentation tests, small loads can be applied up to a few micronewtons and the load and displacement of the indenter are continuously recorded. The mechanical properties are determined from the load-displacement data without imaging the residual imprint, leading to a better resolution at small scale where the residual impression can be difficult to image.

Figure 3-8 shows a characteristic nanoindentation curve obtained during one full cycle of loading and unloading. The important variables are the maximum force reached during the test F_{max}, the true contact depth h_c, the maximum depth reached during the test h_{max}, the depth of the residual imprints after removal of the indenter h_p , and the contact stiffness at the beginning of unloading S.

A nanoindentation test is comprised of a loading and an unloading part. As the indenter penetrates into the material, both elastic and plastic deformation usually occur resulting in a residual impression that conforms to the shape of the indenter to a contact depth h_c also called true penetration depth. During unloading, only the elastic part of the deformation is recovered. If the material deformed plastically, the final depth h_p will be non-zero and correspond to the plastic contribution of the total depth h_{max}. If no plastic deformation occurred, h_p is null. If a purely elastic deformation is assumed during the unloading, the slope S of the curve during the first stages of unloading corresponds to the stiffness of the elastic contact.

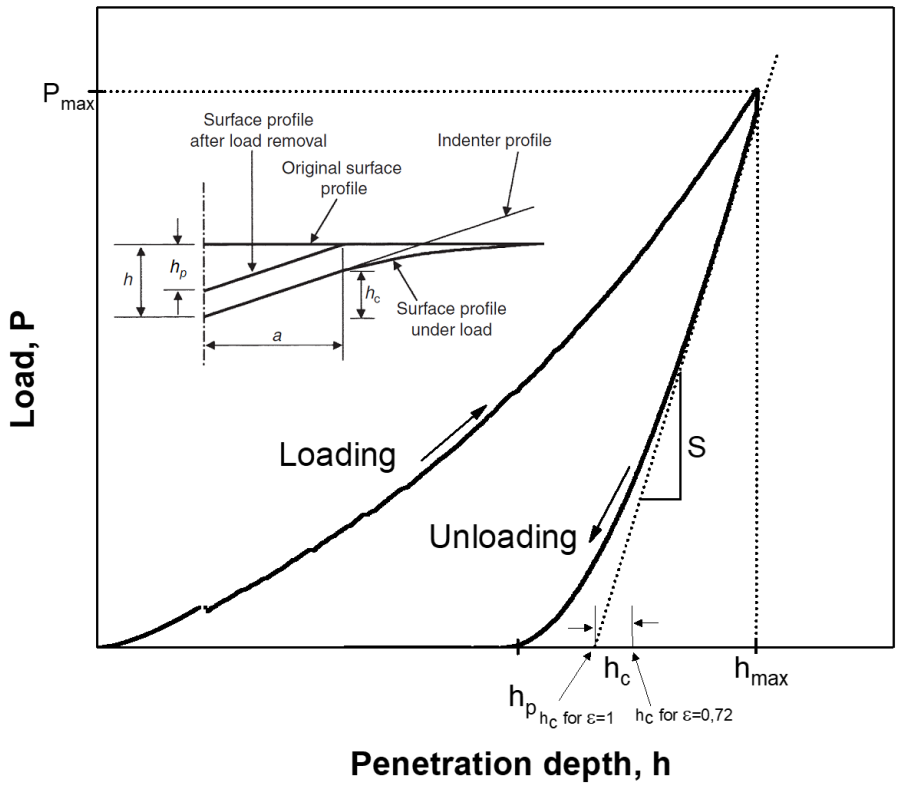

Figure 3-8. Schematic representation of indentation load-displacement data during a loading-unloading cycle [107]

Various indenter shapes and materials are available. They are usually made of diamond to reduce the contribution of the indenter itself in the total displacement. The most common shape is the Berkovich tip. It is a three-sided pyramid with a centerline to face angle of 65.3°. This three sided pyramid tip ensure a lower tip defect compared to other pyramidal tips and is thus more appropriate for very low penetration tests.

The hardness in nanoindentation is defined as the Meyer hardness, which is the maximum applied load divided by the projected contact area under load and is given by

$$H = \frac{P}{A_p}, \qquad \text{Eq. 3-2}$$

where H is the hardness, P the applied load, A_p the projected contact area.

The modulus is derived from the Sneddon relationship [108] described later and can be written as

$$E_r = \frac{\sqrt{\pi}}{2\beta}\frac{S}{\sqrt{A_p}}, \qquad \text{Eq. 3-3}$$

where E_r the reduced modulus, S the slope of the upper part of the unloading curve ,and β a geometric constant. Eq. 3-3 is derived from the elastic contact theory in which the contact is modeled by a rigid indenter of a known shape in elastic contact with an elastic medium. The reduced modulus E_r accounts for the deformation of both the indenter and the sample and is defined as

$$\frac{1}{E_r} = \frac{1-\nu^2}{E} + \frac{1-\nu_i{}^2}{E_i}, \qquad \text{Eq. 3-4}$$

where E_i and ν_i are the elastic modulus and Poisson's ratio, respectively of the indenter and E and v are the properties of the indented material. For indenters made of diamond, E_i=1141GPa and ν_i=0.07. As explained by Hay and Pharr, Eq. 3-3 was developed for an axisymmetric indenter and applies to circular contact. However, by adapting the value of the constant β, the formula can be used for other indenters. Thus, for indenters with a triangular cross section like Berkovich, the value of β is 1.034 [109].

Both relationships in Eq. 3-2 and Eq. 3-3 require knowing the projected contact area, which is obtained from the true penetration depth during the contact, h_c. The true penetration depth is a fundamental notion in nanoindentation, which describes the depth at which the indenter and material are in contact (see **Figure 3-8**). Doerner and Nix (1986), Oliver and Pharr (1992) and Woirgard and Dargenton (1997) proposed various methodologies for calculating h_c from the indentation curve and for interpreting instrumented indentation data.

Moreover, Doerner and Nix defined h_c as the intercept of the initial unloading slope with the horizontal axis, which works well for a flat punch approximation. However, this definition does not apply for conical and pyramidal indenters. Thus, based on their observations, Oliver and Pharr introduced a geometric constant ε accounting for the effect of the indenter shape on the true contact depth, which is then defined as

$$h_c = h_{max} - \varepsilon \frac{P_{max}}{S}, \qquad \text{Eq. 3-5}$$

where h_{max} is the maximum depth reached during the test, ε is an empirical geometric constant, P_{max} is the maximum load reach during the test, and S is the slope of the upper part of the unloading curve. The value of the constant ε depends on the geometry of the indenter and is determined from experiments in many different materials. Woirgard and Dargenton [110] and then Pharr and Bolshakov [111] proposed to estimate the value of epsilon from the exponent of the power law fitting the unloading curve. Their analysis is

based on the concept of the effective indenter and on the Segedin's equations. This method has been used in this study. For Berkovich indenters, epsilon is ε=0.75.

The final step is to determine the projected area from the contact depth. In the case of an ideal Berkovich indenter, the area function is written as

$$A_p = 24.5h_c^2\,, \qquad \text{Eq. 3-6}$$

However, indenters always demonstrates a tip defect inherent to the fabrication of the tip itself but also because of a loss of ideality and shape with time. It is accounted for by regularly calibrating the area function by indenting a material of known modulus (usually Silica E=72GPa). Using the Sneddon relation (Eq. 3-3), the projected area is calculated for different values of h_c. The evolution of the projected area as a function of the contact depth is then plotted and fitted using a simple equation as proposed by Oliver and Pharr (Eq. 3-7)

$$A_p(h_c) = C_0h_c+C_1h_c + C_2h_c^{1/2} + C_3h_c^{1/4} + C_4h_c^{1/8} + C_5h_c^{1/16} \ldots \qquad \text{Eq. 3-7}$$

Summary of the nanoindentation technique

Nanoindentation is commonly used to determine the hardness and modulus of a material at a very small scale. The properties are determined from the load versus displacement curve, an example of which is shown on **Figure 3-8**. However, the projected area of the indenter must first be calculated. The first step to achieve that is to determine the contact depth h_c. Several methods have been proposed in order to analyze the indentation curve. Eq. 3-5 offers the definition of the contact depth by Oliver and Pharr. Once the contact depth is

determined, the function area A_p, describing the projected area as a function of the contact depth must be determined. Due to the inherent non-ideal shape of the indenter and its wear with time, the area function is regularly calibrated and can be fitted using Eq. 3-7. Once the area function is known, the hardness and modulus are calculated using Eq. 3-2 and Eq. 3-3.

3.2. The U-NHT "Ultra nano hardness tester" by ANTON PAAR

The nanoindenter in this study is a U-NHT "Ultra nano hardness tester" from ANTON PAAR. It has two symmetrical columns, one associated with the indenter head and one with an active reference (**Figure 3-9**). The advantage of the active reference is to remove the thermal drift problems usually associated with nanoindentation measurements. The reference and indenter head are 2.5 to 3mm apart from each other. Carefully preparing the sample surface and optimizing its flatness is necessary to ensure that both the indenter and the reference work in the same plane.

Each column possesses its own piezoelectric actuator, which controls its displacement. The displacements induced by the piezoelectric actuators are transmitted to the indenter and reference heads by two springs of stiffness K_1 and K_2 with one end attached to the piezoelectric actuator and the other end attached to either the indenter or the reference.

The device has the capacity to monitor the indenter head both in displacement and in force as opposed to more traditional devices for which the indenter is force driven only. The load applied by each column is calculated from the compression of the springs K_1 and K_2,

which is determined by the capacitive sensors C_1 and C_3 respectively. The displacement control capacity of the indenter head is derived from the differential capacitive sensor C_2 used to evaluate the displacement of the indenter head relative to the reference, maintained at a constant load. Moreover, the sample is fixed on a motorized table allowing displacements in the X and Y directions with a resolution of 1 μm. It is also equipped with two objectives lenses, x5 and x100.

In conclusion, the indenter column has independent load and displacement sensors. The thermal drift is almost null and the device possesses great mechanical stability thanks to the active referencing of the surface. The motorized X-Y table allows achieving large arrays of indentations.

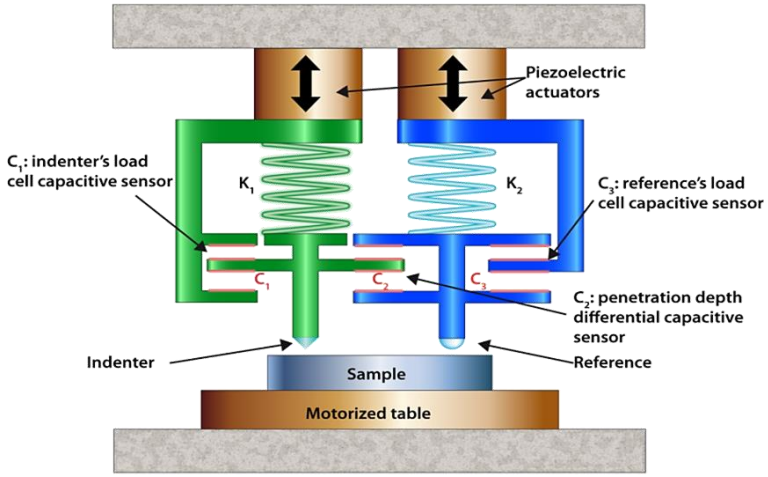

Figure 3-9. A schematic representation of the U-NHT nanaoindenter

3.3. The cartography method

The nanoindentation cartography can be backtracked to Ulm et al. [112] who stated that nanoindentation is mainly used to study homogenous materials. They were looking for a way to apply the nanoindentation technic to heterogeneous microstructures. In their efforts, they developed a method based on the statistical analysis of grid of nanoindentation. At that time, it was made possible by the development of motorized X-Y tables, which allow for accurate control of displacement of a sample between two indentations.

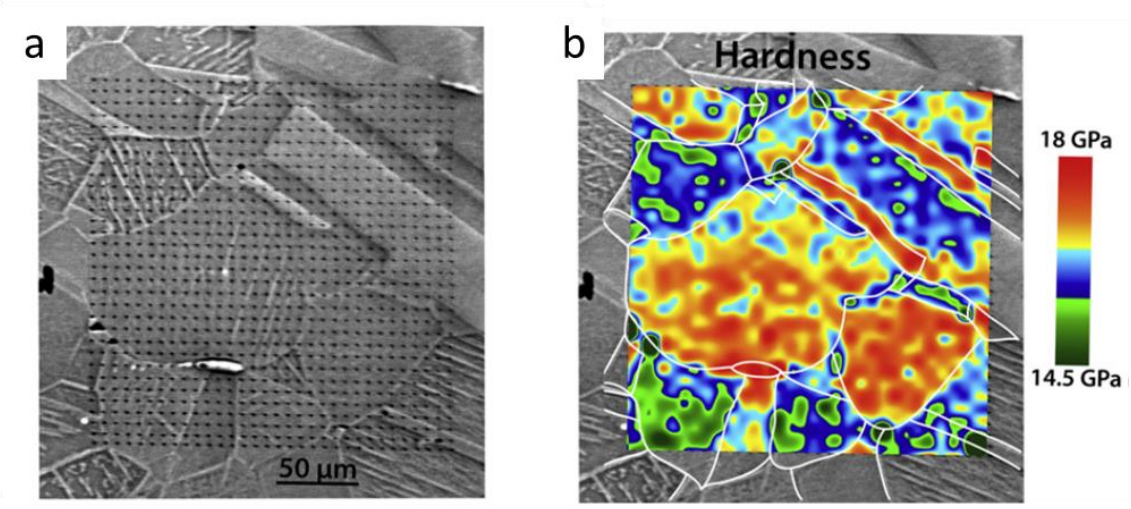

Figure 3-10. Hardness cartography applied to a plasma-nitrided 316 stainless steel (a) SEM image of the array of indentations used to reconstruct the hardness map (b) Hardness map revealing the heterogeneities of hardness of the microstructure [113]

The statistical analysis performed on the grid allows for extraction of the individual properties (hardness and modulus) of individual microstructural features provided that the resolution (e.g. step size) of the grid is satisfactory. Following the Work of Ulm et al., Randall et al. [114] and later Tromas et al. [113], [115] improved the technic by representing

the results as a surface map where each pixel represents a single nanoindentation test. A color chart is associated with the hardness and modulus values, and a bicubic interpolation is applied to build the map from the discrete dataset. The surface of the sample can then be represented in terms of its hardness or modulus values.

Figure 3-10 illustrates the method applied to the characterization of a plasma-nitrided polycrystalline stainless steel. First, a regular array of indentations is made. The size and depth of the indentations are selected to minimize the step size of the array, and thus increase the resolution of the cartography while ruling out the influence of the surface morphology. An interpolation method is applied to build the map from the discrete dataset and a color chart is associated with the hardness or modulus values. The choice of the interpolation method is important because it can lead to artifacts on the maps. For instance, in the case of a two-phase material having highly dissimilar properties, a bicubic interpolation artificially underestimates or overestimates the interpolated value at the interface. Therefore, in some cases, the nearest neighbor interpolation will be preferred.

4. Characterization of the microstructures

The microstructures were observed at different scales using several microscopy techniques including Scanning Electron Microscopy (SEM), Atomic Force Microscopy (AFM), and Transmission Electron Microscopy (TEM). Details on the equipment and conditions used are given.

4.1. Scanning electron microscopy

Scanning electron microscopy is used to image organic and non-organic specimens with a resolution ranging from the nanometer to the micrometer. The area of interest is scanned with a very thin focused electron beam (few nanometers of diameter) which can be moved across the sample surface or maintained in a specific area. The imaging signals are produced from the interaction of the electron beam with the sample and include secondary electrons, backscattered electrons, characteristic x-rays, and photons of various energies. These signals are obtained from specific emission volumes within the sample and can be used to examine many characteristics of the sample (surface topography, crystallography, composition, etc.) [116].

A JSM-7001F-TTLS scanning electron microscope from JEOL was used throughout the study. It is equipped with a field emission gun that generates a very fine probe of 1 to 2nm diameter. The system is equipped with secondary and backscattered electron detectors and both of them will be used depending on the nature of the observation necessary. Acceleration voltage ranging from 5 to 20kV were used.

An Energy Dispersive Spectroscopy (EDS) system is installed in the SEM chamber and allows for chemical characterization of the samples. Chemical analysis was performed at 10kV and before each EDS scan the system was calibrated for photon energy using a cobalt target.

4.2. Atomic force microscopy

The atomic force microscopy is based on the measurements of the forces of interaction between the atoms of a tip attached to a cantilever beam and the surface of the material. The forces are recorded by measuring the deflection of the cantilever beam by recording the deviation of laser reflected from the back of the cantilever.

The AFM was carried out using a Dimension 3100 microscope from Brucker (Santa Barbara, CA) in tapping mode in order to characterize the surface resulting from the sample preparation. The AFM files were processed using WSxM software [15].

4.3. Transmission electron microscopy

The TEM possesses very high resolution compared to the SEM. In some cases, features as small as a few tenths of nanometers can be imaged. As opposed to SEM, TEM relies on the detection of electrons transmitted through the sample, which requires very thin specimens to be used (around 100nm thick).

A Philipps CM20 microscope operating at 200KV was used for the observations of the microstructure at the nanometer scale. For further analysis, a JEM-2200FS microscope from JEOL was used. It is equipped with a scan generator, which enables scanning transmission electron microscope (STEM) operations. It is also equipped with Energy Dispersive Spectroscopy (EDS) and Electron Energy Loss Spectroscopy (EELS) systems for chemical

analysis. Our specimen was too thick to be analyzed by EELS so only EDS was used for chemical characterization.

The specimen was prepared using the Focused Ion Beam (FIB) lift-out technique. The Helios Nanolab G3 CX DualBeam FIB/SEM from FEI equipped with a Gallium source was used. The FIB lift-out technique allows for the preparation and extraction of a thin foil from the specimen by ion milling for TEM observations.

The TEM was used to image the microstructure of a cell wall at the nanoscale scale. Both the precipitates and dislocations are characterized. Moreover, EDS analysis was performed in the dendritic phase to identify the composition of the precipitates.

CHAPTER FOUR

Characterization of mechanical properties at the interface HVOF

Grit blasting with alumina particles is a conventional method used to prepare substrate surfaces in order to improve the adhesion of thermal spray coatings. However, this process modifies the microstructure of the substrate and may weaken the interface. This chapter presents an original experimental approach to characterize by nanoindentation the local mechanical properties of a 17-4PH steel substrate at the interface with a cermet Cr_3C_2-NiCr coating and to correlate these properties to the microstructure. In particular, the effect of grit blasting of the substrate with alumina particles, used to modify its roughness and improve the coating adhesion, is discussed.

1. Microstructural characterization

In this section, the microstructures of the coating and substrate are presented with a strong focus on the interfacial region. The microstructures of both the coating and the

substrate results from the surface treatment and the coating deposition. The individual contributions of the grit blasting and the coating deposition are discussed.

1.1. Microstructure of the interface: residual alumina particle

Figure 4-1 illustrates the microstructure of the interface in cross section. The sample was grit blasted with alumina particles before deposition of the coating and final polished by chemical mechanical polishing (CMP) following the procedure presented in chapter 2. Residual alumina particles are clearly visible. As indicated in the figure, the particles can be either trapped at the substrate surface or completely embedded in the substrate. The diameter of the residual particles varies but averages around 20µm. The roughness of the substrate is also clearly visible highlighting the impact of grit blasting on the substrate surface. The peak-to-valley roughness ranges between 10 and 20µm.

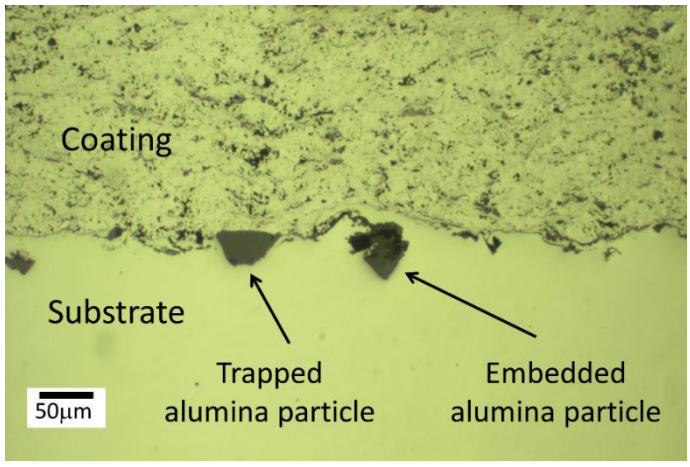

Figure 4-1. Optical micrograph showing the microstructure at the interface. Residual alumina particles introduced by the grit blasting are visible.

The presence of residual alumina particles is not surprising and is revealed by the polishing procedure. Indeed, the use of CMP permits to maintain the integrity of the interface and the alumina particles and reveal microstructural details not discernable otherwise. Residual grits are a common problem in the industry because considered as detrimental for the adhesion. When trapped, the particles modify the wetting properties of the coating particles during the deposition and impede the interaction between the coating and the substrate resulting locally in poorly bonded regions [117], [118]. Embedded alumina particles originate from an important deformation of the substrate overlaying the particles during the process. It is usually associated with a complex surrounding stress state that can lead ultimately to failure. [119]–[121]. The blasting was here followed by flame cleaning to reduce embedded inclusions. However, the technique is not effective in removing all residual particles.

1.2. Coating microstructure

Figure 4-2a shows the initial powder imaged by electron microscopy. The powder is homogeneous in size and the grains are hollow. **Figure 4-2b** illustrates the microstructure of the as-sprayed coating. The dark particles are the carbides while the remaining material is the NiCr binding matrix. The grey contrast observed in the matrix corresponds to different Ni content. The brighter the matrix is, the more nickel it has. Conversely, the darker regions of the Ni-Cr matrix correspond to higher chromium content. The results of EDS in the coating shown in **Figure 4-3** confirm this observation.

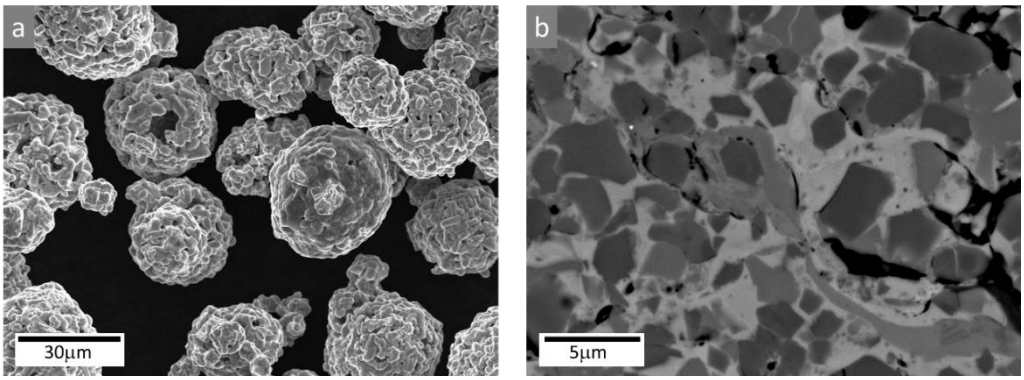

Figure 4-2. (a) SEM image of the initial powder. (b) Typical microstructure of the as-sprayed coating obtained from the powder shown in (a) (SEM).

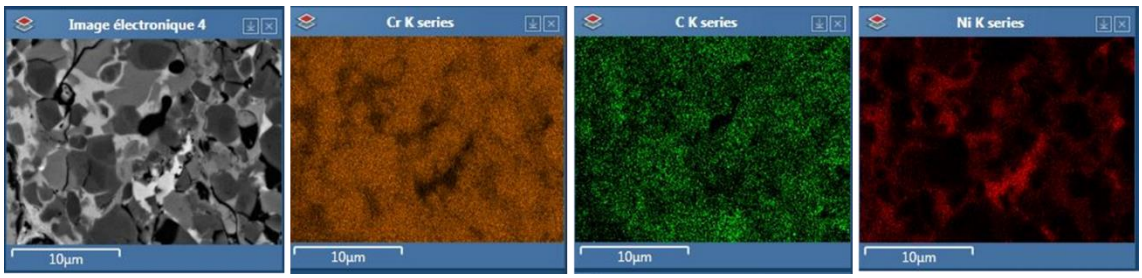

Figure 4-3. EDS analysis performed in the coating. The brighter regions are associated with low Cr content and high Ni content

A FIB secondary ion image of the coating matrix is shown **Figure 4-4**. FIB secondary ion imaging is sensitive to chemical differences and this imaging mode is especially useful here. It reveals small grains below 1µm in diameter having distinct grey levels suggesting different phases with various Ni and Cr content forming during deposition. The influence of the microstructural features of the coating on the mechanical properties and adhesion in this very same system were investigated elsewhere [22].

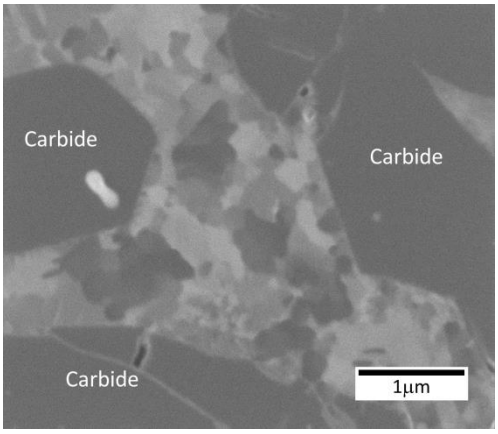

Figure 4-4. FIB image revealing small grain inside the NiCr matrix

1.3. Substrate microstructure

The substrate is a 17-4PH martensitic steel whose composition is detailed in Chapter 2. Its characteristic microstructure is shown in **Figure 4-5a**. The material exhibits a lath martensitic microstructure long known in the literature [122], [123]. However, it was not until recently and the use of technique such as EBSD that the exact details of the microstructure were elucidated [124]. **Figure 4-5b** depicts the delta ferrite stringers revealed by the polishing procedure.

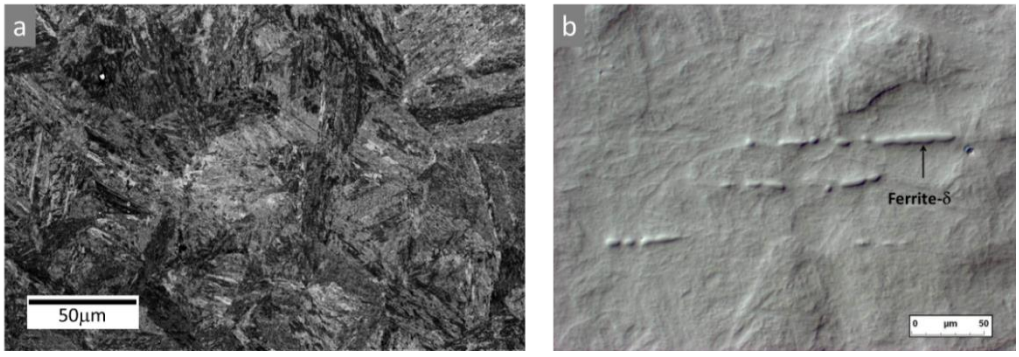

Figure 4-5. (a) SEM image of the microstructure of the 17-4PH martensitic steel substrate. (b) Optical microscopy image of the δ-ferrite.

Figure 4-6a depicts the microstructure of the substrate near the coating/substrate interface. Two microstructurally dissimilar regions can be distinguished inside the substrate. The region just beneath the interface is associated with an ultrafine-grained microstructure and is about 10-20μm. The rest of the substrate is characterized by a grain size gradient up to the point where the process does not affect the microstructure anymore and the common lath martensitic structure is observed.

The nanostructured and refined layers are enlarged in **Figure 4-6b**. The nanostructured layer follows the roughness variations of the interface.

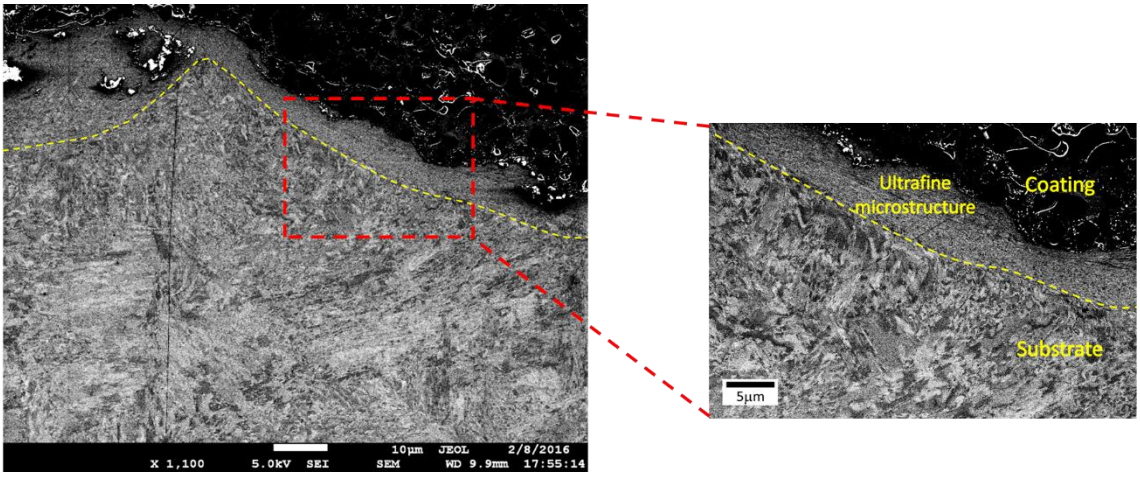

Figure 4-6. SEM images of the microstructure of the substrate at the coating/substrate interface

The SEM image in **Figure 4-6b** reveals that the microstructure of the substrate is affected during the deposition process. The grain refinement mechanisms most likely originate from the strain induced in the material by the sprayed particles during grit blasting and coating deposition. It is similar to what is observed in other mechanical treatment techniques such as shot peening and severe plastic deformation processes where the

nanostructure results from the large strain induced. The gradient of microstructure is therefore a consequence of a strain gradient along the substrate thickness.

Summary of the microstructural characterization of the coating and substrate

The coating is a cermet composite made of carbides embedded in a NiCr matrix. The observations of the NiCr matrix using FIB imaging revealed multiple grains of few hundreds of nanometers and having different contrasts. The difference of contrast suggests different compositions of the grains. Such inhomogeneities in the coating reflect the complexity of the coating process, which induced various stress states and thermal gradients.

The interface is not flat because of grit blasting and the presence of residual alumina particles, which can be either trapped at the substrate surface or embedded inside the substrate volume, was illustrated.

The substrate is a 17-4PH martensitic steel. Its microstructure was imaged using OM and SEM. Distant from the interface, the microstructure of the substrate shows a classical lath martensitic structure and ferrite-δ stripes. At the interface, a nanostructured layer of $\approx$10μm has formed. The rest of the substrate is characterized by a grain size gradient up to the point where the process does not affect the microstructure anymore and the common lath martensitic structure is observed. The microstructure can be schematically represented as shown in **Figure 4-7**.

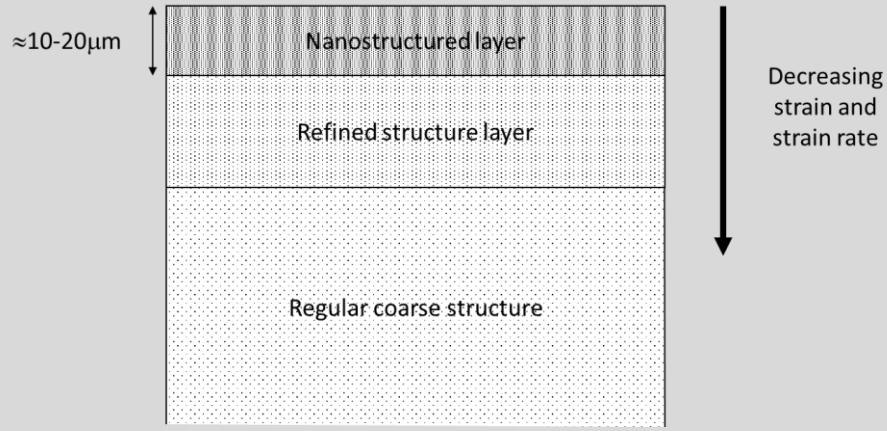

Figure 4-7. Schematic representation of the substrate surface. The gradient of microstructure is associated with a gradient of strain produced by the impact of the grit blasting particles.

2. Significance of grit blasting on the mechanical properties of the substrate

2.1. Surface characterization for nanoindentation

Nanoindentation requires very high standards regarding the surface condition. Those standards are achieved by carefully preparing the surface through several grinding and polishing steps as described in Chapter 2. Atomic force microscopy is used to inspect the surface condition after final polishing. The results are shown in **Figure 4-8**.

Figure 4-8b is the 3D representation of the picture shown in **Figure 4-8a**. The line represents the position of the height profile shown in **Figure 4-8c**, which shows that the coating is standing 150nm above the substrate, resulting from different polishing rate during sample preparation. The slope of the profile extends over 12µm corresponding to a slope of approximately 0.7°. A Root Mean Square (RMS) roughness of about 3nm was achieved in

the 17-4 PH substrate. Both the slope and the roughness will be sufficient for the nanoindentation measurements.

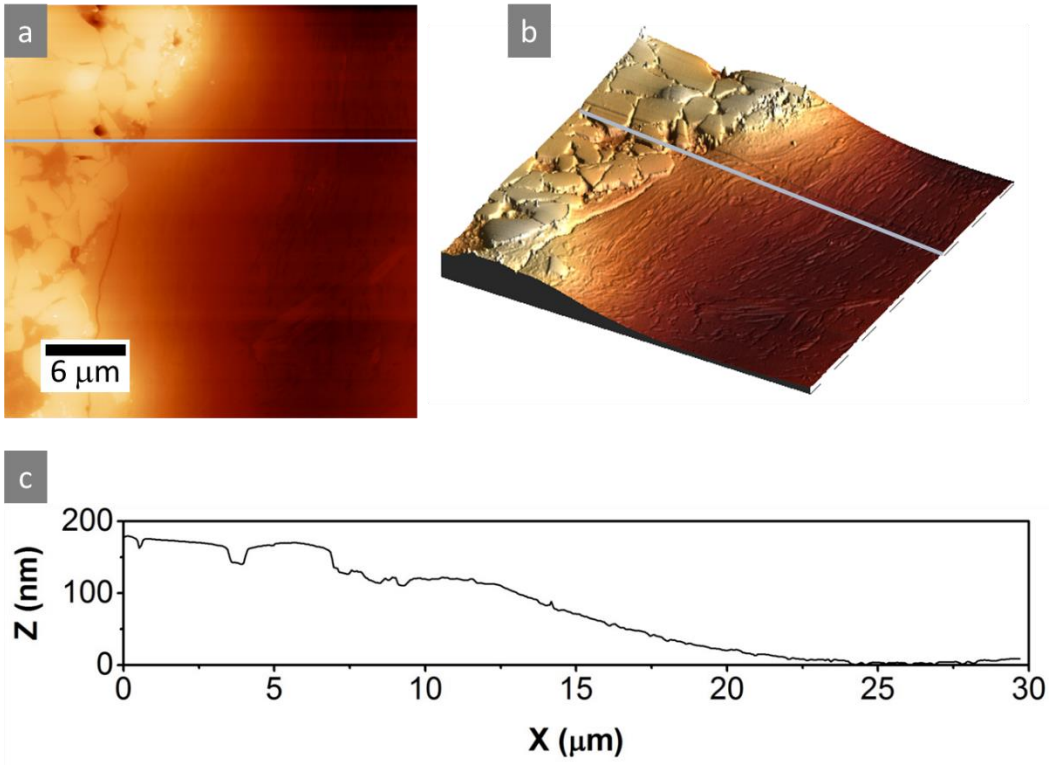

Figure 4-8. (a) AFM topography image of the surface at the interface after CMP with colloidal silica. The blue line represents the position of the profile shown in the figure (c). (b) 3D representation of the topography image shown in (a). (c) Height profile at the interface.

2.2. Nanoindentation cartography of the substrate

2.2.1. Experimental details regarding the nano-indentation cartography technique

Figure 4-9a illustrates the loading sequence used during the nanoindentation tests in this chapter. The loading is performed in depth control to ensure that each of the indentations has the same maximum penetration depth, without regard to hardness. The unloading is performed in load control at 4000µN/min. The step size of the arrays for the

reconstruction of the hardness and Young's modulus cartographies may vary depending on the area tested.

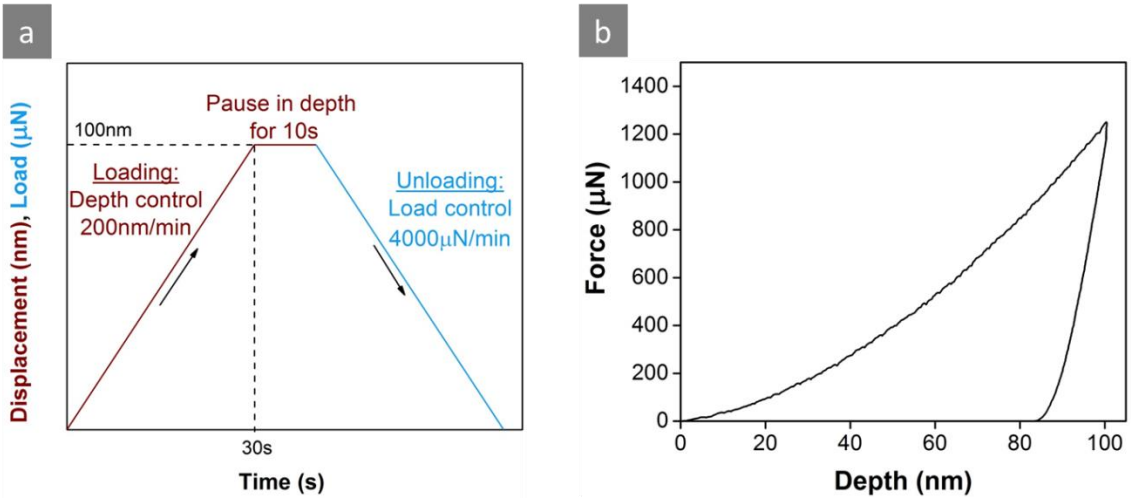

Figure 4-9. (a) Indentation profile. The loading is depth controlled to assure a constant penetration of all the indentations while the unloading is load controlled. (b) Typical indentation curve of the substrate obtained with the procedure showed in (a).

Figure 4-9b shows a typical nanoindentation curve of the substrate obtained by using the indentation profile shown in **Figure 4-9a**. At the displacement peak (i.e. 100nm), the force is ≈1200MPa and during unloading, the substrate demonstrates little elastic recovery since h_p≈83nm.

2.2.2. Calibration of the nanoindentation cartography and validation of the method

It is to the experimenter to adjust the parameters of the cartography in order to reach the desired result. They can include the step size of the array, the depth of the indentations, the interpolation algorithm, the color chart, etc. The manual adjustment of these parameters is not an easy work and is specific to every material tested. It usually requires one or two

attempts to optimize the method. A critical parameter is the interpolation algorithm to transform the discrete hardness or Young's modulus data into a map. The method is detailed in Chapter 2. **Figure 4-10** is an attempt to calibrate the cartography. It shows the same array with two different interpolation methods. The step size of the array is 3μm and a maximum depth of 100nm was used. **Figure 4-10a** was reconstructed using a nearest neighbor interpolation and **Figure 4-10b** using a bicubic interpolation. The nearest neighbor is the simplest and most faithful way to represent the discrete dataset since it does not generate intermediate values. Instead, the algorithm determines the pixels to be interpolated and assign them the value of the nearest data point. On the other hand, the bicubic interpolation generates values between two neighbor data points using a polynomial function. While the nearest neighbor method is more faithful, its representation is not smooth and can sometimes bring complexity in the interpretation of the map. The bicubic method produces smoother images and easy interpretation of the results. However, it can be subjected to interpolation artifacts, in case of abrupt variations, that can lead to physically incorrect interpretation of the results.

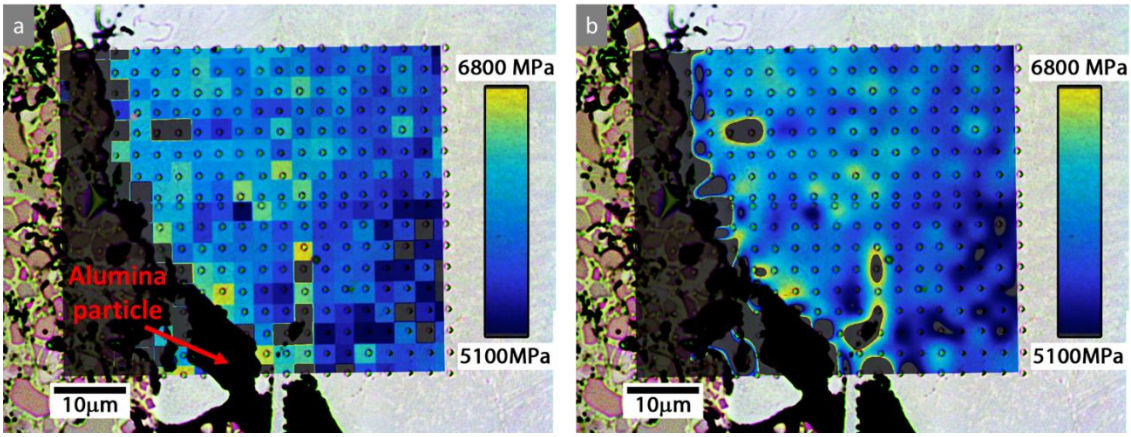

Figure 4-10. Nanohardness cartography at the coating/substrate interface reconstructed from a 20*17 array using (a) nearest neighbor interpolation (b) Bicubic interpolation. The coating is on the left side and was voluntarily saturated to increase the contrast for the representation of hardness in the substrate.

In **Figure 4-10**, both figures results in similar results and reveals higher hardness values at the interface compared to the bulk. The values range between 5100 and 6800MPa. The bottom right region of the maps depicts lower hardness values compared the top left corner of the image. It is unclear whether the results reflect a gradient of hardness or an isolated region having low hardness values. The indented area is small and a larger array prolonged in the bulk of substrate bulk would be necessary to address this observation. Moreover, the presence of residual alumina particles at the interface distorts the results.

The bicubic representation gives a smoother image, which makes it easier to detect the hardness variations and will be preferred for the rest of the chapter. In addition, no interaction between neighboring indentations is observed validating the indentation parameters. The maximum depth of 100nm results in indentations having an average equivalent diameter of 700nm. The step size and maximum indentation depth chosen for

this attempt are a good compromise between minimizing the interaction of neighboring indentations while having a good lateral resolution for the cartography. Those parameters will be used for the following cartographies.

2.2.3. Cartography of a grit blasted sample

Once we determined the correct parameters to use, the cartography method was apply to investigate properly the properties of the substrate at the interface. **Figure 4-11** shows the hardness cartography determined from an array of 765 indents. The step size between each indentation is 3µm and each indentation follows the profile shown in **Figure 4-9a**. For a better analysis, the color scale has been adjusted to the substrate hardness values (the coating hardness values have been saturated and appear in grey contrast). The substrate presents a hardness gradient ranging from 4700MPa at 100µm away from the interface, up to 5800MPa at the interface. The Young's Modulus was also measured and no trend is observed on the cartography. It remains constant throughout the substrate thickness at 219 ± 12GPa. A similar value of 225GPa using the same method was found [125], thereby validating the hardness nanoindentation measurements. Moreover, the use of displacement control ensured that all indentations have the same size so that artifacts associated with any possible tip calibration uncertainties or with indentation size effect are averted.

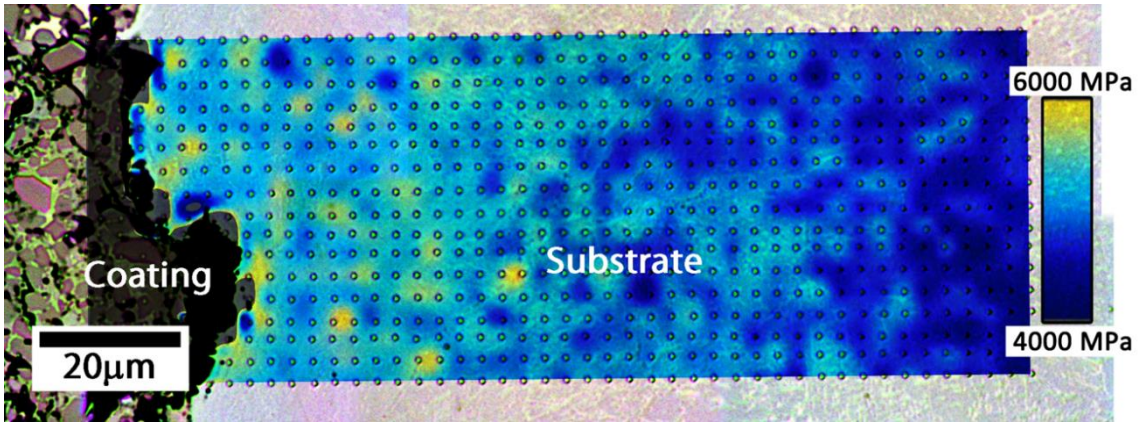

Figure 4-11. Nanohardness cartography built from a 17*45 nanoindentations array at the interface between the coating and the substrate. The hardness map is superimposed to the optical microscopy image of the indented area. The substrate surface was grit blasted with alumina particles prior to the deposition of the coating.

In order to confirm the stabilization of the hardness values away of the interface, a complementary 6*30 array was built. **Figure 4-12a** illustrates the complete nanohardness cartography including the original array and the complementary one. **Figure 4-12b** and **c** depict the evolution of hardness and Young's modulus respectively, as a function of the distance from the interface. Both profiles were calculated by averaging the hardness values over each column of indentations. The hardness gradient is clearly observable from the interface up to 100µm away of the interface. From there, the hardness remains stable around 4800MPa. The Young's modulus is constant throughout the entire indented area oscillating around 220GPa.

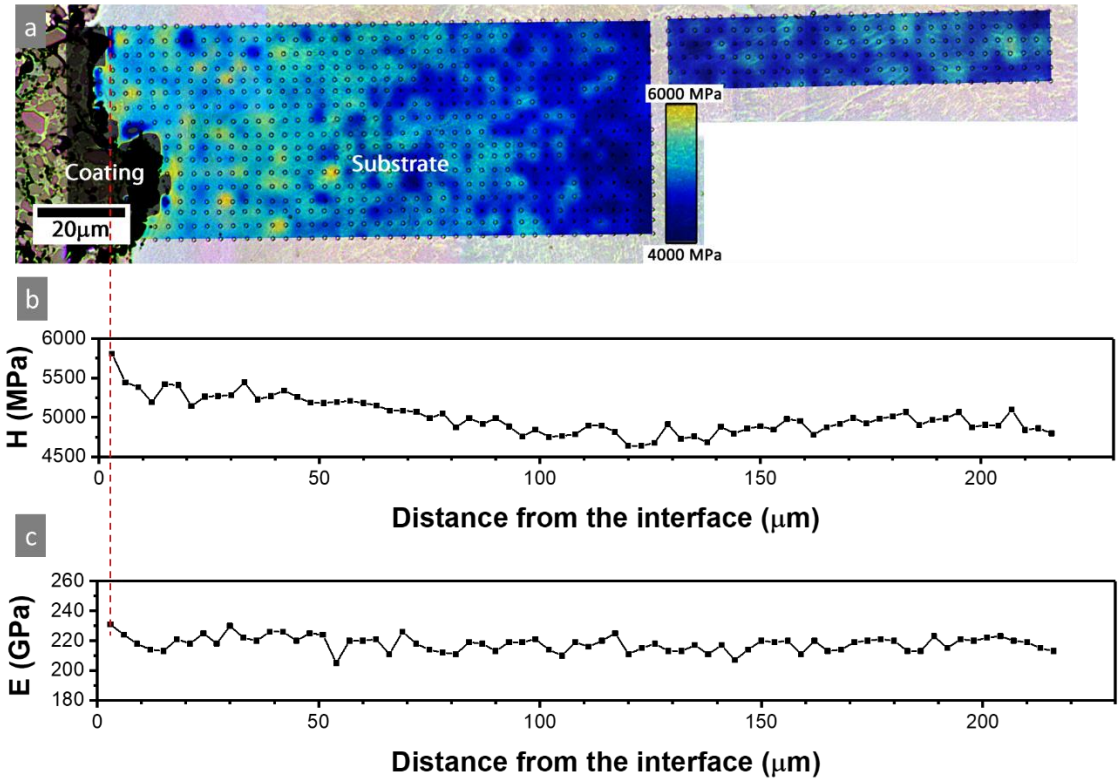

Figure 4-12. (a) Complementary nanohardness cartography built from a 6*30 nanoindentation array (b) Hardness as function of the distance from the interface. The hardness remains constant

A strong increase of the hardness is observed with a gradient of about 11MPa/µm and a hardness reaching a maximum of 5800MPa close to the interface. The hardness increase can have several consequences on the adhesion of the coating. First, it is likely to promote brittleness and modify the surface fatigue properties of the substrate. Furthermore, it can affect the coating build-up during the early stage of deposition. Indeed, research conducted by Gao et al. [126] revealed that a higher hardness of the substrate is associated with more particles rebounding from the substrate surface during the first stage of deposition.

2.2.4. Cartography of a non-grit blasted substrate

From the results shown in **Figure 4-12**, the source of the hardness increase is not clear. At this point, both the grit blasting and the coating depositing could be responsible as they both involve high kinetic energy particles. In order to address this issue, the surface of another substrate was polished up to 1µm instead of being grit blasted. The coating was then deposited on the polished surface. Thus, only the contribution of the coating deposition is investigated and is separated from the one of the grit blasting. **Figure 4-13** shows the hardness cartography of the non-grit blasted substrate determined from 450 indents. The nanohardness remains constant throughout the substrate thickness at approximately 4700MPa.

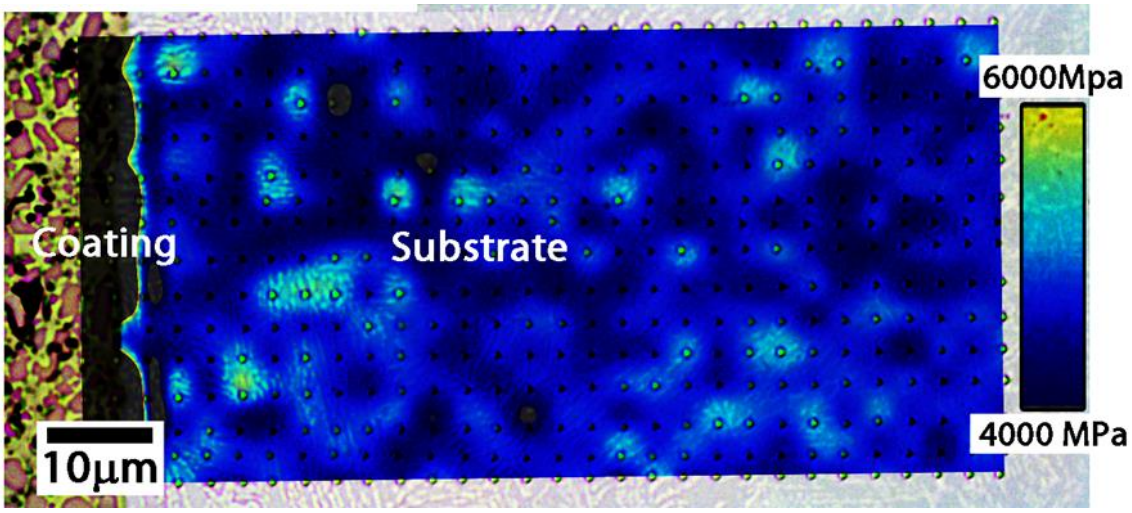

Figure 4-13. Nanohardness cartography built from a 15*30 nanoindentation array at the interface between the coating and the substrate. The substrate was polished with a diamond solution up to 1µm prior to the deposition of the coating. No hardening is observed in the substrate.

The non-grit blasted sample exhibits no evidence of hardness gradient in the substrate. Comparison with the cartography of the grit blasted sample shown **Figure 4-11** shows that grit blasting the substrate surface modifies its mechanical properties and increases the hardness. It also demonstrates that the coating deposition, despite high kinetic energy involved, does not induce any visible changes of the mechanical properties of the substrate whereas one would have expected some hardening due to the impact of the carbides contained in the coating and the temperature involved.

2.2.5. Impact of grit blasting on the substrate microstructure

The grit blasted substrate exhibits an evolution of its microstructure as we move away from the interface. The high hardness values in **Figure 4-12** appear to coincide with the modified microstructure unveiled in **Figure 4-6**. The highest values are localized near the interface where the microstructure is highly affected and made of nano-sized grains. It suggests that the hardness gradient reflects an evolution of the microstructure and that the microstructure is no longer affected beyond 100µm from the interface. The relationship between hardness and microstructure was further investigated by imaging the microstructure of the array shown in **Figure 4-12**. **Figure 4-14b** was taken in the bulk where the substrate has not been affected by the grit blasting process. The microstructure is a regular lath microstructure characteristic of martensitic steels [127]. **Figure 4-14a** was taken in the substrate, a few microns away of the interface, where the substrate is highly affected by the

grit blasting process. The lath microstructure disappeared, replaced by a finer-grained structure.

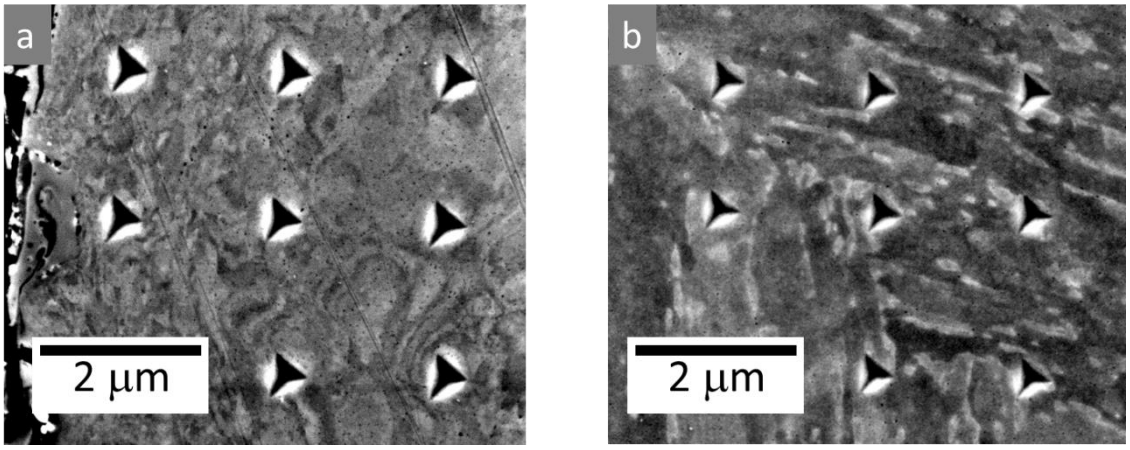

Figure 4-14. Electronic microscopy images revealing the microstructure of the substrate taken a) away of the interface b) at the interface. The microstructure at the interface is made of very small grains associated with deformation patterns while the microstructure in the bulk shows a regular lath microstructure.

The comparison of the microstructure shown in **Figure 4-14a** and **b** suggests that the high values of hardness measured at the interface are related to a grain refinement induced by the grit blasting process. Several papers have reported a change of microstructure when blasting high velocity particles on a metallic surface. The mechanisms of refinement are similar to the one observed in severe plastic deformation processes such as high-energy shot peening or surface mechanical attrition treatment [128]–[130]. The plastic strains induced by the impacting particles are accommodated by a change of microstructure through dislocation motion and grain subdivision [131]. A gradient of microstructure and mechanical properties is usually observed in the impacted material because of the gradient of strain and strain rate induced.

2.3. Indentation size effect

A clear gradient of hardness was exposed and an increase of hardness of ≈20% at the interface was measured compared to the bulk values. The nanoindentation cartography has been performed at a low penetration depth (100 nm) in order to reduce the matrix step size and thus to increase the spatial resolution. At such small indentation depths, it is common that materials appears to be harder than at larger indentation depths and the validity and significance of the hardness values we presented can therefore be questioned. For this reason, the effect of the penetration depth on the hardness measurement or indentation size effect (ISE) was investigated.

Indentation size effect (ISE) describes the scale dependence observed in various materials for which the hardness increases with decreasing the indentation size. In order to characterize a potential ISE in the substrate, fifteen rows of indents were made containing 15 indentations each for a total of 225 indentations. Each row corresponds to a different maximum penetration depth ranging between 80 and 700nm. The indentations were made in the bulk where the microstructure and hardness are considered homogeneous. The results of the ISE characterization are presented **Figure 4-15**. Each data point is an average of 15 hardness values. The hardness remains constant throughout the range, which indicates that there is no scale-dependence in the hardness values. The uncertainties at small penetration depths remain acceptable, which further validates the indentation procedure used.

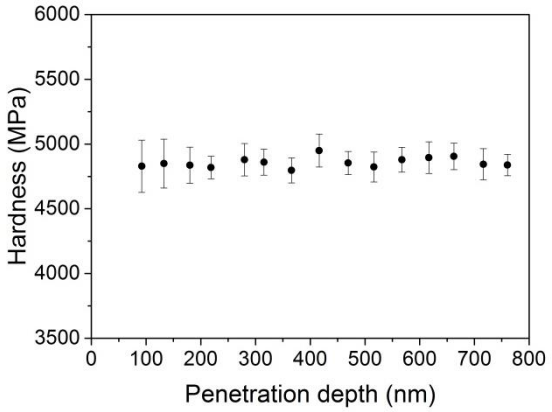

Figure 4-15. Nanohardness as a function of the penetration depth for ISE investigation. Each data point is the average of 15 hardness values obtained from indentations made at the same depth for a total of 225 indentations. The errors bars correspond to the standard deviation calculated from those 15 values.

2.4. Embedded alumina particles

The consequences of the grit blasting on the substrate hardness and microstructure were investigated above. In this section, we examine the local impact of grit blasting on the substrate by imaging and mapping the hardness of an embedded alumina particle. As mentioned in Chapter 1, grit blasting leaves residual particles on the substrate surface, which can adhere to the substrate or completely embed into the substrate surface.

The surface preparation is critical to ensure accurate measurements around the alumina particles. The profile shown in **Figure 4-16** was taken across the alumina particle shown in **Figure 4-17**. The risk of the surface preparation, in the case of heterogeneous microstructures, is to favor one phase compared to another, which would results in a non-flat surface. However, as seen on the profile, our procedure allowed us to avoid this problem

and even in the close vicinity of the particle, the slope induced by the surface preparation is very small (≈0.7°).

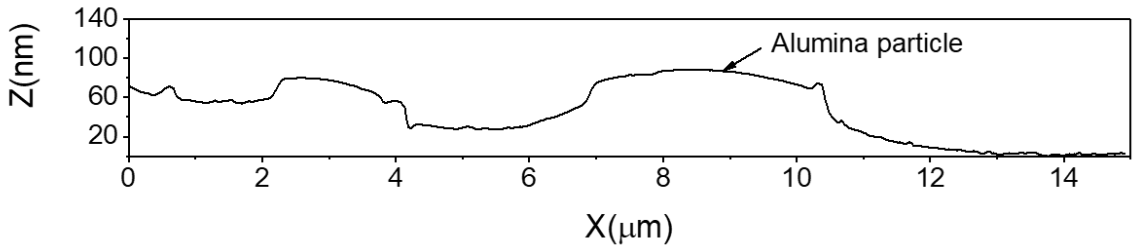

Figure 4-16. Height profile around the particle along the blue line shown in Figure 4-17b.

Figure 4-17 illustrates the steps in performing and analyzing the cartography from a 12*15 indentations array around an alumina particle. The SEM image (**Figure 4-17a**) of the indented area was taken using back scattered electrons. Using a step size of 2μm provides a better resolution for the characterization of this ultra-fine-grained microstructure. The yellow dash line separates this microstructure from the rest of the material. The diameter of the affected region is about 2-3μm. Small cracks nucleating from the particle (see red arrows on **Figure 4-17a**) and propagating into the substrate are clearly observable. An AFM image of the particle is shown **Figure 4-17b**. It shows deformation patterns on the surface which follows the ultra-fine-grained microstructure observed in **Figure 4-17a**. In addition, the high resolution AFM resolves surface features for correlation with the hardness cartography shown in **Figure 4-17c**. A nearest neighbor interpolation method was used to reconstruct the hardness map.

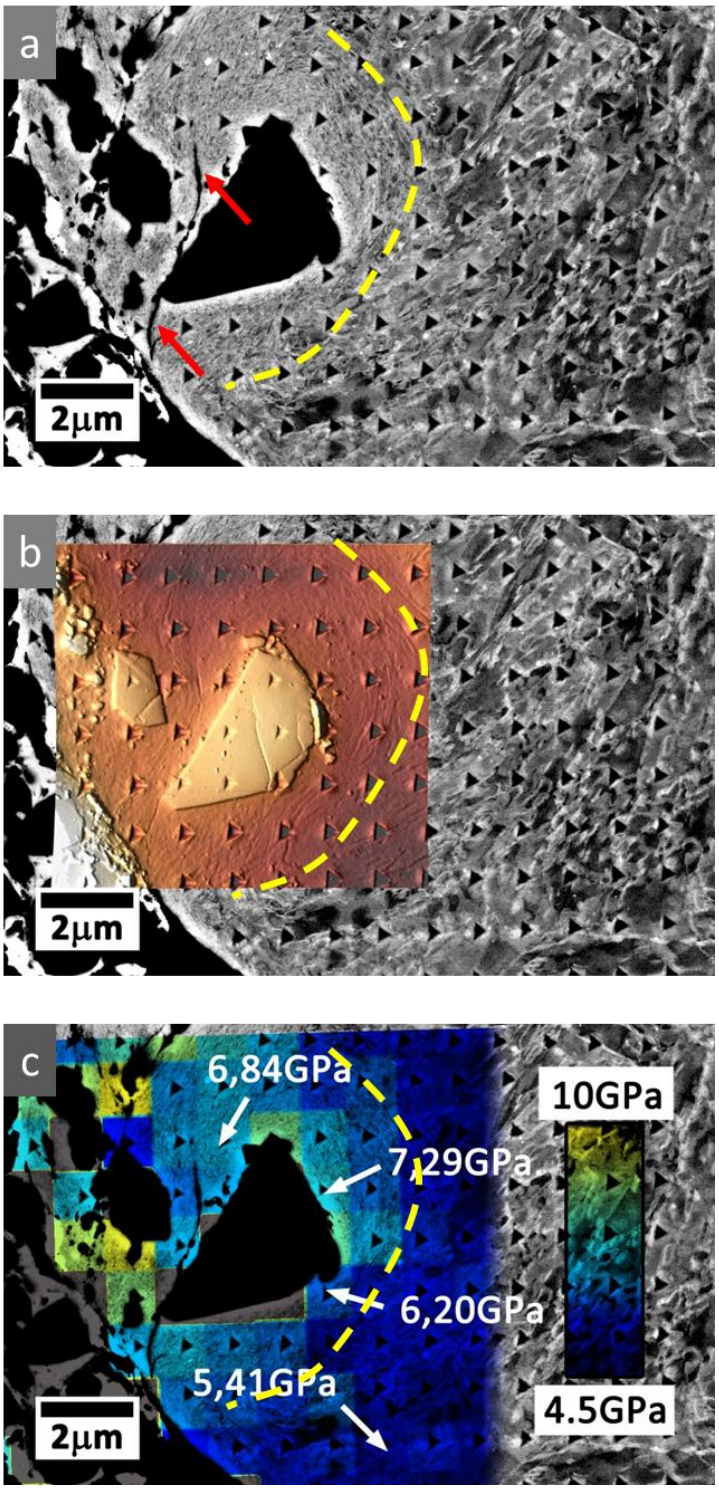

Figure 4-17. Nanoindentation array on an alumina particle. (a) SEM image showing the microstructure around the particle. The yellow line delimits an ultra-fine-grained structure in the vicinity of the particle. (b) Same area imaged by AFM (3D top view) (c) Nanohardness map around the alumina particle.

Figure 4-17c suggests that the hardness is notably higher in the vicinity of the particle. However, the hardness variations apply over very short distances, which make it difficult to extract clear information from the hardness map. To address this issue, one could think of increasing the resolution of the cartography by decreasing the step size of the array but further decreasing the step size would induce interactions between neighboring indentations. One solution is then to look at the individual hardness values as shown in **Figure 4-17c**. The hardness values of the ultra-fine-grained region (delimited by the yellow dashed line) are ranging from 6.2 to 7.3GPa. Outside this region, the hardness ranges between 5.1 and 5.9GPa. The SEM and AFM observations suggest that the vicinity of embedded alumina particles is severely altered and the mechanisms of refinement described earlier take place to a greater extent.

It is commonly thought that the coating/substrate interface is the preferential path for failure. However, the presence of cracks around the embedded particles (red arrows in **Figure 4-17a**) indicates that the particles act as stress raisers and are preferential sites for crack nucleation. Additionally, we can also observe that those cracks propagate in the substrate, in the layer of affected microstructure, which suggests that the coating/substrate interface is not necessarily where the failure will occur. It is confirmed by the nanohardness cartography results, which indicate that the area surrounding the particles has higher hardness, which is likely to promote brittleness and thus crack propagation. **Figure 4-18** further illustrates the crack propagation in the substrate. In both optical images, a crack

nucleating from the edge of the alumina particle and propagating through the substrate is observable.

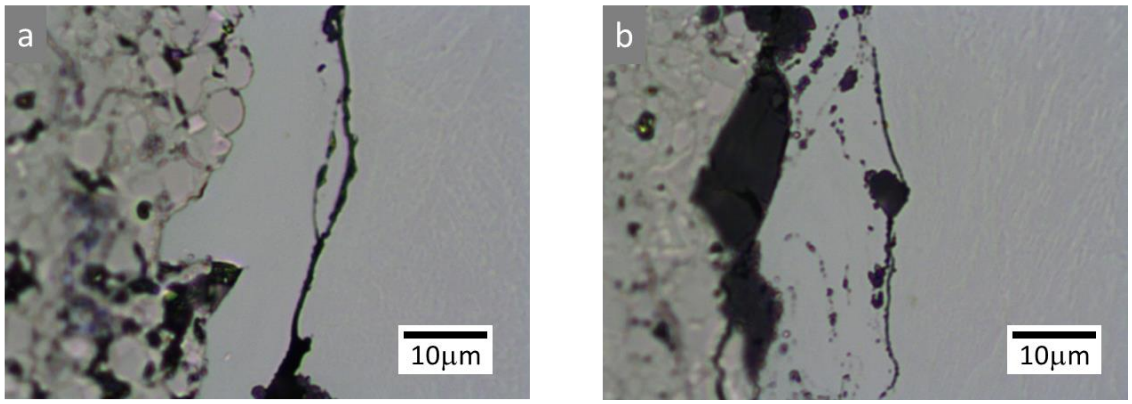

Figure 4-18. (a) and (b) Optical images showing cracks propagating from an alumina particle through the substrate.

2.5. General discussion

It was demonstrated that the surface of the substrate is highly affected by the whole coating procedure. Both the mechanical properties and microstructure exhibit an evolution when we move away from the interface. The grit blasting procedure, applied to optimize the substrate surface before deposition of the coating, is responsible for these effects. The adhesion of the film is impacted as the substrate become more brittle, which favors the propagation of cracks in the case of interfacial failure. However, the most harmful consequence of grit blasting resides in the residual grits remaining on the substrate surface. These particles act as stress raisers and preferential sites for crack nucleation which was confirmed by the presence of numerous cracks nucleating from embedded alumina particles.

Thus, in order to optimize the performance and lifetime of those materials, it is crucial to minimize the presence of such defects by optimizing the manufacturing parameters.

The method developed in this work successfully exposed and distinguished the issues related to the interface and the embedded alumina particles. It gives access to complementary information about the mechanical properties and the microstructure. Controlling the size and parameters of the indentation array allows investigating the interface at different scales.

This work was the result of a strong collaboration with an industrial partner. Unfortunately, the constraints associated with such study did not allow exploring further the adhesion mechanisms. Several experiments were envisaged but could not be initiated. The crack propagation around an alumina particle could be characterized by reconstructing its path inside the substrate. Sequential polishing or FIB milling are good ways to achieve that. The influence of the spraying parameters could be examined and applying the method described here for different processing conditions would give valuable information.

3. Conclusion of the chapter

The impact of grit blasting on a 17-4PH steel substrate coated with a cermet Cr_3C_2-NiCr coating was investigated using an original method based on nanoindentation cartography coupled to microscopic observations. Despite the beneficial effect of grit blasting on adhesion through roughness modification, it was shown that the grit blasting process affects the

microstructure and mechanical properties of the substrate subsurface (an average increase of more than 20% in hardness at the interface compared to the bulk values was measured). The impact of the coating deposition process on the substrate was shown to be close to zero. The potential adverse effects of the grit blasting treatment were confirmed by a local investigation of an embedded residual alumina particle. The SEM and AFM imaging, coupled to the hardness map reconstruction from nanoindentation measurements, revealed an ultra-fine-grained microstructure associated with a further, and very local, increase of hardness (40% higher than the bulk values). Cracks nucleating from the edge of the particle were also observed suggesting that failure could preferentially occur in the layer affected by the grit blasting and not at the coating substrate interface.

Obviously, other factors could be more critical in understanding the failure of such systems. Failure in the coating or at the interface is more likely to occur. However, in a process of improving the performance of the coating, the local investigation of the impact of the substrate surface preparation is critical. Moreover, in light of the results presented in this chapter, the nanoindentation cartography method couple to high resolution imaging techniques could enable to reinterpret the adhesion problems of thermal spray coating deposited on grit blasted substrate.

CHAPTER FIVE

Multiscale characterization of the mechanical properties of an A359 aluminum foam

This chapter intends to characterize the mechanical properties of a multiscale composite materials. The relationship between mechanical properties and microstructure will be addressed. The material is an aluminum foam used in energy absorbing structures. Its properties are defined by the cellular structure as well as by the parent material properties of the foam. The method used in the previous chapter, which is based on nanoindentation cartography, will be further developed. Because of the complexity of the material, a descending scale approach was established to answer the dual dependence associated with the foam starting from the cell level (macroscale) up to the precipitates scale (nanoscale) and several new techniques are introduced.

The chapter is divided in three sections. One section will be focused on the characterization of the structure and microstructures while the other will be focused on the

characterization of the mechanical properties. Finally, in light of the results presented, the relationship between the microscale properties (microstructure and mechanical properties) and the macroscopic behavior of the foam will be examined.

1. Characterization of the structure and microstructures

The foam is characterized by adopting a multiscale approach. In this first section, corresponding to the characterization of the structure and microstructures, the results of the morphology quantification of the foam by X-ray tomography is first introduced. Then, the results of the microstructural analysis at the cell wall level by optical and electron microscopies are presented. Finally, A TEM analysis of the precipitates, corresponding to the nanoscale part of this section, concludes the characterization of the foam.

1.1. Macroscale characterization: characterization of the foam morphology by X-ray tomography

As explained in Chapter 2, two samples were used to characterize the morphology and are shown on **Figure 5-1a** and **Figure 5-1b** and will be referred as sample 1 and 2 respectively. To highlight the accuracy and the relevance of using such technique to analyze the morphology, a comparison of the same cross section obtained from a photograph and X-ray tomography of sample 1 is shown **Figure 5-1c**. The details of the structure shown on the photograph are perfectly reproduced on the corresponding tomographic image. The resolution used for this reconstruction (e.g. voxel size of 30 and 24µm) is enough to capture

the thinnest details and more specifically to capture the cell walls. Indeed, one of the apprehension before doing the experiment was to know if it was doable to scan a volume big enough to be characteristic of the structure while having a sufficient resolution to capture the thinnest walls. The results shown in **Figure 5-1** suggest that it is.

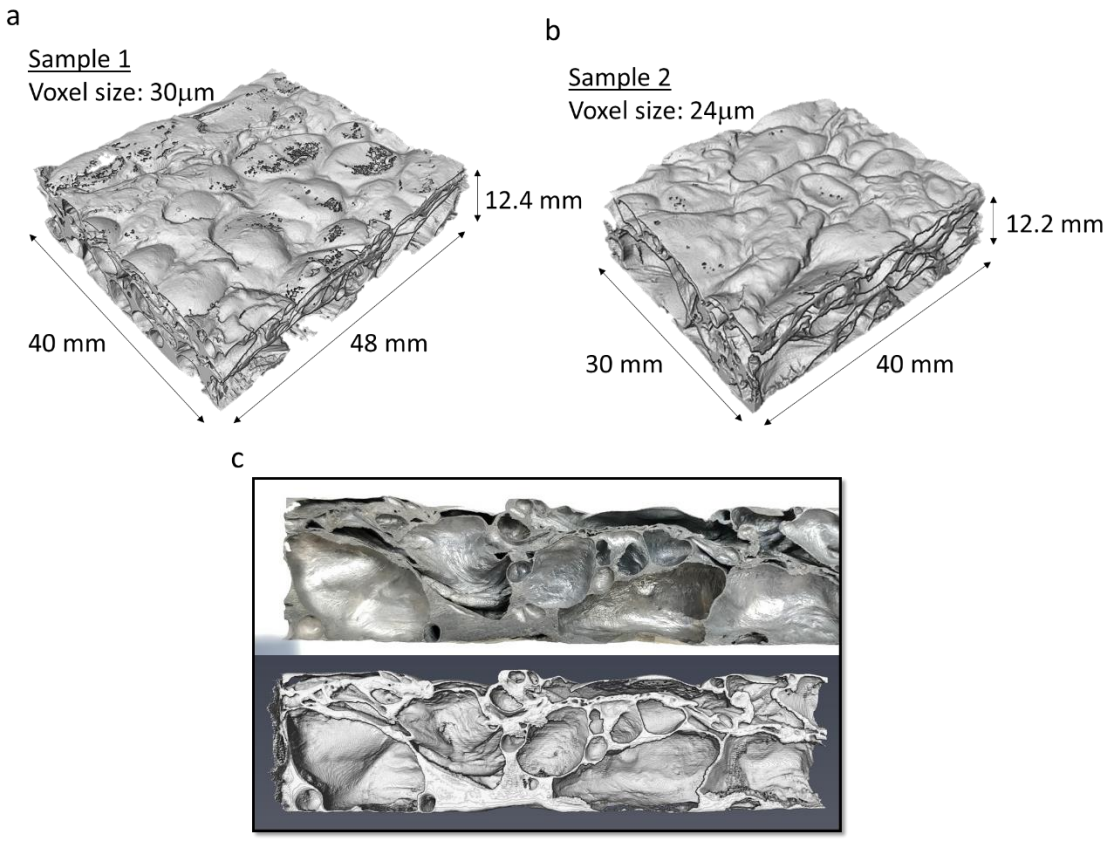

Figure 5-1. (a) Reconstruction of sample 1 (voxel size 30µm) (b) Reconstruction of sample 2 (voxel size 24mm) (c) and (d) Comparison of the same cross section obtained from a photograph (top) and x-ray tomography (bottom)

1.1.1. Relative density calculation

Table 5-1 summarizes the relative densities calculated by dividing the densities of the foams over the densities of their base materials, and the average relative density measured

from CT images. The relative density as calculated from the manufacturer data is 0.16. The calculated relative densities from the CT image analysis for sample 1 and 2 are 0.165 and 0.187 respectively. The relative density of sample 2 is probably overestimated due to the smaller dimensions of this sample. Indeed, a smaller sample means that it will be more affected by the image processing procedure and more specifically by discarding the unclosed cells on the edge of the sample. On the other hand, the relative density of sample 1 agrees well with the manufacturer value.

Table 5-1. Comparison of foam relative densities calculated from the manufacturer data and from the CT image analysis

Sample	Dimensions (mm)	Base material	Density (g/cm³)		Relative Density	
			Foam	Base material	Calculated	Image analysis
1	40x48x12.7	Al	0.44	2.75	0.160	0.165
2	30x40x12.7					0.187

The distribution of the relative density across the sample thickness was investigated and the results are shown in **Figure 5-2**. Both curves show a similar trend. The relative density increases sharply at the top and decreases sharply at the bottom of the foam. Indeed, the top and bottom of the foam are not flat and only a fraction of the foam is captured during the CT resulting therefore to small apparent relative densities. Besides those artifacts, the relative density reaches a minimum in the middle of the structure between 5 to 7mm. Finally, the relative density rises sharply at the bottom of the sample, which indicates a higher density at the bottom of the foam. Those observations are similar to other studies [132], [133] that revealed the same distribution of density. It is inherent to the melt gas injection

process. During solidification of the foam, the molten material drains through the cell membranes due to gravity leading to a gradient of thickness throughout the foam and a dense layer of aluminum at the bottom.

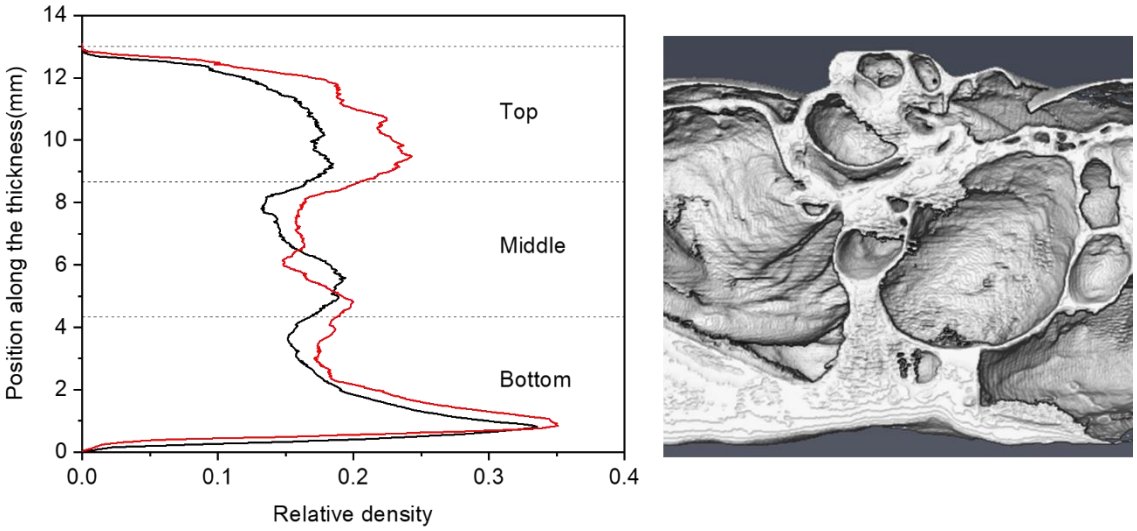

Figure 5-2. Evolution of relative density along the sample thickness

1.1.2. Pore size characterization

Figure 5-3 summarizes the results of the cell analysis. It displays the histograms of the equivalent diameter distribution of both samples. The two sets of data were not blended together because the dimensions of the samples were different and an effect of the sample size on the distribution could exist. Indeed, bigger cells are most likely to be detected in the bigger sample. The statistics were obtained from a population of 219 pores for sample 1 and 299 pores for sample 2. Cells below 0.5mm were not considered in the calculations due to the post processing procedure applied, which discards the smaller pores.

The equivalent diameter distribution ranges from 0.63 to 11.61mm and 0.45 to 9.82mm for sample 1 and 2 respectively. It indicates a wide distribution of cell size and therefore a non-uniform structure with the peaks clearly shifting towards the small diameters. The figure also indicates the contribution of each bin to the total porosity volume. Moreover, even though there is a majority of cells with small diameters, they contribute little to the total porosity volume. About 80% of the cells contribute only to about 12% of the total porosity volume.

Sample 1
Voxel size: 30mm

	Volume (mm^3)	Eq Diameter (mm)	Sphericity
Min	0.13	0.63	0.50
Max	820.24	11.61	0.98
Mean	46.07	2.95	0.82
Median	5.36	2.17	0.85
Standard deviation	103.06	2.29	0.11

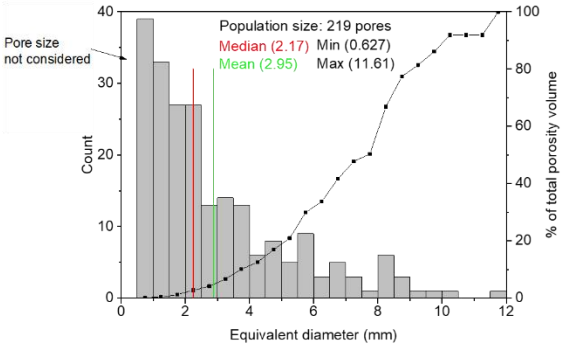

Sample 2
Voxel size: 24mm

	Volume (mm^3)	Eq Diameter (mm)	Sphericity
Min	0.05	0.45	0.40
Max	495.60	9.82	1.00
Mean	19.92	2.21	0.83
Median	2.30	1.64	0.86
Standard deviation	51.32	1.71	0.11

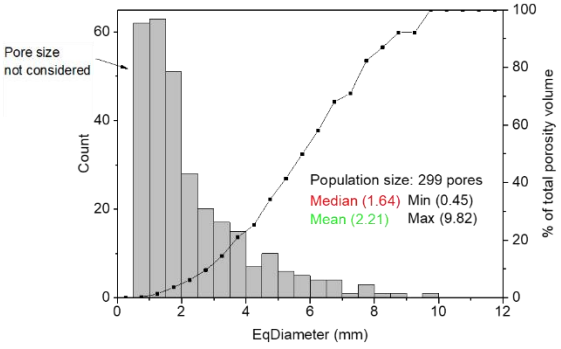

Figure 5-3. Summary of the results of the porosity analysis of the samples shown in figure 4-1. Cells below 0.5mm were not considered in the calculations due to the post processing procedure applied, which discards the smaller pores

The sphericity values are better understood when sorted as a function of the cell diameter. The cells below 3mm have a sphericity averaging at 0.86 (s=0.08) and the ones above 3mm averages at 0.73 (s=0.11). This discrepancy indicates that smaller cells tend to have a more spherical shape because their sphericity is closer to 1. Their shape is also more consistent as

the standard deviation is lower. Conversely, the sphericity of bigger pores is higher and more spread indicating a variety of non-spherical shapes.

Summary of the foam characterization by tomography

Tomography was used to characterize the morphology of the foam. The relative density, cell diameter and sphericity were used as indicators of the foam morphology and quantified. The relative density calculated from the experimental data was found to be close to the value calculated using the manufacturer data for the bigger sample scanned. The sample dimensions were shown to affect the relative density by overestimating it when the sample dimensions are reduced. However, the dimensions of the samples are limited to optimize the resolution of the tomographic scan.

A gradient of density through the thickness was unveiled. It proceeds from the drainage of the molten aluminum during processing of the foam due to gravity and could be prevented or at least reduced by optimizing the process.

The characterization of the cell diameters highlighted a non-homogenous distribution with a majority of cells having small diameters below 3mm. However those small cells accounts for less than 15% of the total volume of porosity. The larger cells accounts for the majority of the total porosity volume. The quantification of sphericity showed a higher sphericity of smaller cells (<3mm) compared to the bigger ones (>3mm). It is indicative of a non-uniformity in terms of cell shape when increasing the cell diameter, the smaller cells tending to be more spherical.

1.2. Characterization of the microstructure using X-Ray tomography

The capabilities of the tomograph allow operating it at a lower scale, thus characterizing the microstructure of individual cell walls. It is accomplished by switching to the nanofocus source, having an acceleration voltage of 160kV, and by decreasing the size of the sample so the distance between the source and the sample is reduced. Doing so, a resolution of 2µm was achieved on a small piece of a cell membrane and the results are shown in **Figure 5-4**.

A non-negligible presence of pores and cracks of various sizes was found inside the material. The carbides are hardly visible (light grey contrast) but easily distinguishable by their characteristic angular shape and distribution. However, the eutectic silicon particles are not detected. The characteristic size of the silicon particles is too small to be captured with the current resolution.

Even by optimizing the scanning conditions, the microstructure (eutectic silicon, carbides) is hardly visible. The silicon carbides might be more defined by increasing the resolution but eutectic silicon will most likely remain invisible. The tomography is therefore not the appropriate technique to characterize the microstructure features. However, the defects of the material are evident. The presence of pores and cracks indicates that the foam is highly flawed at a microstructure level, most likely due to processing. It is well known that when a material is subjected to a load, a stress concentration develops around the cavities [134], [135]. Therefore, the existence of such defects at the microstructural level in the cell membrane could indicate preferential sites for crack propagation and failure when

the foam deforms. In addition, it was explained in Chapter 1 (see section 3.4.4) how the presence of particles, such as the SiC particles found in this study, could modify the fracture behavior of the cells walls. The study by Onck et al. clearly demonstrated an embrittlement of the walls due to the presence of those particles. Therefore, the flaws revealed by the tomographic scans coupled to the presence of the SiC particles are significant to understand the deformation and the brittle fracture of the cell walls observed later during the compression tests. In an effort to optimize the properties of the foam, the processing should be improved to prevent the formation of such flaws.

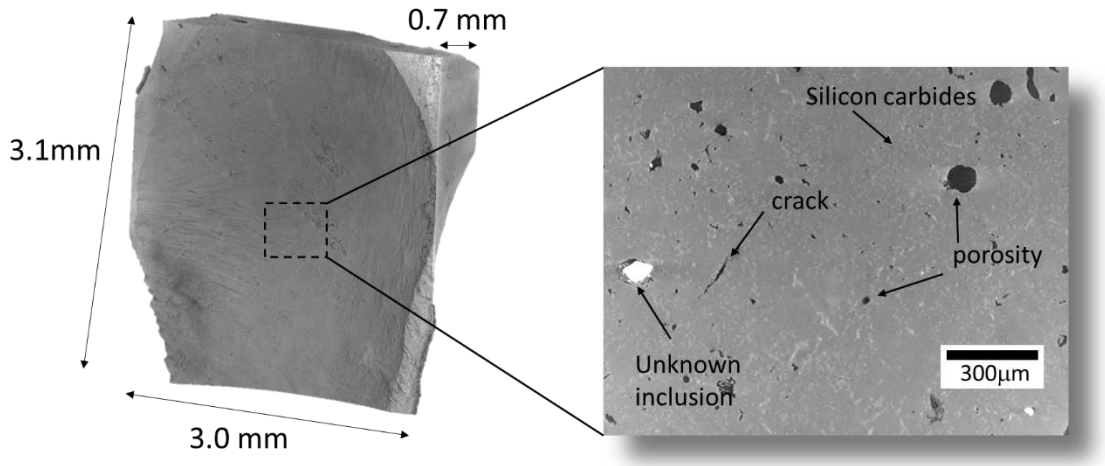

Figure 5-4. High-resolution scan of the piece aluminum foam (left) with a zoomed in view (right) revealing some microstructural features of the materials like porosity inside the walls, cracks and silicon carbides.

1.3. Characterization of the cell wall microstructures

Figure 5-6 shows the SEM images illustrating the microstructural features of the foam. It reveals the presence of α-Al dendrites and eutectic silicon phase. The dendritic phase is Al-rich and therefore ductile. The dendritic microstructure was characterized by the measure

of the secondary dendritic arm spacing (SDAS). It is measured by identifying and measuring an align group of dendrite cells. The SDAS is then calculated as SDAS = L/n, where L is the length of the line and n is the number of dendrite cells. **Figure 5-5** illustrates this procedure for a characteristic dendritic region. The SDAS is 20.9μm for the region shown in figure 1.

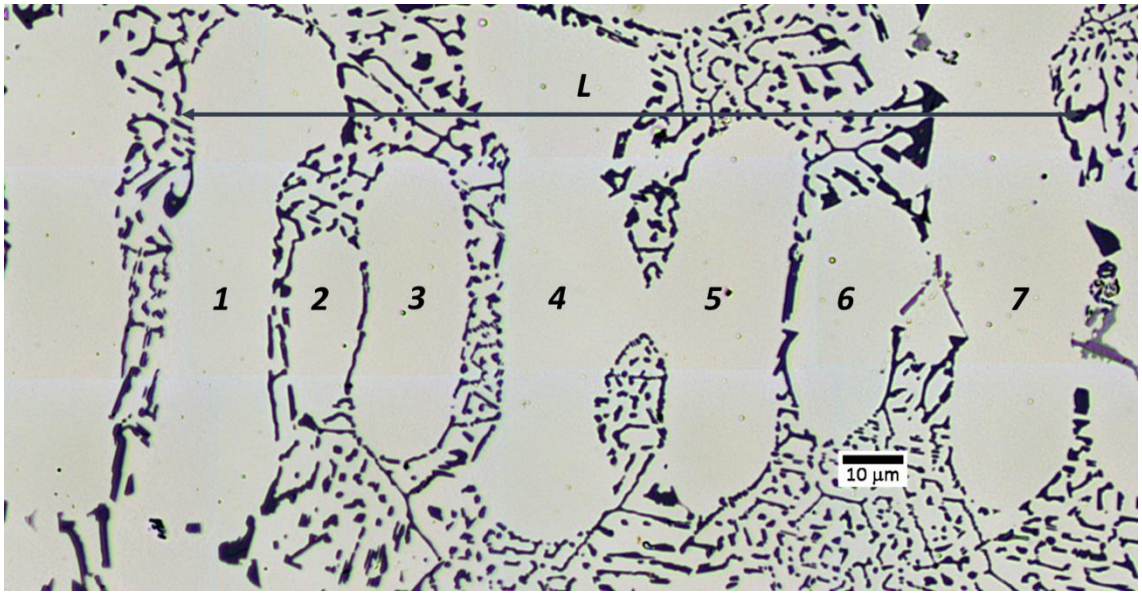

Figure 5-5. Optical image showing how to calculate the secondary dendritic arm spacing

A number of studies have investigated the effect of solidification variables on the microstructural features of alloys [58], [136], [137]. Specifically, using equation 1, the SDAS can be related to the solidification time when the solidification time is used as the solidification variable influencing the SDAS. Equation 1 was proposed by Bamberger et al. [137] for Al-Si alloys and define the SDAS as

$$SDAS = A_{Si}(t_S)^a\,, \qquad \textbf{Eq. 5-1}$$

where A_{Si} is a constant which varies inversely with the silicon content, t_S is the solidification time and a is an exponent which value can be found in the literature for a number of alloys.

It was experimentally observed for Al-Si alloys at various Si content that the SDAS is roughly proportional to the cube root of the local solidification time and that the constant A_{Si} is approximately 12. Thus, the solidification time t_S can be calculated by

$$t_S = \left(\frac{SDAS}{12}\right)^3. \qquad \textbf{Eq. 5-2}$$

For the region shown in **Figure 5-5**, the solidification time is approximately 5.3 seconds, which corresponds to a short time regarding the Al-Si phase diagram.

The eutectic phase is an alternation of ductile eutectic aluminum and brittle silicon platelets. The silicon platelets are elliptical with an aspect ratio averaging at 2.5. The diameter of the platelets ranges between 1.8 and 4μm. Their average spacing does not exceed 5μm. Silicon carbide particles were introduced during the manufacturing of the foam to improve its stability by increasing the viscosity of the melt. Their diameter averages at approximately 10μm.

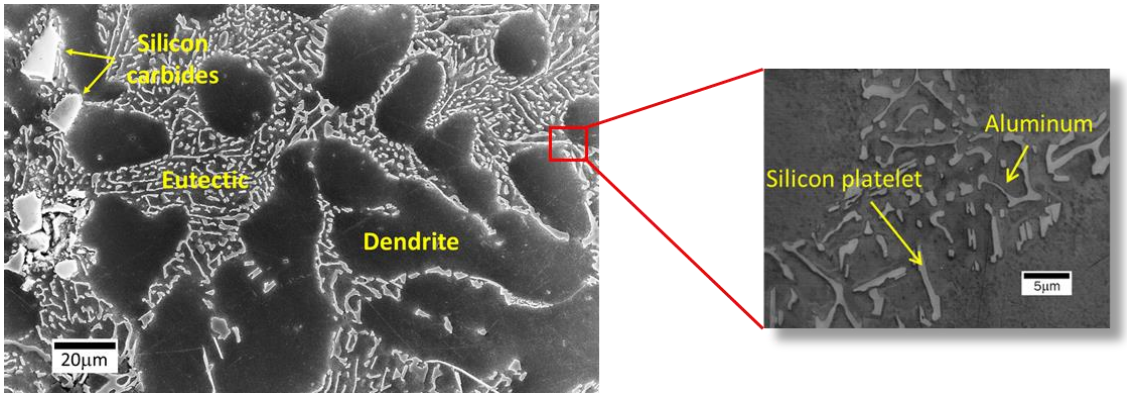

Figure 5-6. Microstructure of the foam showing the dendritic and eutectic phases and the silicon carbides particles (MEB-SEI)

The microstructure is also the results of a complex composition (see table 2-3 in chapter 2) reflected in the presence of Fe-rich and Mg-rich precipitates. The precipitates were observed and analyzed by energy dispersive spectroscopy (EDS) and the results are shown in **Figure 5-7**. The literature suggests that the Fe-rich intermetallic particles are detrimental for the mechanical properties [44]. However, it is usually very difficult and even impossible to remove all traces of iron in the alloy. The magnesium is mainly found in the microstructure as precipitates as seen in **Figure 5-7** and in appendix A (**Figure A-1e**). Appendix A gives a closer look at the distribution of Mg inside the Al solid solution and suggests that magnesium is not uniformly distributed in the solid solution but is concentrated in and around the Mg precipitates indicating that Mg migrates during solidification to form Mg-rich precipitates and intermetallic with other elements. The role of Mg on the mechanical properties is therefore most likely limited to those areas and does not play a major role in the properties of the Al phase.

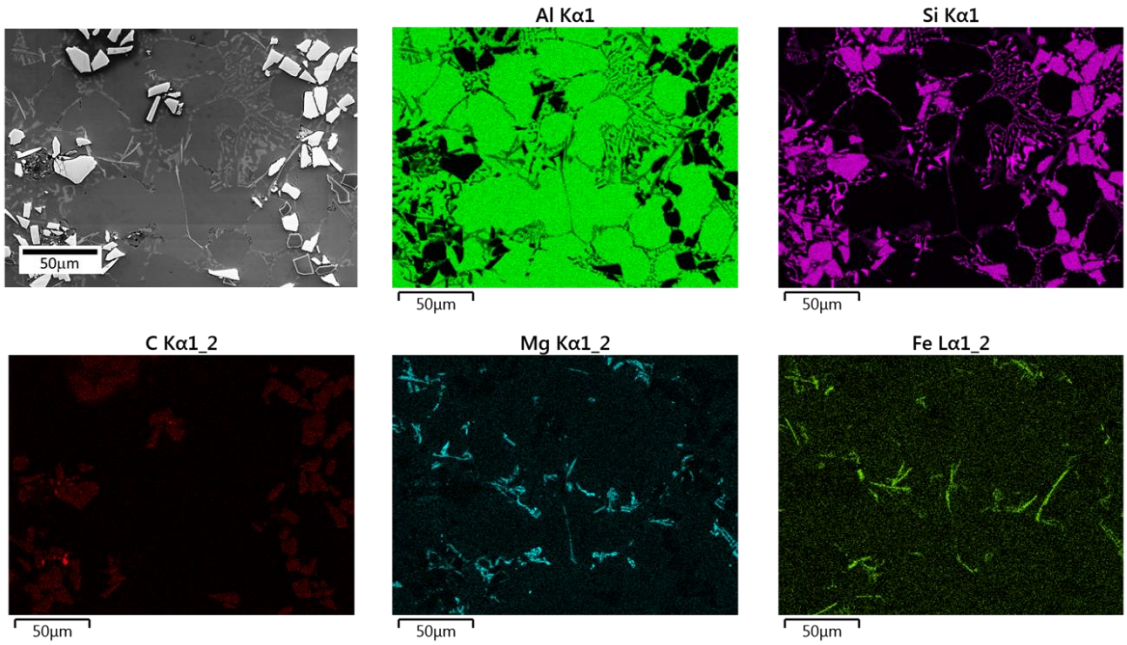

Figure 5-7. Qualitative EDS maps revealing the presence of Fe-rich and Mg-rich precipitates

The microstructural features are highly dependent on the cooling rates during solidification. The size of the dendrites and the shape of the silicon particles, from acicular to fibrous, are modified upon different solidification conditions [61], [63], [68], [75]. The melt gas injection process used to manufacture the foam induces different cooling conditions from one part of the foam to another. It is due to the complexity of the process and the difficulty to control homogeneously the injection of the gas inside the aluminum melt. It results in a highly inhomogeneous microstructure.

Figure 5-8a and **b** are two images having the same scale and highlighting the difference in terms of dendrite size from two different regions. **Figure 5-8a** shows a very fine dendritic structure while **Figure 5-8b** reveals a dendritic structure four to five times larger.

Figure 5-8c and **d** highlight the different morphologies of silicon particles found inside the cell walls. **Figure 5-8c** shows elongated, acicular particles while **Figure 5-8d** reveals a very fine and fibrous eutectic microstructure.

Finally, **Figure 5-8e** and **f** attest of the inhomogeneity of the silicon carbide particles distribution. Indeed, **Figure 5-8e** shows a cell wall with a very high density of particles while **Figure 5-8f** shows another wall with no particles at all. It also reveals that the particle are distributed in the eutectic phase which is in agreement with the literature focused on metal matrix composites of casting alloys (see chapter 1). During the dendritic growth, the particles are pushed by the solidification front and are trapped in the eutectic structure after complete solidification.

The microstructure is highly inhomogeneous inside the cell walls. One wall can be full of carbides while another can have none. The shape and distribution of the eutectic silicon differ greatly as well. All those considerations put together draw the picture of an inhomogeneous microstructure.

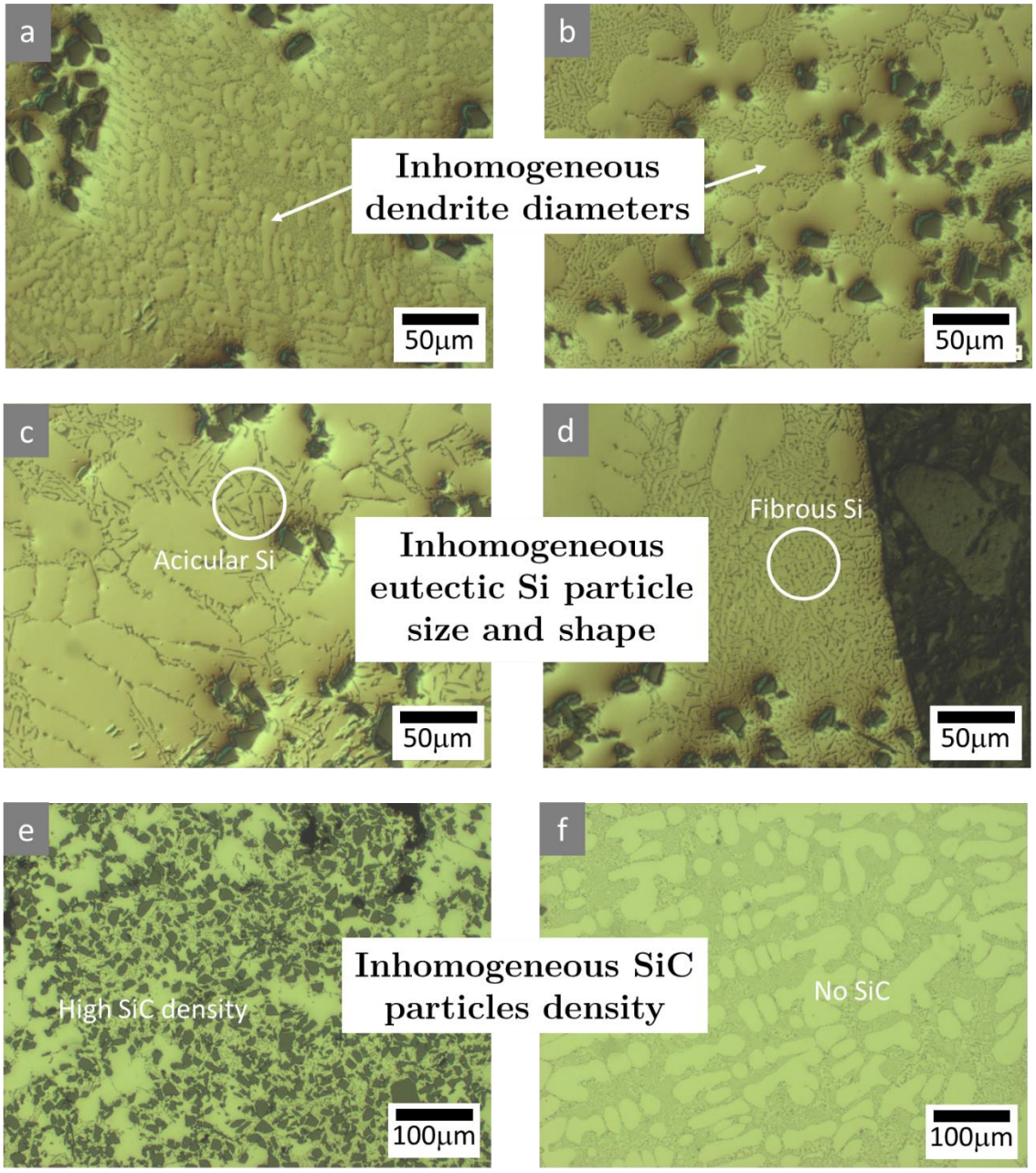

Figure 5-8. Optical microsocpies of a cell wall showing (a) and (b) Two regions having different dendrite sizes. (c) and (d) Two regions with various eutectic silicon shapes and sizes. (e) and (f) Two regions having different SiC partilce distributions: (e) has a very high SiC density while (f) has no carbides.

1.4. Nanoscale characterization of the microstructure by TEM

Al-Mg-Si alloys belong to the age-hardening alloys category, which possess superior mechanical properties because of the interaction between the dislocations and the precipitates produced during an annealing treatment. Even though no heat treatment was applied during the manufacture of the foam, a TEM investigation was performed to characterize the presence of precipitates in order to better understand the mechanical behavior of the foam.

1.4.1. Preparation of the thin foil

The different steps for preparing the foil are illustrated in **Figure 5-9**. As shown in **Figure 5-9a**, the foil was extracted between two rows of indents across a secondary arm of a dendrite. The circles, observed in both **Figure 5-9a** and **b** result from the EDS spot scans carried out before the extraction of the foil.

First, a layer of platinum is deposited to protect the surface from sputtering (**Figure 5-9a**). Then, trenches are milled at high current to isolate the foil from the rest of the material (**Figure 5-9b**). The foil is then extracted using a micromanipulator (**Figure 5-9c**). Finally, the foil is attached to a TEM grid and thinned down to be transparent for electrons (**Figure 5-9d**). At this stage, very low currents (9nA and 3nA) are used to preserve the integrity of the foil. The TEM grid is made of high purity beryllium, which facilitates the chemical analysis. Indeed, the low atomic number of beryllium (Z=4) assures that EDS spectra are free of non-desirable peaks and have low background noise.

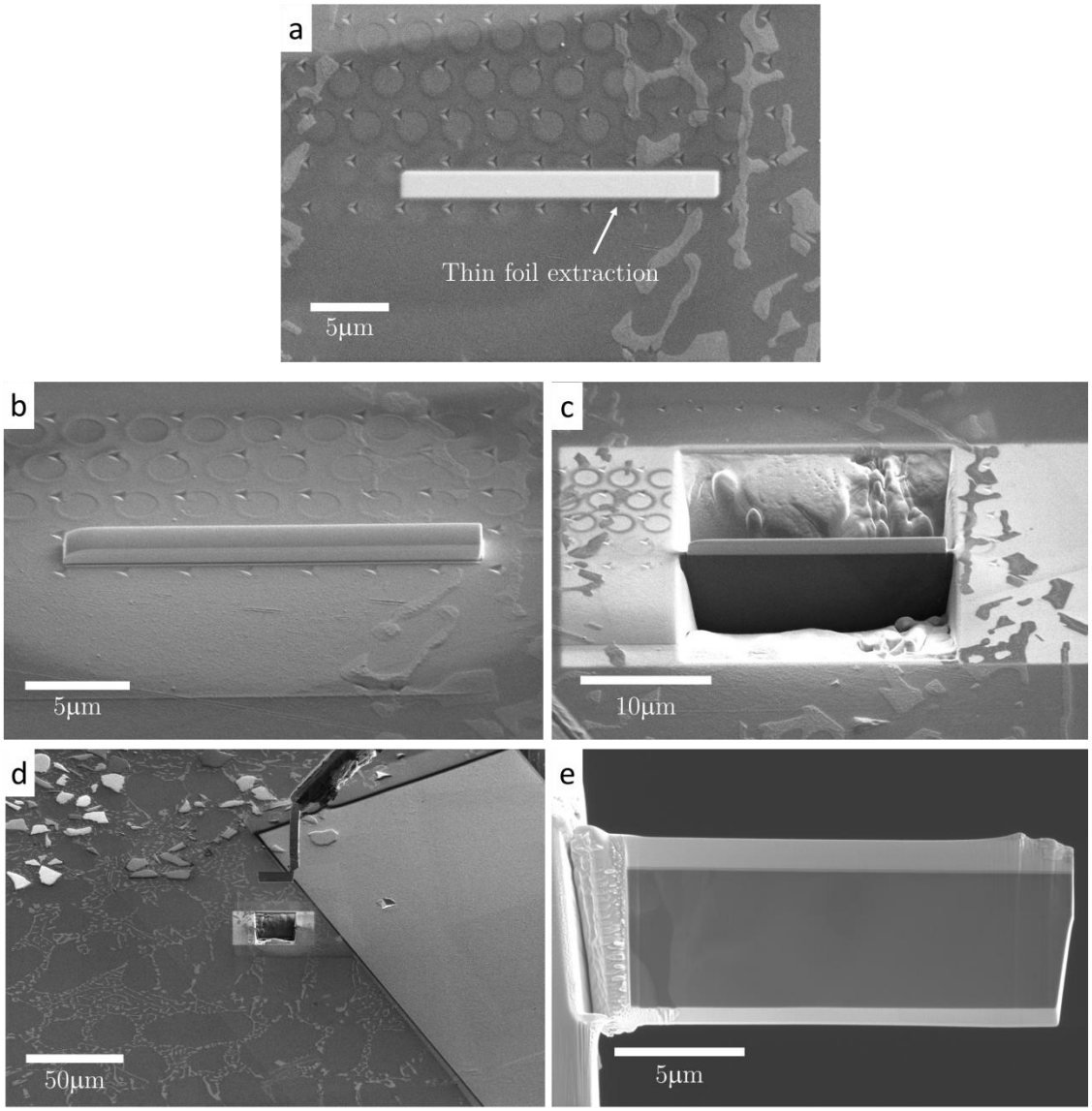

Figure 5-9. Procedure of the FIB lift-out technique used to prepare thin foils for TEM imaging. (a) The thin foil is extracted between two lines of indents inside a 5x15 array. (b) A layer a platinum is deposited to protect the surface from sputtering. (c) The thin foil is prepared by milling trenches. (d) The thin foil is extracted using a micromanipulator. (e) The foil is attached to a high purity beryllium grid and thinned down to be transparent to electrons.

The TEM was used to image the microstructure of a cell wall at the nanoscale scale. Both the precipitates and dislocations are characterized. Moreover, EDS analysis was performed in the dendritic phase to identify the composition of the precipitates.

1.4.2. TEM characterization of the microstructure

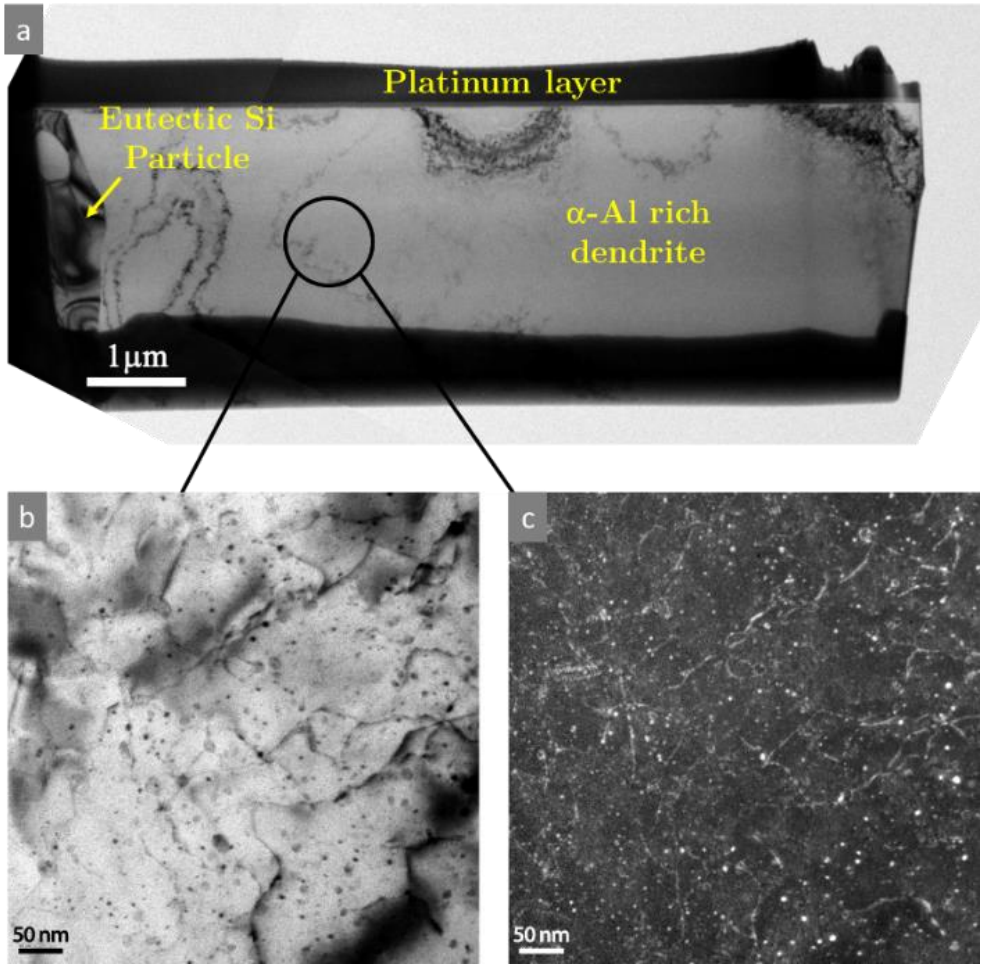

Figure 5-10. (a) TEM image of the thin foil. A eutectic Si particle is visible on the left of the image. (b) and (c) Bright and dark field, respectively, TEM images of the same microstructure in the dendrite taken in the circled area of (a). The red arrows in (b) highlight the presence of dislocation loops.

A TEM image of the thin foil prepared by FIB (see Chapter 2) is shown in **Figure 5-10a**. A eutectic Si particle is visible on the left hand side of the image while the rest of the foil corresponds to the dendritic phase. **Figure 5-10b** and c are respectively bright and dark field TEM images of the same region taken in the circled area in **Figure 5-10a**. The diffraction conditions set for bright-field contrast (**Figure 5-10b**) highlight more clearly the

presence of precipitates while those used for dark-field imaging (**Figure 5-10c**) accentuate the dislocations microstructure. It reveals a microstructure made of a non-uniform array of dislocations and dispersed precipitates.

Figure 5-11 shows a region of the foil taken in STEM using Annular Dark Field (ADF) and High Angle Annular Dark Field (HAADF) contrasts. The ADF-STEM imaging provides less stability because issues related to the specimen drift arise. However, the current density in STEM mode is higher than regular TEM mode which produces higher signal to noise ratio and therefore better pictures compared to DF-TEM (especially for thick sample). Three categories of precipitates can be distinguished depicted in **Figure 5-11c**, **d** and **e**. **Figure 5-11c** details the first category corresponding to the bigger precipitates which diameter ranges around 20nm. They are spherical and some of them emerge in a different (light-grey) contrast in the HAADF image shown in **Figure 5-11b**. The difference of contrast in HAADF scales with the atomic number (scaling law of contrast $\approx Z^{1.7}$) and the sample thickness. Accordingly, the brighter contrast suggests heavier elements in these precipitates. However, not all bigger precipitates appear in the HAADF image indicating presumably different compositions from one precipitate to another. The second category is depicted in **Figure 5-11d** which shows smaller spherical precipitates with diameters below 10nm. They are randomly distributed in the microstructure and more numerous than the bigger precipitates. Finally, the third category corresponds to what is illustrated in **Figure 5-11e** showing a fringed contrast. The origin of those features is not well understood. However, the literature reports the same findings in irradiated materials [138]–[140]. The fringed contrast

can be the consequence of the nucleation of multiple interstitial and/or vacancy loops. The formation of loops is caused by the presence of vacancies and interstitial defects introduced by irradiation and/or subsequent annealing treatments which favor the growth of those loops [138], [139]. The exact formation mechanisms remain hazy and the reader is directed to the indicated references for more details. In our case, the loops could be a consequence of the bombardment of Ga^+ ions during the preparation of the foil by FIB, similarly to what shown by Lv et al. during electron irradiation of Si wafers [140].

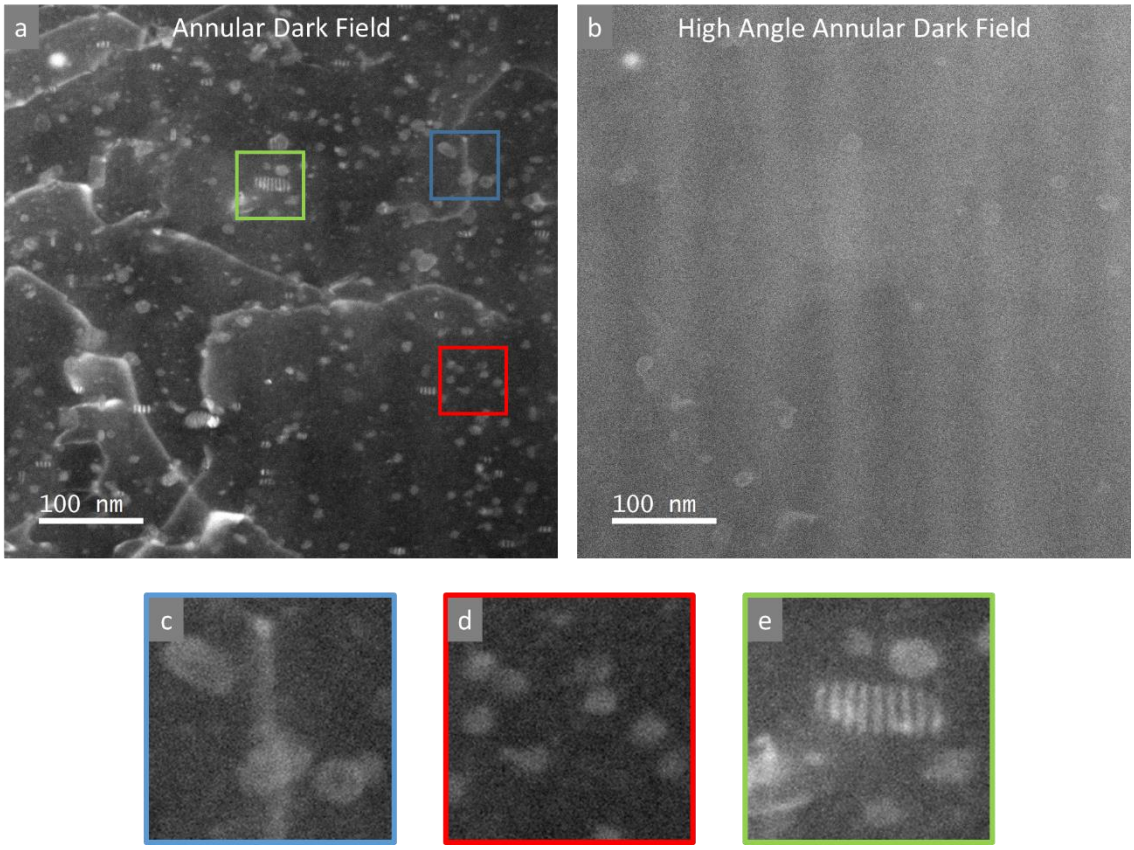

Figure 5-11. STEM images of the microstructure of the dendritic phase (a) Annular dark field image (b) Corresponding high angle annular dark field image (HAADF) (c), (d) and (e) Enlarged images of the regions indicated in (a) highlighting the various types of precipitates found.

The microstructure of this eutectic silicon was also imaged and the results are shown in **Figure 5-12**. The particle was reconstructed from several images but an enlarged image of the Si particle is shown. It reveals very fine precipitates inside the silicon particles ranging between 3 and 10nm. The precipitates are homogeneous in terms of spatial distribution inside the Si particles and shape.

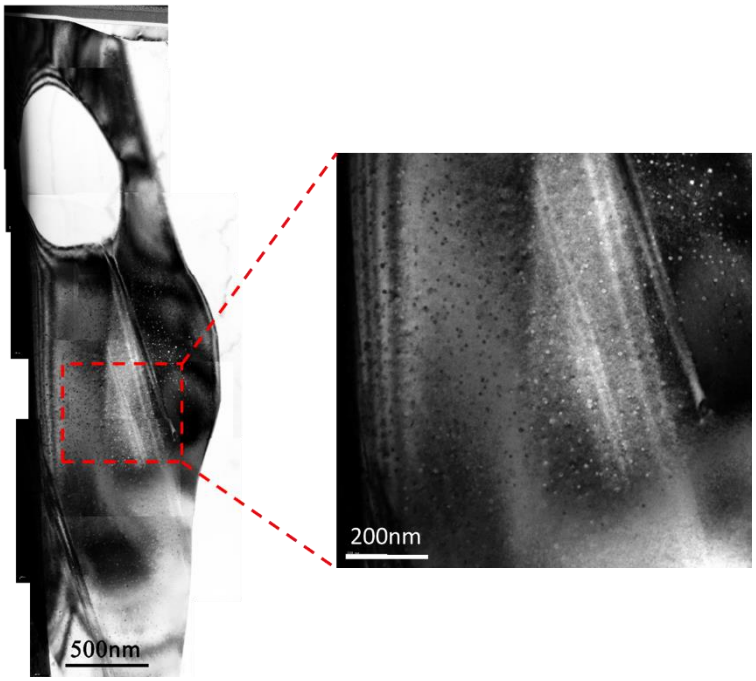

Figure 5-12. Microstructure of a eutectic silicon particle as imaged by transmission electron microscopy. Fine precipitates inside the particles can be observed.

1.4.3. TEM chemical analysis

The chemical composition of the dendritic phase was determined using the EDS detector implemented in the TEM. An attempt to determine the composition of the precipitates and the matrix was made.

Figure 5-13 was acquired in the Al matrix while **Figure 5-14** was acquired on a "big precipitate". What is referred as "big precipitate" is illustrated in **Figure 5-11c**. The same acquisition conditions (dwell time, beam current) were used for all spectra. Four elements were identified in both spectra: Oxygen, Gallium, Aluminum and Silicon. Oxygen is inherent to the surface contamination of the sample and is not accounted for in the conclusions. The Gallium peaks correspond to the pollution from the Gallium source of the FIB used to prepare the thin foil. Two Gallium peaks are discernible at around 1.10 and 9.21 keV corresponding to the Lα and Kα emission lines respectively. The peaks are higher in **Figure 5-14** than they are in **Figure 5-13** indicating a preferential migration of the Ga^+ ions onto the precipitates. The Al peak is higher in the matrix at around 4500 counts (**Figure 5-13**) than it is in the precipitates at around 4100 counts (**Figure 5-14**). The opposite observation can be made for the Si peak, which is higher on the spectra acquired on a precipitate (**Figure 5-14**).

Because the Si peak is consistently higher when EDS is performed on a precipitate, and because no other elements were found, it is highly suspected that the precipitates are Si-rich. However, it is not possible to obtain their exact composition. In addition, it is interesting to notice the absence of magnesium. Indeed, from chapter one, one could have expect to detect magnesium in the form of Mg_2Si precipitates as it is common to observe in Al-Si-Mg alloys. However, the absence of Mg at this scale suggests that the magnesium preferentially precipitates in the form of intermetallic compounds as shown in **Figure 5-7**.

This is consistent with the observation made in the section 1.3 of this chapter from the EDS results performed in appendix A.

The JEM-2200FS microscope used in this work is equipped with an EELS detector, which could potentially give information about the exact composition of the different phases. However, the thickness of the foil (>150nm) prevented any analysis with the EELS detector.

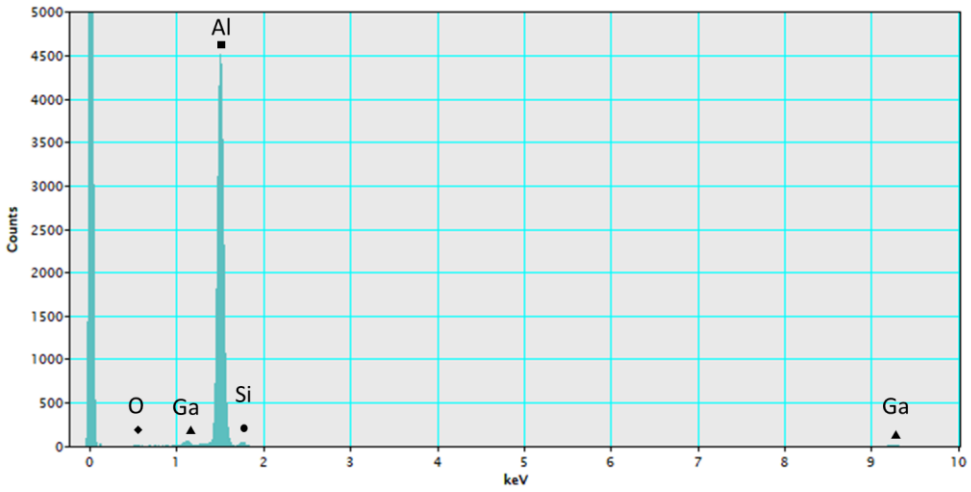

Figure 5-13. STEM-EDS spectrum in the matrix of the dendritic phase.

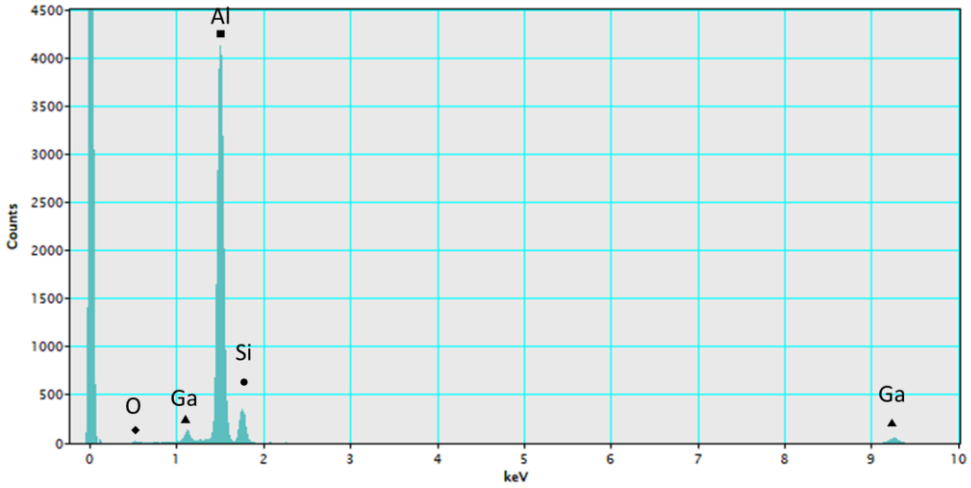

Figure 5-14. STEM-EDS spectrum in the dendritic phase on a "big precipitate" of the dendritic phase

The TEM characterization unveiled dispersed precipitates and dislocations. Precipitates and defects were identified at the nanoscale. The precipitates can be categorized depending on their shape and size. The bigger precipitates (≈20nm) are less numerous than the smallest one and not as well distributed inside the microstructure. Their shape is not perfectly circular and some showed a more elongated shape. The smaller precipitates are circular and homogeneously distributed in the microstructure. Their diameters vary but are less than 10nm. Defects were also exposed through the observations of "fringed features" characteristic of the nucleation of dislocation loops from clusters of vacancies or atoms. The impact of ion milling was suggested to explain their presence.

Summary of the multiscale characterization of the foam

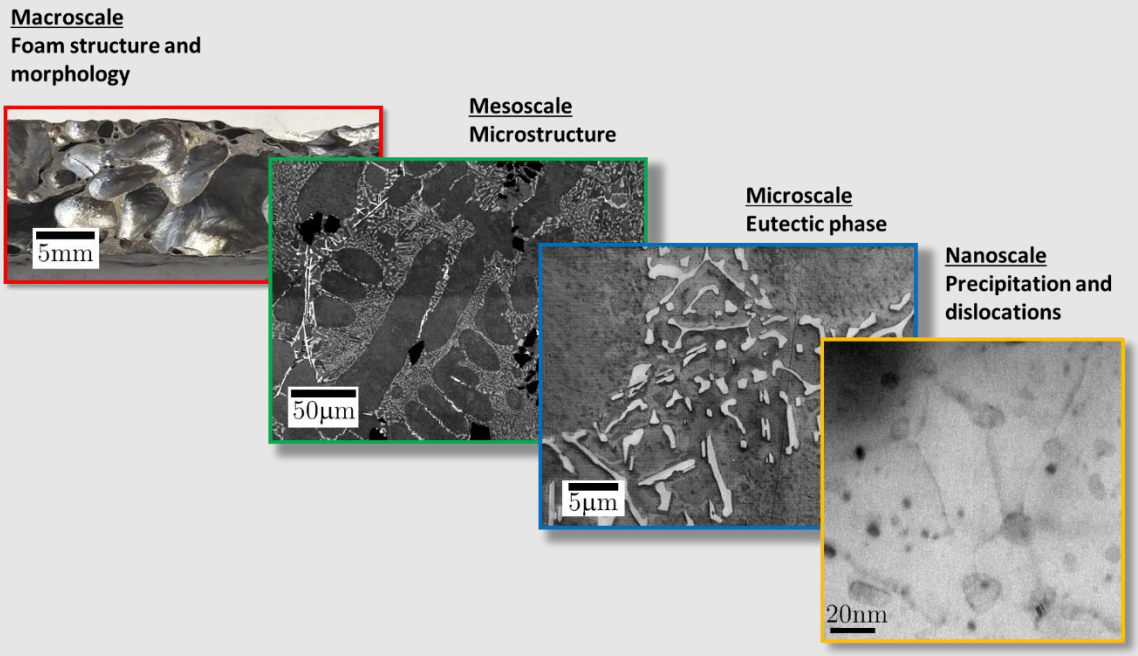

The foam was characterized at different levels coupling tomography and microscopy techniques. The material exhibit a highly inhomogeneous structure at all scales. The foam

morphology and density were characterized using X-ray tomography and a gradient of density was exposed throughout the foam thickness resulting from the manufacturing process favoring the liquid to flow to the base of the structure.

Then, the microstructure of the cell walls was investigated using optical and electronic microscopies. As predicted by the Al-Si phase diagram, the microstructure exhibits a dendritic α-Al phase and a eutectic phase made of silicon platelets. Silicon carbide particles, added to the melt during the manufacture of the foam, were characterized. The microstructure of the walls is deeply inhomogeneous. The size of the dendrites, the shape of the Si platelets as well as the density of the SiC particles were showed to vary greatly from one region to another.

Finally, TEM was used to investigate the nanoscale features of the microstructure with a focus on the dendritic phase. Precipitates and defects were spotted. Bigger, more elongated precipitates were shown as opposed to spherical smaller ones. In addition, defects were also exposed through the observations of "fringed features" characteristic of the nucleation of dislocation loops from clusters of vacancies and/or atoms. The impact of ion milling in the FIB was suggested as a hypothesis to explain their presence. The composition of the precipitates was determined by TEM-EDS. The results suggest a high Si content but the exact composition could not be determined. The smaller precipitates were not identified because they were too small. The TEM investigation revealed several precipitates of various sizes, which could contribute to various interaction behaviors with the dislocation.

2. Characterization of the mechanical properties of the foam

This section is focused on the characterization of the mechanical properties of the foam in the light of the structural and microstructural characterization presented in the previous section. The importance of considering the foam as a multiscale material possessing various interfaces was demonstrated. Therefore, the characterization of the mechanical properties must reflect its complex nature by way of different techniques. In addition, the inhomogeneities illustrated at different scales will most likely convey in the mechanical response and correlating the two is the objective of this work. To achieve that, the tomography will first be used to understand the mechanisms of deformation of the foam in compression at the cell level. Then, the cartography by nanoindentation is used to measure the mechanical properties (i.e. hardness here) of the dendritic phase. The hardness distribution is then coupled to chemical analysis of the indented area to correlate the composition and the local mechanical properties. Finally, the study of the nanoindentation curve will be used to characterize the mechanical properties at the nanoscale and more specifically the dislocation/precipitate interaction.

By constantly associating the structural and microstructural observation to the mechanical behaviors observed at different scales, a complete overview and understanding of the deformation of the foam will be available.

2.1. Macroscale characterization of mechanical properties

2.1.1. Uniaxial compression

The sample dimensions were chosen to prevent exceeding the load cell limits while maintaining the highest ratio of the specimen size to the cell size as it can affect the measured mechanical properties [83], [99]. A ratio superior to 7 is recommended and was achieved (considering a maximal cell size of ≈10mm from **Figure 5-3**). The final dimensions of the tested samples were 76x76x13mm. The speed of the cross head is v=0.1mm/min corresponding to a strain rate of $\varepsilon=7.7\text{x}10^{-3}$.

The results of the characterization of the uniaxial compression properties of the foam are summarized in **Figure 5-15**. We first notice the scattering of the curves originating from different relative densities from one sample to another as indicated on the figure by the black arrow. Indeed, and despite that all samples had the same dimensions, they were extracted from panels presenting local inhomogeneity in terms of relative density. We can identify two effects of the relative density on the stress strain curves in compression. Firstly, an increase of relative density extend the linear elastic region therefore increasing the value of the plateau stress. Secondly, it reduces the densification strain, above which the densification takes place. These observations are consistent with previous results and more specifically with the early models proposed by Gibson and Ashby [82], [83] describing the correlation between the relative density and mechanical properties of foams.

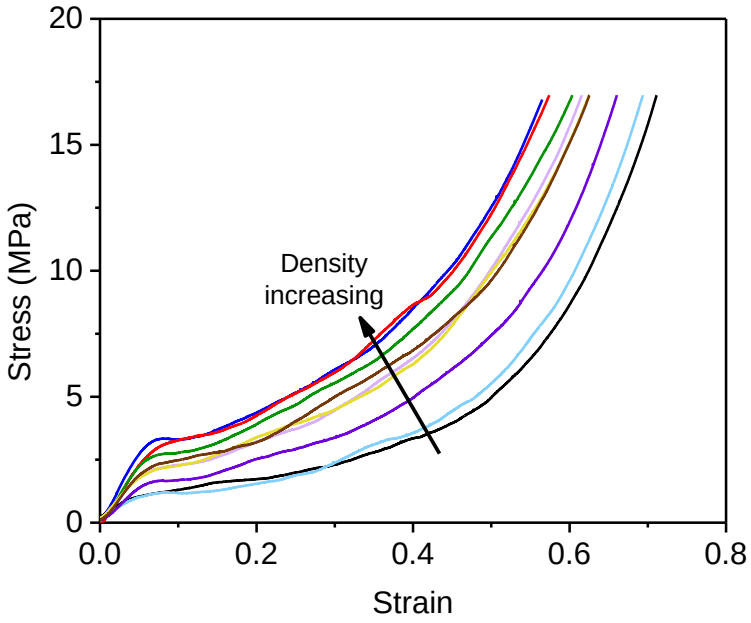

Figure 5-15. Compressive stress–strain response of the foam. All curves were obtained from samples having the same dimensions. The scattering comes from the difference in density from one sample to another.

Besides the scattering, all curves show a similar behavior following the characteristic deformation behavior of foams. It comprises an initial linear regime followed by a plateau region up to the densification. At the first stages of deformation, the stress increases quasi linearly and is commonly mistaken as an elastic regime. In reality, local, non-reversible, plastic events take place in the form of bending of the cell walls and faces. It is followed by what is called the plateau regime, which gives the foam its mechanical energy absorption properties. The stress varies little with the increasing strain resulting in a quasi-zero slope of the curve. Here the plateau is not flat and corresponds more to a rising plateau where the stress increases with the strain but the slope remains low compared to the linear and densification regime. The cells collapse by buckling, yielding or cracking of the cell walls and faces. Finally, the densification corresponds to a sharp increase of the slope of the curve and

the stress increases steeply. The cell walls and faces crush together and are pushed against each other.

2.1.2. In-situ compression with X-ray tomography

The deformation mechanisms of the foam were investigated using in-situ X-ray tomography. A compression apparatus with a load cell capacity of 25kN was mounted on the tomograph shown in chapter 2 and scans were recorded at different levels of strain to follow the deformation of the cellular structure. The dimensions of the samples are a compromise between maintaining a good resolution, not exceeding the capacity of the load cell and having closed porosity inside the sample. Two samples of 2x2cm were compressed using a crosshead speed of 0.9mm/min corresponding to a strain rate of ε=7.0x10^{-2}. In comparison, the uniaxial compression results shown in the previous section were obtained with a strain rate ε=7.7x10^{-3}. However, both the uniaxial compression and in-situ uniaxial compression are considered quasistatic and no effect from the strain rate is expected on the deformation behavior. The tomographic parameters were the same for both samples resulting in a resolution of 18μm.

The stress strain curve of both samples is shown **Figure 5-16**. The vertical dashed lines on the plot represent the strains at which the different tomographic scans were made. Sample 1 was scanned at 0.03, 0.12, 0.24 and 0.35. Sample 2 was scanned at 0.08, 0.21, 0.30 and 0.43. The grey dotted line represents the average of the curves represented in **Figure 5-15**.

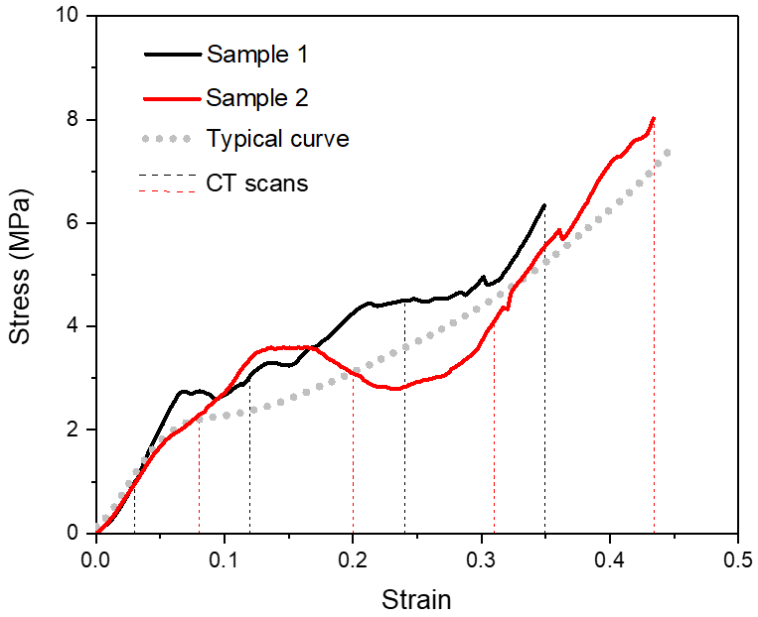

Figure 5-16. Compression stress-strain curves of the two samples tested for in situ X-ray tomography. The vertical dotted lines indicate the strains at which the CT scans were recorded. The grey dotted line is the average of the curves represented in **Figure 5-15**.

The compression curves fit well with the averaged curve, implying that despite the small dimensions of the specimens, the deformation behavior is representative of the macroscopic behavior illustrated in **Figure 5-15**. There are no clear delimitations between the different stages of the deformation unlike what we would expect from a metallic foam (linear elasticity, plateau region and densification). Both curves show a similar linear elastic part until ε=0.04. After that, the curves dissociate and their slope changes which indicate the onset of local plasticity and failure of the structure. The densification, beyond which the structure compacts and the stress rises steeply, starts around ε=0.32 for sample 1 and ε=0.30 for sample 2. The differences between the two stress strain curves are expected because the sample dimensions are too small to ensure the reproducibility of the deformation. However,

it does not detract from the validity of the observations and the conclusions made later on the deformation of the cellular structure.

The densification occurring during the deformation is illustrated on **Figure 5-17** which is a plot of the evolution of the relative density as a function of the applied strain. The relative density was calculated as the average of the individual relative densities of the slices. An increase of 45% and 50% is observed for sample 1 and 2 respectively. The errors bars are high and reflect the inhomogeneous density of the foam unveiled earlier in **Figure 5-2**.

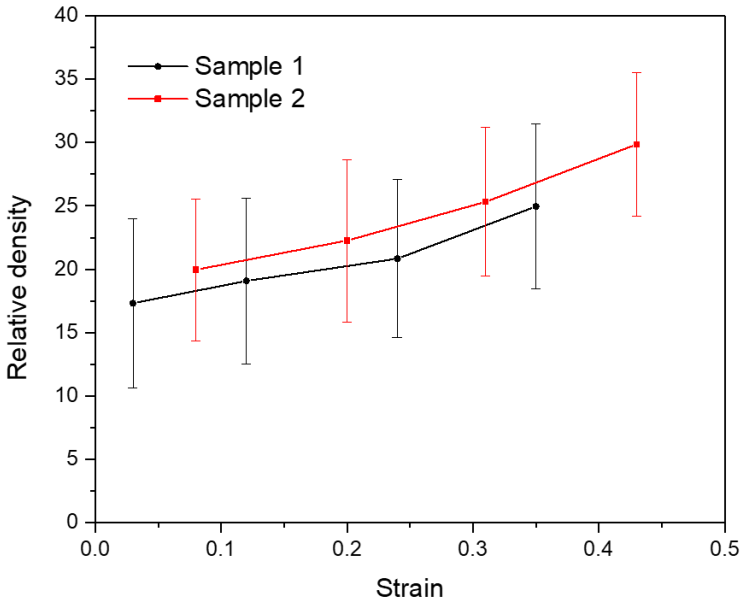

Figure 5-17. Evolution of the relative density as a function of strain for the two sample tested.

The evolution of the relative density along the sample thickness as function of strain was also investigated by repeating the procedure of **Figure 5-2** for the CT scans performed at different strains. The results for sample 1 and 2 are shown on **Figure 5-18a** and **b** respectively. Those plots give information about the failure process of the structure in terms

of where the deformation occurs in the material. It also gives an idea of when the densification takes place.

The deformation is sequential rather than homogeneous. **Figure 5-18a** reveals that the deformation of sample 1 initiates in the middle of the structure (≈5.5mm) where the density is the lowest. It is indicated by the dissociation of the ε=0.03 and ε=0.12 curves. As the stress increases, the top half of the curves progressively shifts down while the bottom half of the foam remains unchanged. It illustrates that the densification is localized in the top half of the foam and propagates towards the highest density regions situated at the bottom of the foam.

It is further illustrated in **Figure 5-18b** displaying the results of sample 2. A very high peak of density is observed on the curves resulting from an irregularity in the structure of the foam but observations analogous to sample 1 can be made. The first deformation events once again initiates at around 5.5mm where the density is the lowest. As the strain increases, the top half shifts towards the bottom and the density peak broaden. The density in the bottom 4mm increases as the strain increases indicating densification in this region.

The deformation of the foam is therefore progressive and a direct aftereffect of the gradient of density unveiled in **Figure 5-2**. The densification initiates in the lowest density region localized in the middle of the foam. Then, it propagates towards the higher density regions. The bottom of the foam, associated with the highest density values, is not affected

until consequent deformation levels are reached. The observations are similar to other studies performed on foam manufactured using the same process [132], [133].

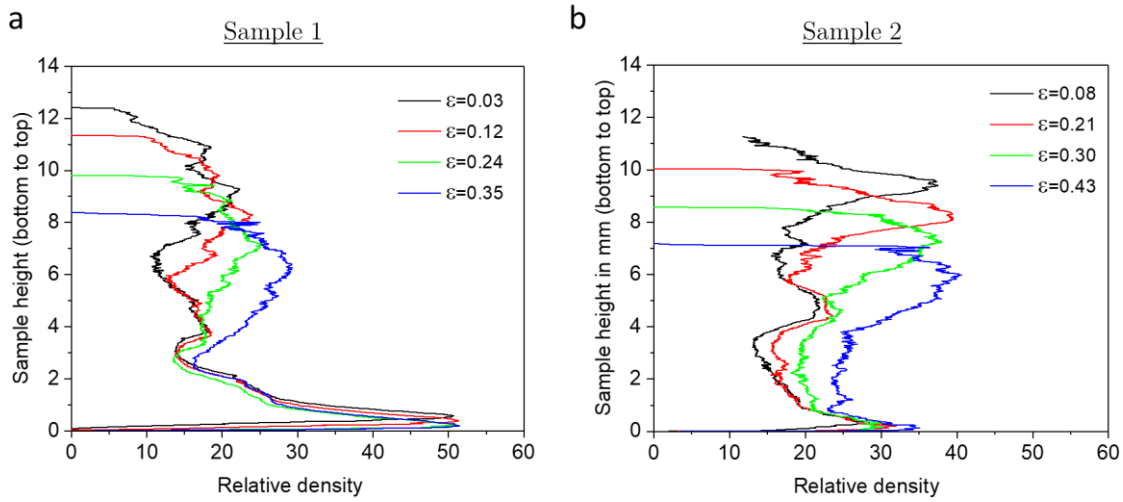

Figure 5-18. Evolution of the relative density along the sample height for different strain increments of sample 1 (left) and sample 2 (right)

Figure 5-19 illustrates a cross section of sample 1 parallel to the loading direction at different strain levels. The foam has a complex and inhomogeneous deformation behavior, which is the result of local deformation of the cell walls. The black dashed lines are placed at 5.5mm from the bottom of the foam, which corresponds to the location of the onset of densification as observed in **Figure 5-18a**. The deformation is clearly localized in the upper half of the foam. In **Figure 5-19b**, no modification of the bottom half is observed while many plastic events occurred in the upper half. The first sign of plastic deformation in the bottom half only appear in **Figure 5-19c** and proceed in **Figure 5-19d**.

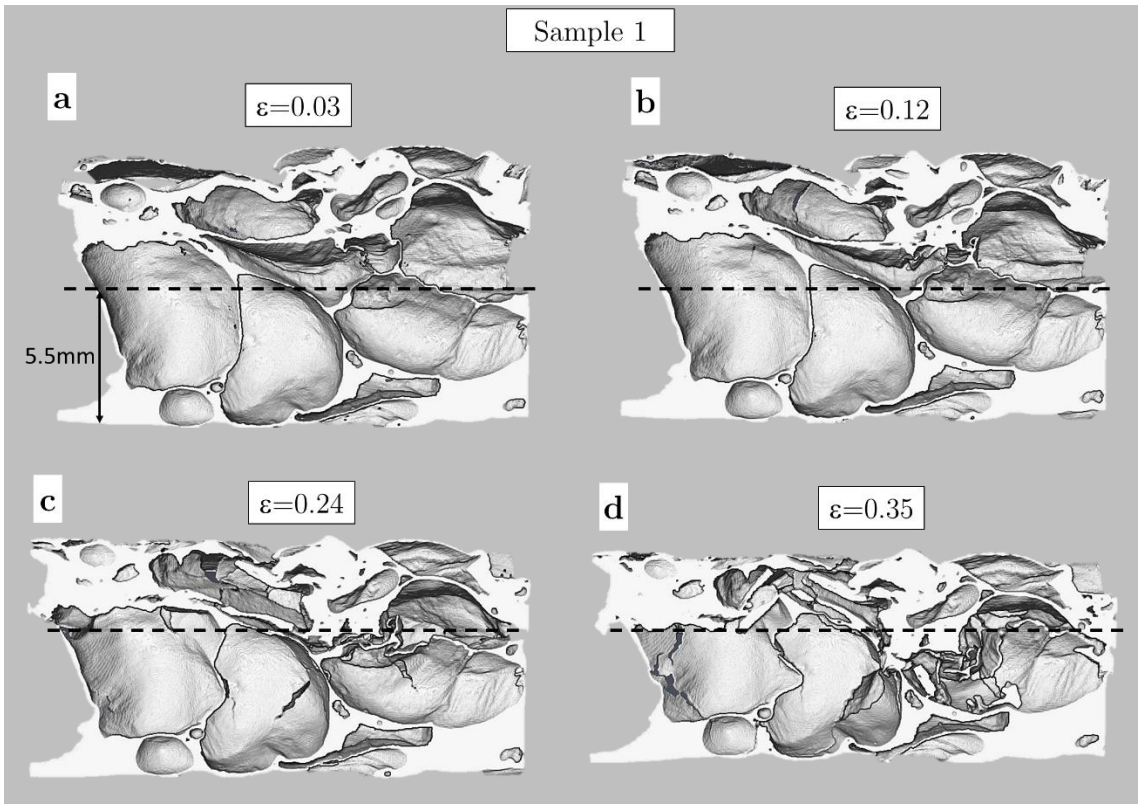

Figure 5-19. Evolution of the cellular structure at different applied strain (sample 1). The black dashed lines are placed at 5.5mm relative to the bottom of the foam corresponding to the onset of deformation determined in **Figure 5-18**.

The deformation mechanisms associated with the compression of the foam are numerous as illustrated in **Figure 5-20**. The weak cells collapse first by bending or buckling of the cell walls. As already defined in the literature, the weak cells are the elongated ones which are unfavorably oriented (i.e. perpendicular) relative to the loading direction (**Figure 5-20d**) or the one made of entangled or thin walls (**Figure 5-20b**). As the compressive stress increase, the deformation proceeds in the bottom half of the foam as depicted in **Figure 5-20c**. The deformation is accommodated by buckling of the cell walls and cracking of the cell membranes (see black arrows in **Figure 5-20b**). Moreover, the structure deformed

during the first stages of the deformation also causes damages by being pushed downwards and inducing tearing of the cell membranes and walls. It is visible in **Figure 5-20d**.

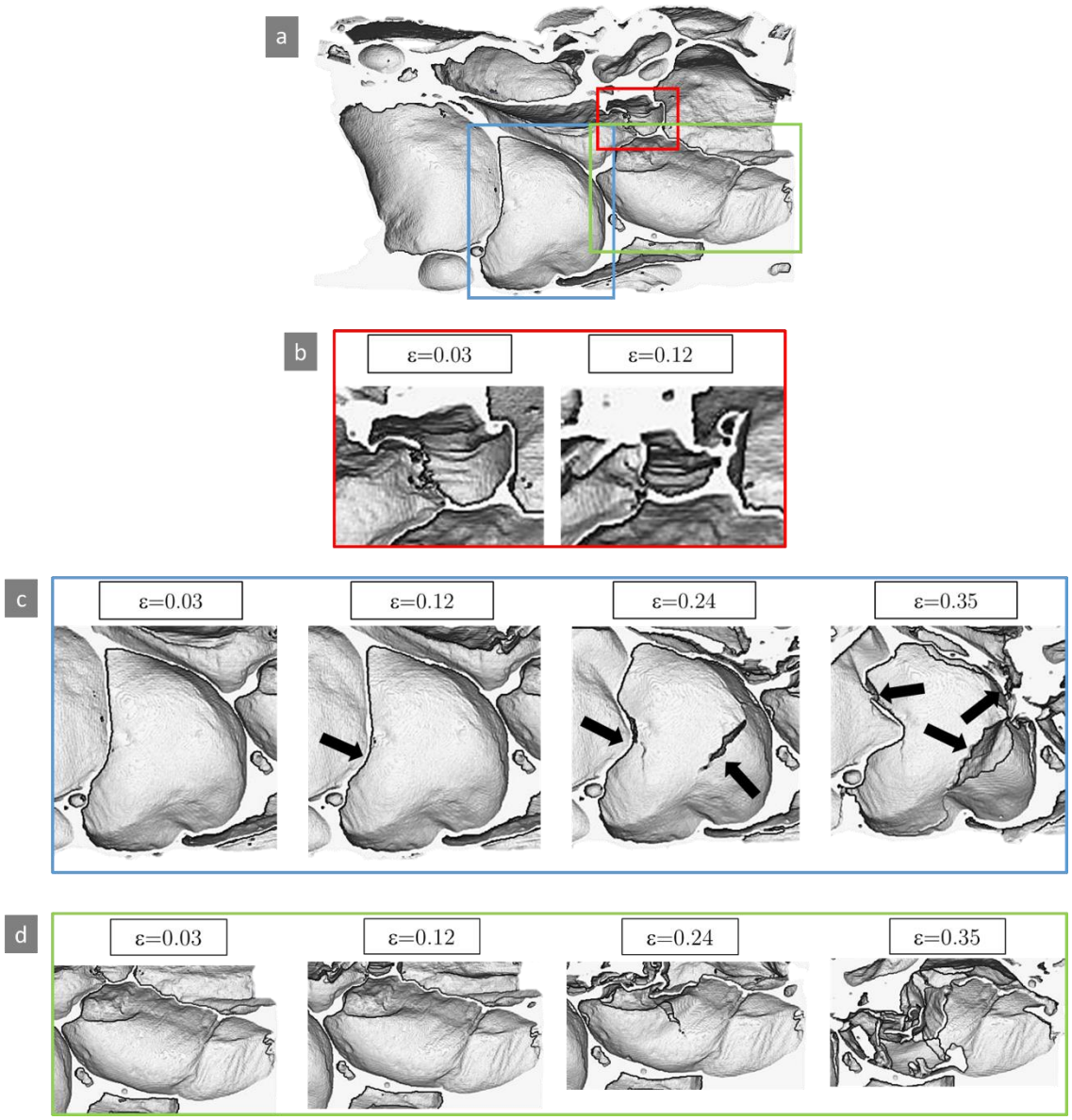

Figure 5-20. Deformation mechanisms of the individual cells. (a) Global view of the cross section. (b) Evolution of a cell as the strain increase. (c) The black arrows indicate the deformation of the cell walls and the crack appearing in the cell membrane. (d) The failure occurs by the top structure being pushed down.

Figure 5-21 illustrates the deformation of sample 2, which was ultimately deformed at a higher strain compared to sample 1 (0.43 as opposed to 0.35 for sample 1). Similarly, to **Figure 5-19**, the black dashed lines are placed at 5.5mm from the bottom of the foam, which corresponds to the location of the onset of densification as observed in **Figure 5-18b**. By following the evolution of the structure relative to the position of the black lines, it is obvious that the densification takes place primarily in the upper half of the foam and it is not until sufficient deformation is reached (i.e. ε=0.43) that the bottom half heavily deforms. The densification initiates in the middle section and is manifested by a subsidence of the structure related to the presence of a weak cell surrounded by thin and entangled walls. This weak region is indicated by the blue circle in **Figure 5-21a**. The impact of the subsidence on the surroundings is indicated by the highlighted cells in **Figure 5-21b** whose shape is directly altered by the collapse of the weak region mentioned above. Cracks in the cells membranes accommodate the change of shape of the cells and are indicated by the black arrows in **Figure 5-21b**. As the strain increases, the deformation diffuses in the lower half of the foam indicated by the gradual collapse of the cell highlighted in **Figure 5-21c** whose walls start bending because of the strain but also because of the above structure being pushed down. It is further exemplified in **Figure 5-21d**. At this stage, the upper half is almost completely densified and has been pushed downwards causing the deformation of the lower half.

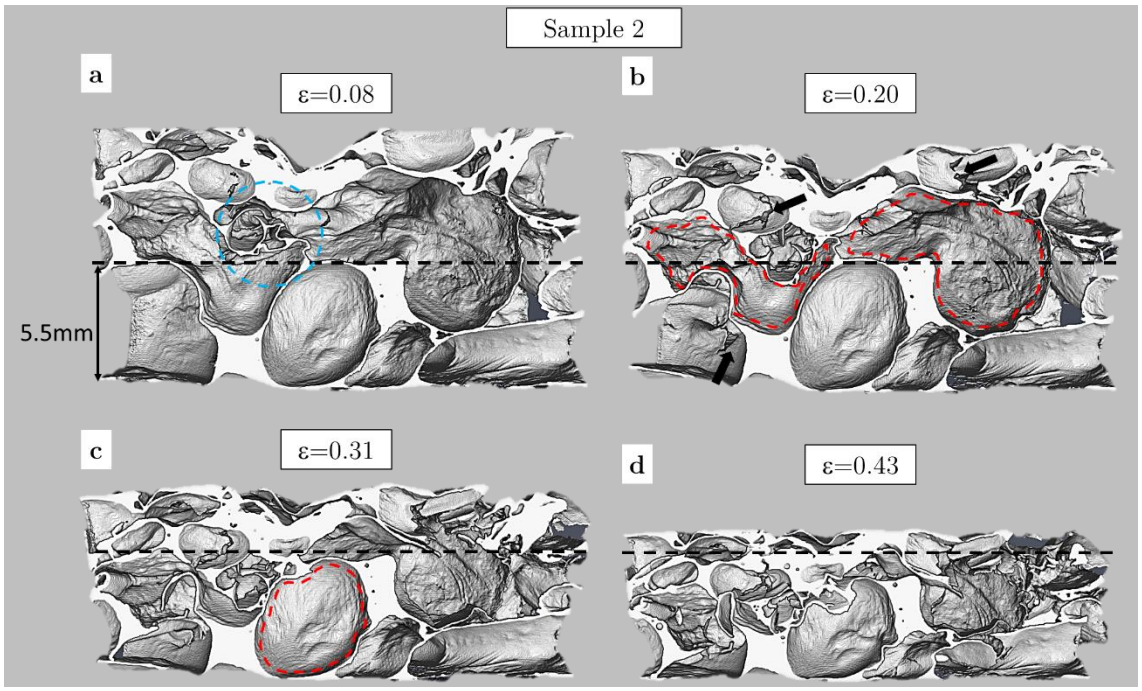

Figure 5-21. Evolution of the cellular structure at different applied strains (sample 2). (a) The blue circle indicates a weak region of the structure. (b) The red dashed lines highlight the change of shape of the cells affected by the presence of the weak region indicated in (a). The black arrows point to the cracks in the cell membranes. (c) The red dashed line highlight the deformation of a cell located in the lower half of the foam. (d) Final stage of deformation

Finally, **Figure 5-22** shows a horizontal cross section of sample 1 that is perpendicular to the loading axis. It was taken at 5.5mm from the bottom of the foam, which corresponds to the location of the onset of densification as illustrated in **Figure 5-18**. It is particularly tricky to find the exact same cross section for each strain increment as the structure moves significantly during deformation; therefore, some differences can appear from one image to another.

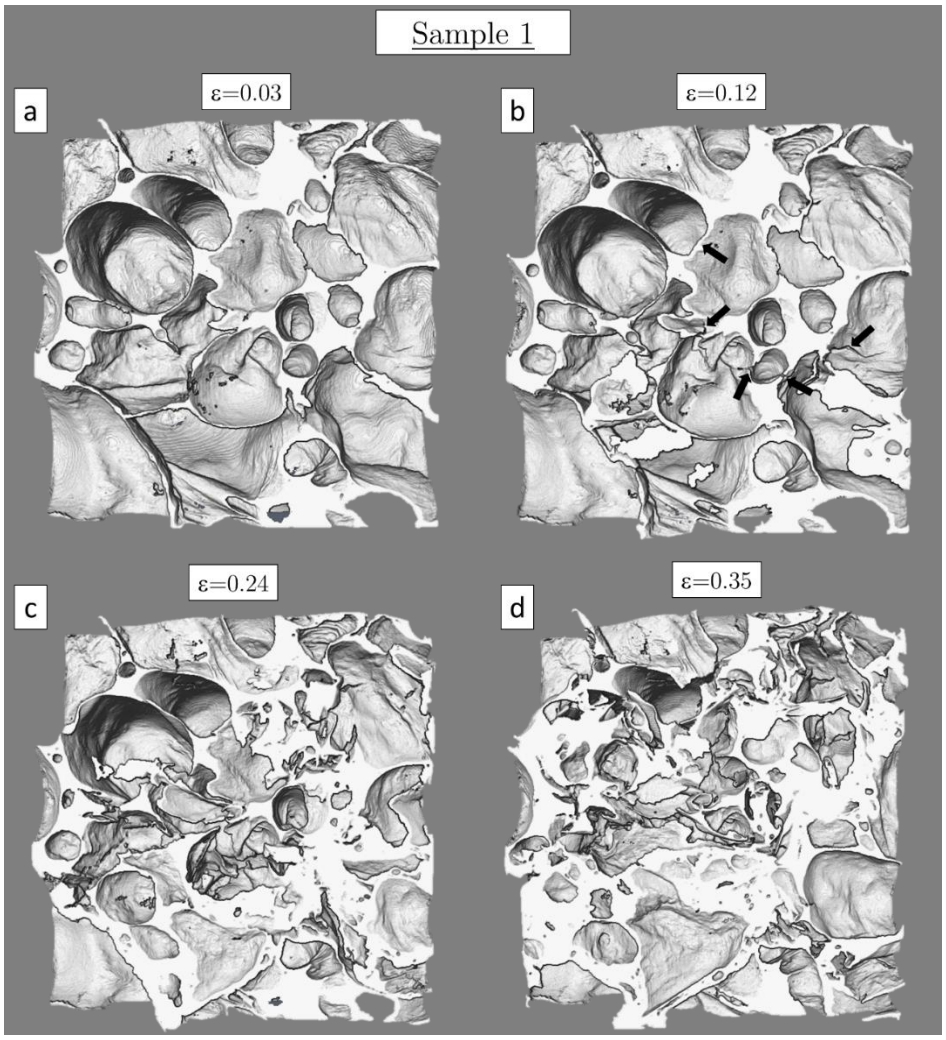

Figure 5-22. Evolution of the cellular structure in a horizontal cross section perpendicular to the loading direction at different applied strains (sample 1). The cross section is located at 5.5mm relative to the bottom of the foam corresponding to the onset of deformation determined in **Figure 5-18**. The black arrows in (b) point to the location of the first events of deformation.

The same conclusions as before can be made. The deformation seems indeed localized in this section of the material as we observe signs of deformation on **Figure 5-22b** indicated by the black arrows. **Figure 5-22c** and **Figure 5-22d** shows the same cross section for higher strain increments. A lot of the structure has moved and it is therefore difficult to visualize the initial structure. However, we can see that tearing and fracture of the cell faces and walls take place.

Summary of the deformation mechanisms of the foam by tomography

In-situ micro X-ray Computed Tomography tests of foam samples under progressive compressive loading were carried out to study the evolution of the structure while deforming. It was found that the deformation occurs first in the middle section of the sample where the relative density is low. The deformation occurs first by buckling and bending of the cell walls, which can induce cracking and tearing of the cell faces. The damages intensify and the deformation propagates to the neighboring cells until all the structure has failed after which densification takes place. It has been observed on both samples for different cross sections. Both vertical and horizontal cross sections were observed to try to extract a deformation pattern. It has also been seen that the lower section of the foam undergoes little deformation compared to the top section. It is partially explained by the relative density analysis presented previously that reveals a very high increase of relative density (about 40%) in the lower section of the foam.

The results are consistent with the literature. Indeed, it has been observed that the deformation of a foam occurs in the weakest cells of the structure. Those weak cells are defined as the elongated ones (i.e. perpendicular to the loading direction) which are unfavorably oriented with the loading direction but also the ones made of entangled or thin walls. The deformation is highly inhomogeneous and the densification is the result of multiple local deformation events occurring at the cell level.

2.2. Microscale characterization of the mechanical properties by nanoindentation

The nanoindentation cartography, introduced in the previous chapter is now used to characterize the hardness of individual cell walls and especially the dendritic phase. Because of the inhomogeneity of the cell walls, several areas were indented and will be presented. The effect of composition, with a strong focus on the silicon content in the aluminum solid solution is discussed. Finally, the nanoindentation has been associated with a peak deconvolution of the statistical analysis of the hardness data in order to reveal a possible difference of hardness between the eutectic and dendritic aluminum phases.

2.2.1. Nanoindentation behavior

The mechanical properties of the cell wall at the microstructural level were investigated using nanoindentation. **Figure 5-23** illustrates the loading sequence used during the nanoindentation tests of the foam in this chapter. The loading is performed in depth control, at a penetration speed of 300nm/min, to ensure that each indentation have the same maximum penetration depth, without regard to hardness. The maximum depth of the indentations is 150nm. The unloading is performed in load control at 2000μN/min. The step size of the arrays for the reconstruction of the hardness and Young's modulus cartographies may vary depending on the area tested.

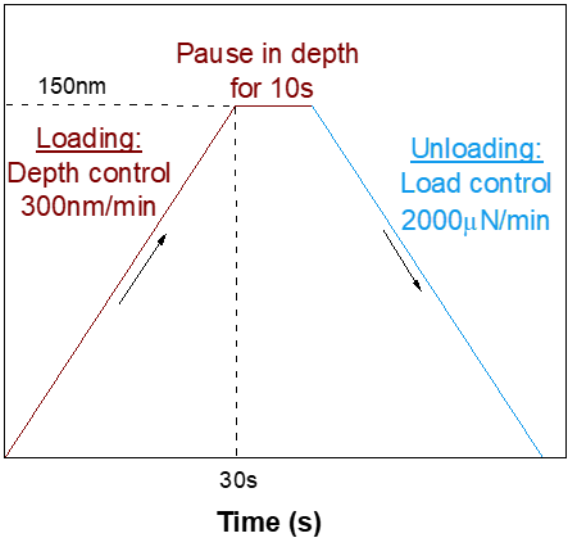

Figure 5-23. Indentation profile. The loading is depth controlled to assure a constant penetration of all the indentations while the unloading is load controlled.

Two major nanoindentation behaviors stand out corresponding to the aluminum and the silicon as illustrated in **Figure 5-24a** and **b** respectively. The aluminum essentially exhibits a plastic deformation with a ductile behavior illustrated by the almost vertical unloading curve. On the other hand, the silicon shows an elasto-plastic deformation with a strong elastic recovery during the unloading. The unloading part of the silicon curve reveals a displacement discontinuity, called pop-out, at around 100nm resulting from a phase transformation and associated with a sudden expansion of the material [141], [142]. It typifies the indentation behavior of silicon.

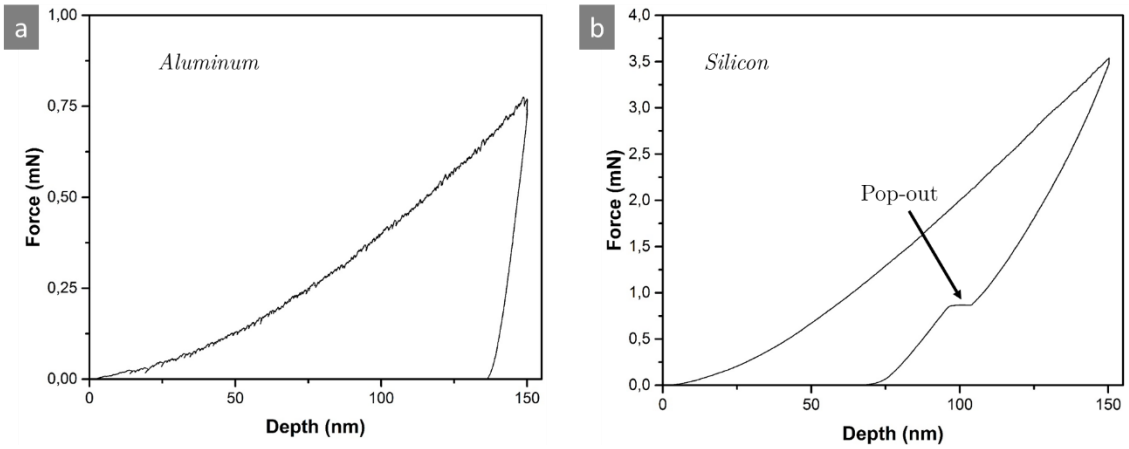

Figure 5-24. Characteristic load vs. displacement curves for (a) the aluminum phase (both eutectic and dendritic) (b) the eutectic silicon phase.

2.2.2. Nanoindentation cartography of the dendritic phase

Cartography n°1

This first cartography is mainly designed to adjust the parameters of the cartography and gather early information on the indentation behavior of the microstructure. The results are summarized in **Figure 5-25**. The array overlies the dendritic and eutectic phases but most of the indentations are localized in the dendritic phase. The step size is 2µm. The grey color on both maps corresponds to the values outside the scale. The array was designed to be 10x25 indentations but the procedure failed at the 203rd indentation resulting in a big imprint on the bottom right corner of the image.

The map in **Figure 5-25b** reveals a preferential distribution of the hardness values. The hardness is higher in the top left corner and decrease continuously when approaching the eutectic phase. The values range between 1300 and 1800MPa. The modulus varies between

80 and 110GPa but no tendency is observed, the distribution is homogeneous. Moreover, no correlation between the modulus and hardness values is detected.

It is difficult to identify where the preferential distribution of hardness originate from just from the optical image and the maps. However, as highlighted previously from the TEM analysis, Si-rich clusters and precipitates were observed in the dendritic phase. As described by Mott and Nabarro, the presence of atoms of a second phase inside a solid solution locally induces strains resulting in an apparent increase of hardness. Therefore, the distribution of hardness is most likely the consequence of the presence of precipitates.

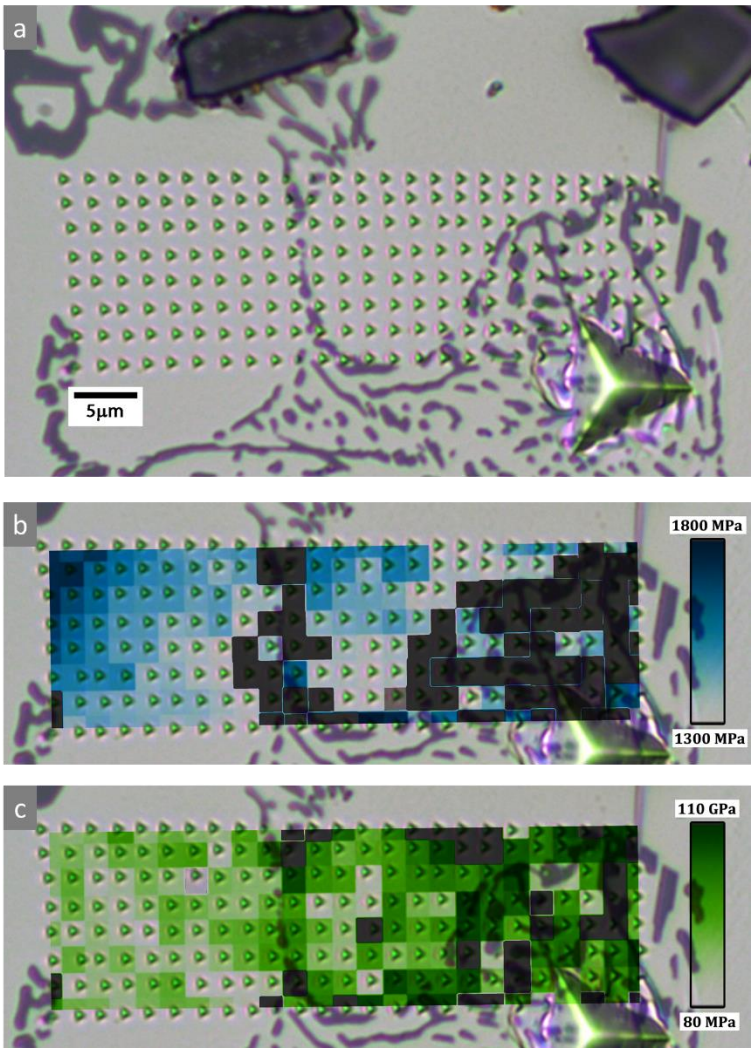

Figure 5-25. Cartography n°1 (a) Optical micrograph of the surface after indentation. The array is made of 10x25 indentations. (b) Nanohardness cartography reconstructed from the array shown in (a). Each square represents a single nanohardness value. (c) Cartography of Young's modulus from the array shown in (a).

Cartography n°2

Following the previous cartography, which focused on the dendrite/eutectic region, the influence of Mg was quantified by indenting an Mg-rich precipitate. There are a number of microstructural features that affect the ductility of aluminum casting alloys. The ductility is known to be sensitive in various degrees to the dendrite cell size and silicon particle size,

the aging condition but also the magnesium content [143], [144]. **Figure 5-26** summarizes the results of hardness and modulus corresponding to the array shown **Figure 5-26a** using a 2µm step size. This array was built on an Mg-rich particle indicated by the distinct contrast of the particle compared to the rest of the image.

The map in **Figure 5-26b** depicts hardness values ranging from 1500MPa to 2100MPa. Those values are higher than the ones measured in the previous example. Here, the higher values are localized around the Mg-rich particle suggesting that the Mg precipitate influences its surrounding properties. However, the indented area is small and it would have needed a bigger array to be sure that the tendency observed extend to the rest of the region.

Similarly, to the previous cartography, the local inhomogeneities of the ductile dendritic phase in terms of hardness values are unveiled. Moreover, the role of the chemical composition of the Al-rich phase is again questioned.

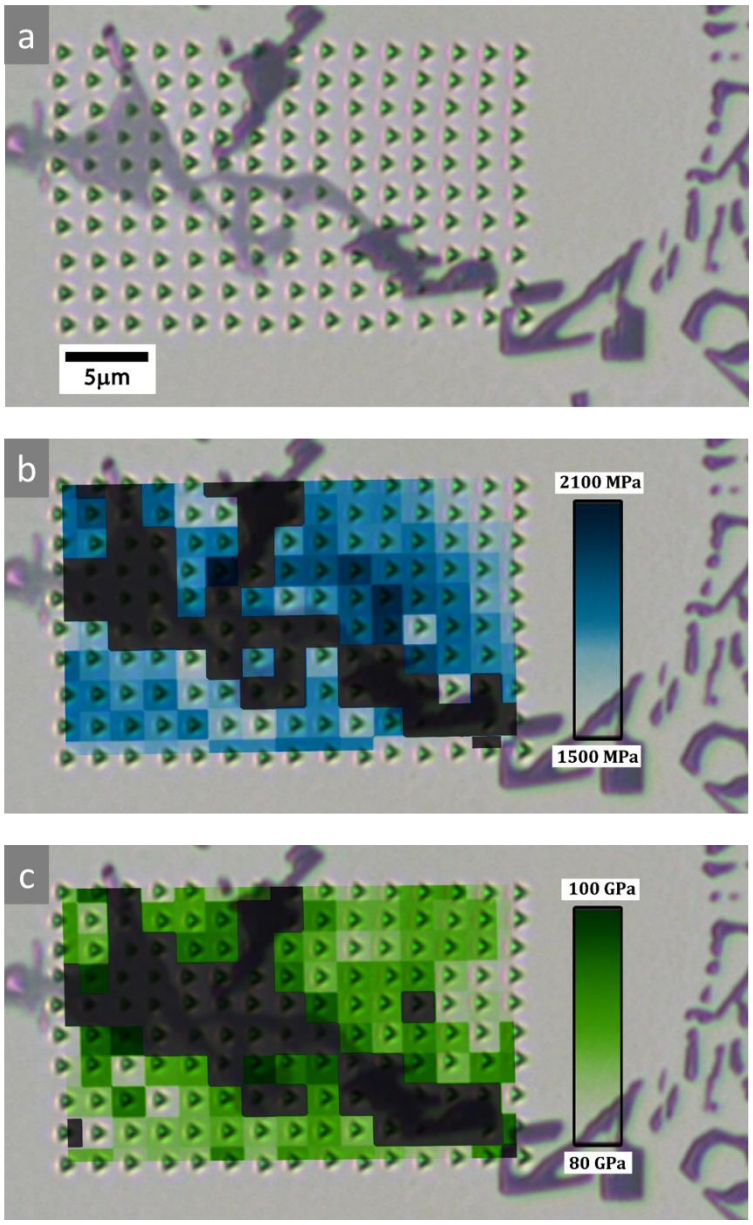

Figure 5-26. Cartography n°2 (a) Optical micrograph of the surface after indentation. The array is constituted of 15x10 indentations with a step size of 2µm. (b) Nanohardness cartography reconstructed from the array shown in (a). (c) Cartography of Young's modulus from the array shown in (a).

Cartography n°3

The appropriate parameters of the cartography were determined with the two previous cartographies. In an attempt to assess more accurately the correlation between chemical composition and hardness, the cartography by nanoindentation is coupled to an EDS cartography for the analysis of the dendrite in cross section. Additionally, the potential variation of hardness between the eutectic and dendritic aluminum are investigated by performing an analysis of the statistical distribution of the hardness values.

Figure 5-27 compiles the outcome of the nanoindentation cartography performed on what is considered as the cross section of a dendritic arm using a 2µm step size. **Figure 5-27b** depicts the hardness distribution of the indented area. It suggests a lower hardness on the edges, at the eutectic/dendritic interface, compared to the core of the dendrite. The hardness ranges between 1200MPa at the edge and 1500MPa in the core. **Figure 5-27c** illustrates the young's modulus of the indented area. No observable trend stands out with values ranging between 80 and 100GPa. Finally, **Figure 5-27d** depicts the elemental Si composition of the dendrite as quantified by EDS and unveils a clear gradient of Si content along the radius of the dendrite. Here, the core is associated with higher Si contents compared to the edges. The Si content ranges from 1.2 to 3%.

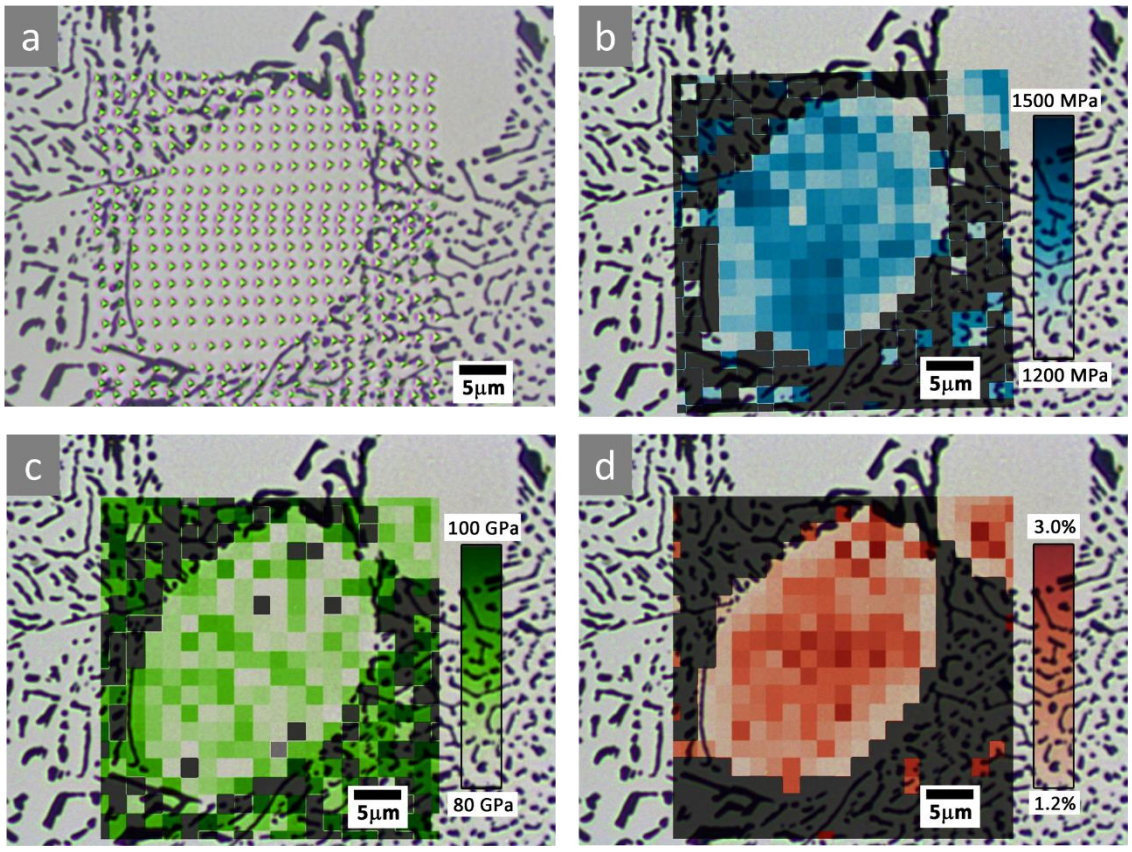

Figure 5-27. Cartography n°3 on the cross section of a dendritic arm. (a) Optical micrograph of the surface after indentation. The array is constituted of 20x20 indentations with a maximum penetration depth of 150nm. The step size is 2µm. (b) Nanohardness map (c) Young's modulus map (d) Si percent concentration map.

From **Figure 5-27b** and **Figure 5-27c**, one could say that the hardness exhibits a correlation with the Si content. Here, higher hardness values appear to be associated with higher Si content. Thus, to confirm this correlation, each hardness value was associated with a corresponding Si concentration and plotted resulting in **Figure 5-28**. Despite some scattering in the data points, the trend noticeably shows an increase of hardness when the Si content increases.

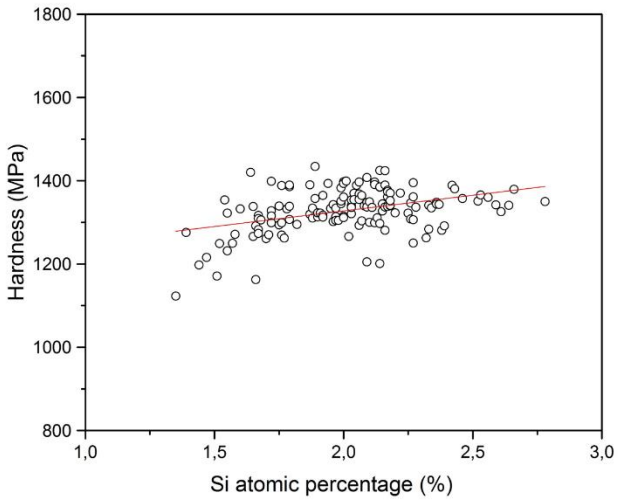

Figure 5-28. Plot of the hardness vs Si content. The same data were used to reconstruct the maps shown in Figure 5-27. The red line represents the trend of the data points.

The Si atomic percentages measured by EDS challenge the analysis of the Al-Si phase diagram. According to the diagram, the maximum solubility of Si in Al is 1.65% at 577°C and close to zero at room temperature. However, this solubility (and by extent the entire phase diagram) applies only in equilibrium for which the cooling rate is low. Obviously, in the case of a foam manufactured by gas melt injection, the equilibrium conditions are not fulfilled. Physically, it means that the solute atoms do not have enough time and energy to diffuse from the dendritic phase to the eutectic phase. Instead, they will form clusters and/or precipitates, as it is more energetically favorable. This mechanism is more pronounced at the core of the dendrite, manifesting itself by higher Si contents measured by EDS. This phenomenon is corroborated by the calculation of the solidification time made earlier in the chapter (see chapter 4 section 1.3). The calculated time for the specific region showed is

5.3s, which is very short regarding the time needed to form the microstructures predicted by the Al-Si phase diagram.

The array overlies both the eutectic and dendritic phases. Thus, it gives us the opportunity to investigate the potential variations between the eutectic and dendritic aluminum. According to the phase diagram, both phases are α-Al and should have the same composition. However, the environment of each phase is different. The dendritic aluminum solidifies alone while the eutectic aluminum solidifies simultaneously with the Si platelets and after complete solidification, the eutectic aluminum is tangled with Si platelets. A potential effect on the hardness is investigated. To this end, an analysis of the statistical distribution of the hardness values was performed to deconvolute the hardness peaks associated with the different mechanical phases. This approach is particularly interesting when the different phases are hardly identifiable. The array presented in **Figure 5-27** was used. The statistical deconvolution was performed according to the method proposed by Ulm et al. [112]. An example of its application can be found in the literature [115]. Three types of behaviors can be considered relative to the region indented. The first one is when the dendritic aluminum is indented, the second when the eutectic aluminum is indented and the third corresponds to a hybrid behavior when the indent overlaps the eutectic aluminum and Si platelets. It results in three deconvoluted peaks as shown in **Figure 5-29a**. A Gaussian distribution was assumed for each phase. The first peak (blue) is located at 1172MPa with a full width at half maximum (FWHM) of 167MPa. The second peak (orange) is located at 1343MPa with a FWHM=86MPa. Because the PDF of this peak is so high and because

majority of the indentations were located in the dendrite, this hardness value is most likely to be the hardness of the dendritic phase. Finally, the third peak (pink) is positioned at 2067MPa with a FWHM=2750MPa. The high FWHM of this peak is attributed to the composite behavior of the indentation when the indenter is in partial contact with the Si and Al phase.

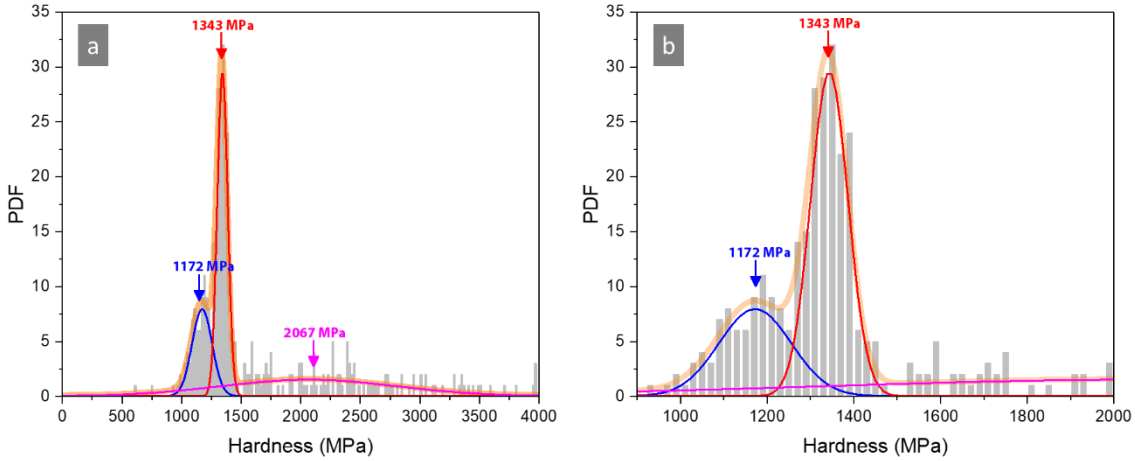

Figure 5-29. Experimental data (histogram) and associated probability density function (PDF) (a) Full data (horizontal axis 0-4000MPa) (b) Zoom in on the aluminum peaks (horizontal axis 900-2000MPa). On both plots, the yellow line is the envelope of the PDF. The blue, orange and pink curves are the deconvoluted PDF's assuming a Gaussian distribution for each phase.

The two sharp peaks are only 171MPa apart, which can appear low and not conclusive. To confirm the nature of the peaks, a hardness cartography of the full data has been established (i.e. no values were saturated) and superimposed to the optical image of the indented area. The color scale has been chosen in order to reveal the three main hardness values: the color has been used with sharp transition in between the deconvoluted peaks. The results are shown in **Figure 5-30**. The deconvoluted PDF's from **Figure 5-29** are associated with the hardness color scale.

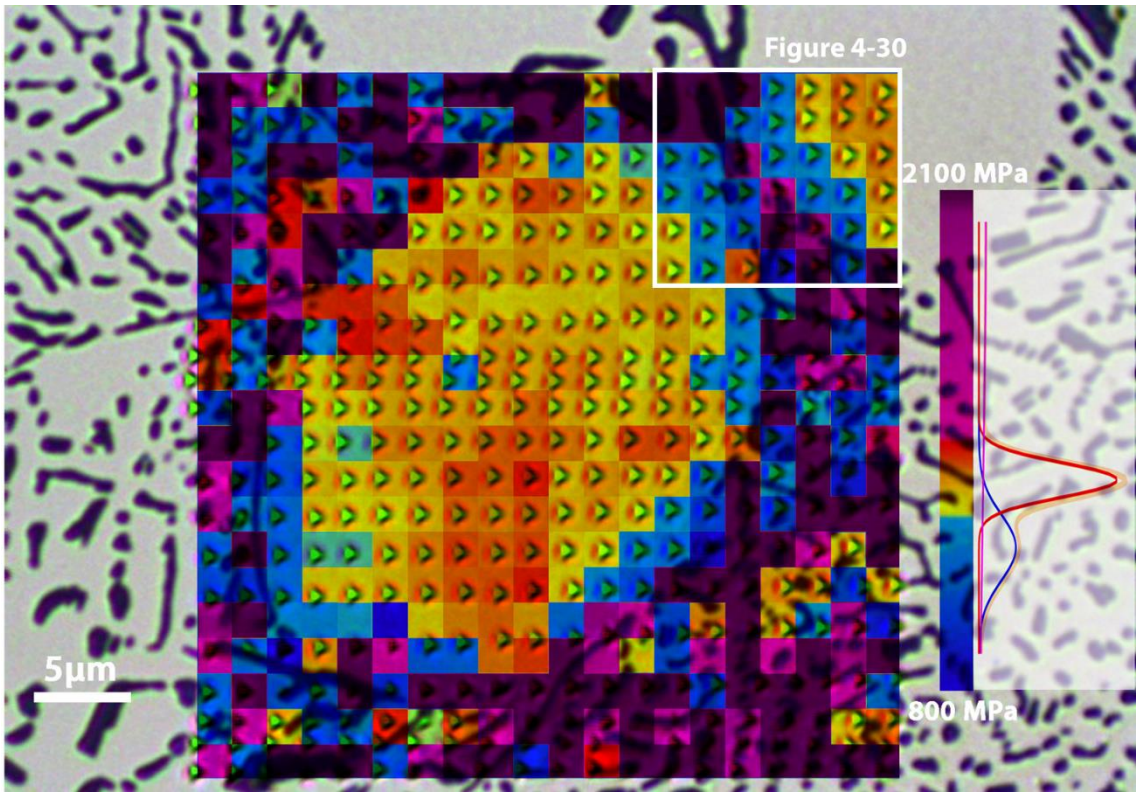

Figure 5-30. Hardness cartography of the array shown in **Figure 5-27** superimposed on the optical image of the indented area. The deconvoluted PDFs from **Figure 5-29** are associated with the hardness color scale. The white square on the top right corner corresponds to 4-30.

The blue color is associated with the 1172MPa peak while the orange values are associated with the 1343 peak. The pink color is associated with the 2047MPa peak. The cartography suggests that the lowest hardness values, corresponding to the blue color, are primarily located in the eutectic phase or at the dendrite/eutectic interface. The dendrite appears in orange, thus showing that the hardness in these regions is about 1350MPa and corresponds to the second peak. However, it is challenging to distinguish clearly a hardness contrast in the hardness map in the eutectic phase. Thus, a zoomed in version of the top right corner

of the cartography is presented in **Figure 5-31**. In this image, the cartography is superimposed on the SEM image of the indented area to improve the visibility of the indentations. The color chart is similar to the one in **Figure 5-30**. But ranging from 800 to 4100 MPa

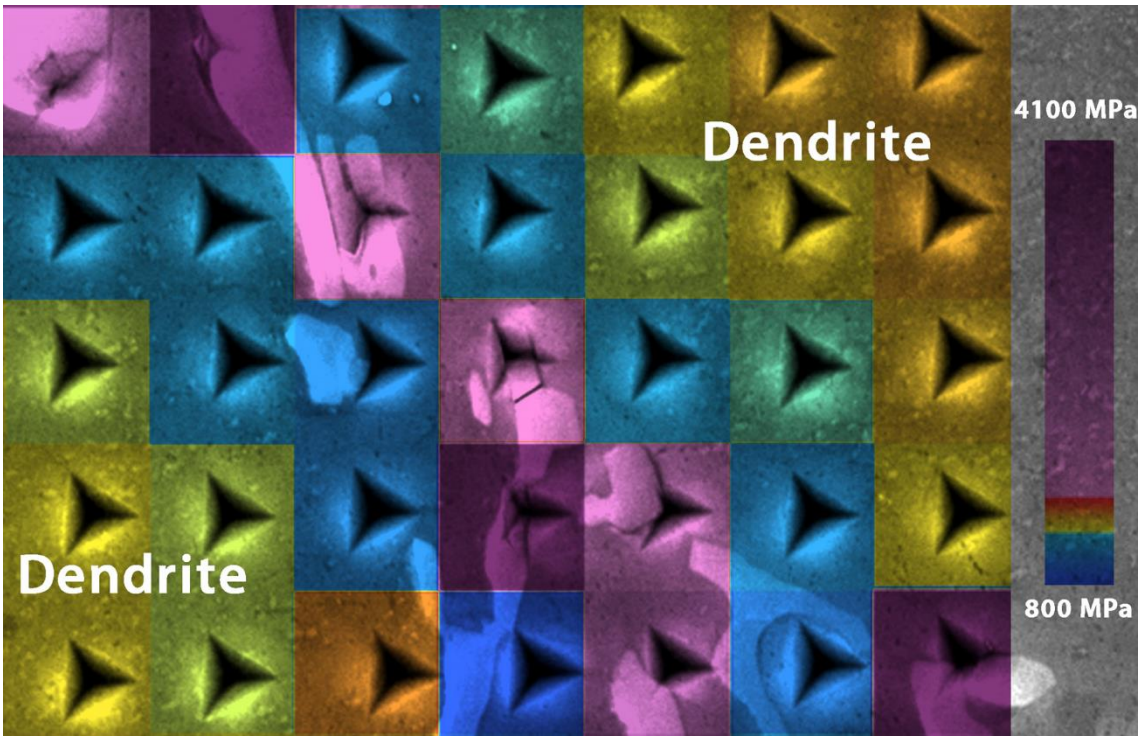

Figure 5-31. Image extracted from the cartography in **Figure 5-30**. The hardness cartography of the array shown is here superimposed on the SEM image of the indented area to better distinguish the indentation. The color chart is similar to the one in **Figure 5-30**.

Figure 5-31 clearly shows the position of the indents relative to the different phases. The indents located in the dendrites appear in orange, confirming that the 1343MPa peak in **Figure 5-29** corresponds to the hardness of the dendritic aluminum. Thanks to the quality of the SEM image, the indents overlapping the eutectic Al and Si are distinctly visible and appear in pink color showing that they are associated with the third peak. At

last, the indents located in the pure eutectic aluminum phase (without any contact with the silicon platelets) appear in blue color, which confirms that the 1172MPa peak in **Figure 5-29** corresponds to the eutectic aluminum hardness.

Even if the hardness is only 171MPa apart, the hardness of the eutectic and dendritic aluminum was shown to be different. The dendritic phase has higher hardness compared to the eutectic aluminum phase. The method allows revealing small hardness variations between the two aluminum phases, which would have been difficult to extract in a conventional hardness study. The variations of hardness can ultimately lead to strain localization and to the nucleation of crack within the cellular structure. Within the context of the multiscale characterization of the foam, it accentuates the presence of various microstructural interfaces and the inhomogeneity of the microstructure.

Summary of the microstructural characterization by nanoindentation cartography

The nanoindentation cartography method has been used to reveal and to characterize the inhomogeneities of mechanical properties of the microstructure. The silicon platelets and aluminum have two very different behavior when indented. The aluminum exhibit a plastic deformation with a ductile behavior and the silicone an elasto-plastic behavior with a strong elastic recovery upon unloading.

A detailed analysis of the dendritic phase revealed a gradient of hardness within the dendritic structure. This gradient is distributed relative to the position inside the dendritic arm. The core has higher hardness compared to the edge. This distribution derives from a

corresponding distribution of silicone in the solid solution, which is most likely a consequence of the non-equilibrium cooling conditions during the foam manufacture. Overall, the hardness of the aluminum is strongly affected by its elemental composition. The presence of Si and Mg in solution greatly modifies the hardness of the aluminum phase.

The nanoindentation cartography was further used to investigate the properties of the eutectic aluminum relative to the dendritic one. The deconvolution performed on the statistical analysis of an indentation array overlying both phases confirmed a lower hardness of the eutectic aluminum. Only 171MPa separates the hardness of both phases, which would have been undetectable by conventional nanoindentation. Coupling the deconvolution with a hardness cartography confirm the distinct properties of both phases. A possible effect on macroscopic deformation behavior of the foam was raised as the variations of hardness between the two ductile aluminum phases can lead to strain localization and ultimately to crack nucleation at the macroscopic scale.

2.3. Characterization of the deformation mechanisms at the nanoscale

2.3.1. Nanoindentation curve analysis: PLC effect

The influence of the elemental composition, and more specifically the Si content, on the hardness was demonstrated. In this section, the indentation curves are analyzed and the strengthening role of Si in the aluminum phase is investigated. The benefit of the nanoindentation cartography is therefore extended and the technique is no longer used as a

conventional hardness measuring technique but as a way to study the deformation behavior at the nanoscale.

Instabilities are observed on the load-displacement curve when indenting the aluminum phase (eutectic or dendritic). Those instabilities are manifested by oscillations on the loading part of the curve as exemplified in **Figure 5-32** which depicts a typical load vs. displacement curve of the dendritic aluminum. It is also known as the Portevin-Le Chatelier (PLC) effect.

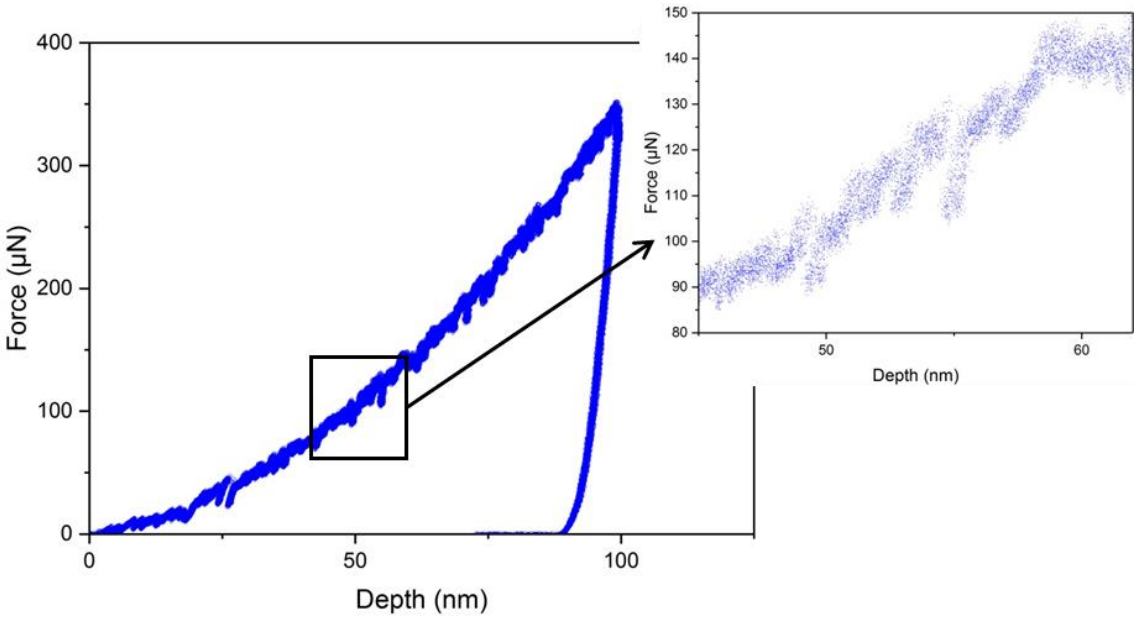

Figure 5-32. Instabilities on the load-displacement curve appearing when the aluminum phase is indented.

The PLC effect, serrated yielding or jerky flow described originally the serration observed on the tensile stress-strain curve of some dilute alloys and particularly Al alloys. This phenomenon represents a material instability that results in severe strain localization, reduction in ductility and formation of striations on the surfaces of sheet metals during forming processes. It is now accepted that the serrations originate from dynamic strain aging

of the solute atoms. Physically, this phenomenon is the result of the interaction of mobile dislocations with solute atoms, which encompasses pinning of the dislocations by the solute atoms, the breakaway of the dislocations from the solute atoms, and diffusion of the solute atoms to the dislocations, which are therefore pinned again.

It has mainly been studied for aluminum alloys with a focus on Al-Mg alloys. Recently, nanoindentation revealed itself to be a great tool to study the PLC effect as similar serrations were observed on the load vs. displacement curves of dilute alloys [145]–[149] . Nanoindentation provides further insight since it makes possible to evaluate the properties of individual phase. Therefore, a much more local information is obtained.

The elemental characterization of the microstructure by EDS showed variable silicon content in both the eutectic and dendritic aluminum phases. The silicon in solid solution is most likely to induce the serrations. Thus, the objective is to analyze the serrations of the load-displacement curves of several imprints relative to their position inside the dendritic structure. The U-NHT "Ultra nano hardness tester" by ANTON PAAR was used to conduct the nanoindentation experiments. Unlike conventional nanoindentation systems, the nanoindenter has two independent high-resolution load and displacement sensors. In addition, the active reference provides an extremely high mechanical stability. The serrations on the curve are therefore a physical response from the material and are not induced by the device (see Chapter 2 for more details).

An array of 5x15 indentations was designed over a dendritic arm as shown in **Figure 5-33**. The indentations were performed with an acquisition rate of 400Hz, i.e. 400 data points collected per second, to ensure the detection of the load jumps. The step size of the array is 3μm. The loading is performed in displacement control at 50nm/min while the unloading is performed in load control at 1500μN/min. The maximum depth of the indentation is 100nm.

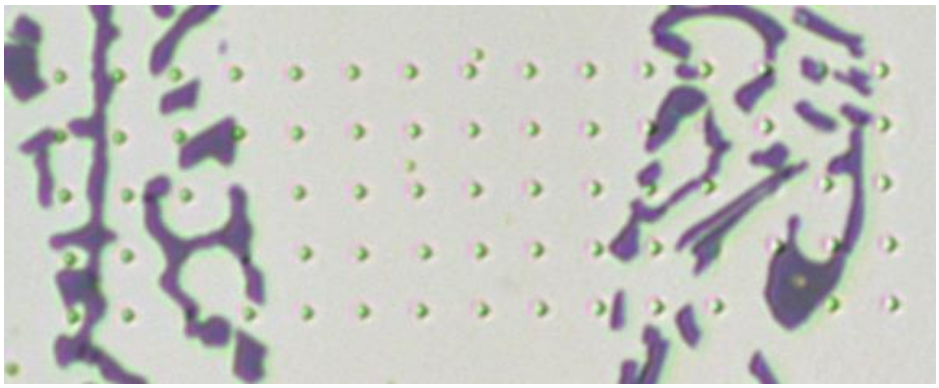

Figure 5-33. 5x15 nanoindentation array over a dendritic arm. The indentation cycle is specifically developed for the analysis of the PLC effect.

The procedure to analyze and compare the load drops from one curve to another is illustrated in **Figure 5-34**. First, the load and displacement signal are plotted as a function of time as shown in **Figure 5-34a**. Only the loading portion of the load signal is displayed while the entire indentation cycle of the displacement signal is plotted. The displacement signal is linear since the loading is controlled in displacement and the instabilities of the load signal are clearly visible. From the data, the envelope of the load signal is determined (orange curve in **Figure 5-34a**) and subtracted in order to isolate the serrations and obtain a plot

as shown **Figure 5-34b**. Finally, the position and amplitude of the load drops are automatically detected, recorded and indicated in order to perform a statistical analysis. The results are shown in **Figure 5-34c**. The green bars indicate the position of a load drops. The numbers above each bar correspond to the amplitude of the load drops in micronewtons.

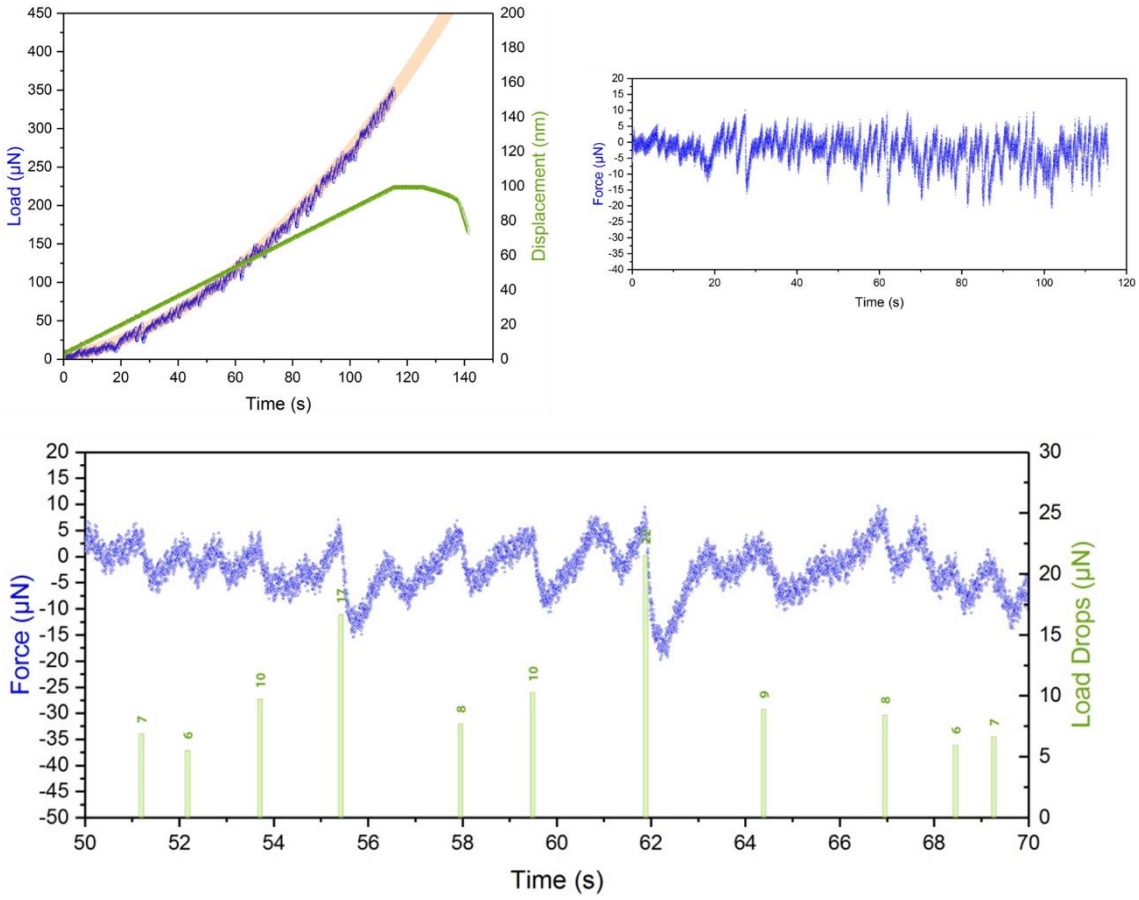

Figure 5-34. Procedure of the statistical analysis of the serrations (a) Load and displacement signals as a function of time. (b) Load signal as a function of time after subtraction of its envelope. (c) Results of the statistical analysis of the load jumps. Each green bar represents a load drop.

Figure 5-35 summarizes the results of the load drops analysis. The figure shows only the results of one line of indents. Within this line, only the results of the indentations numbered 63, 66, 69 and 74 are displayed as they described well the different possible cases.

Indentation 63 corresponds to the indentation of a eutectic Si platelet, indentation 66 is located in the dendritic phase at the interface between the eutectic and dendritic phase, indentation 69 is located at the core of the dendritic arm and indentation 74 is located in the eutectic aluminum phase. First, the curve numbered 63 does not exhibit load jumps. The silicon platelets are pure silicon and the serrations only appear in solid solution. It is therefore natural that no load drops were detected. Despite the different locations of indentations 66, 69 and 74, i.e. different locations inside the dendritic arm for 66 and 69 and different phase for 74, no significant differences are observed.

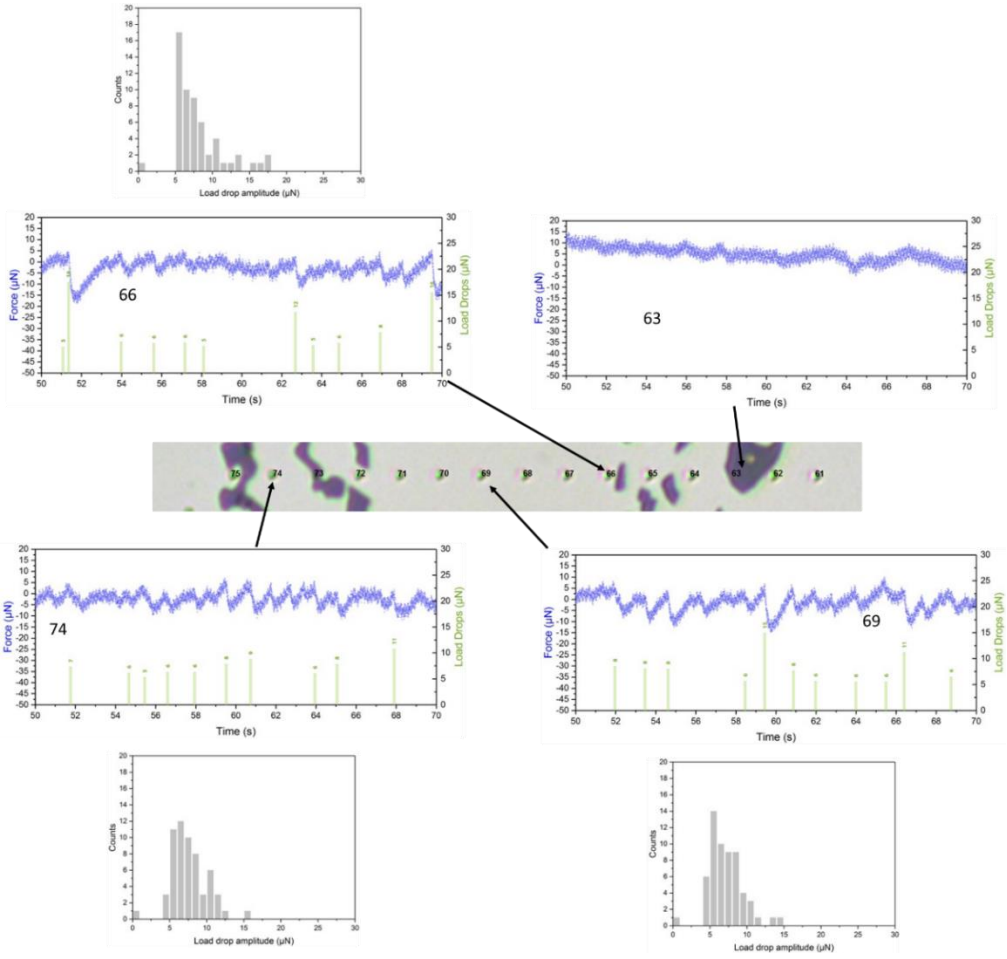

Figure 5-35. Results of the statistical analysis of the load jumps relative to the location in the dendritic arm.

The presence of load drops in the eutectic and dendritic aluminum confirms the presence of solute atoms or nano-precipitates in both phases [147], [150]. However, the TEM characterization presented earlier in this chapter revealed precipitates below 10nm but their number and spacing cannot explain the multitude of drops. Thus, the presence of smaller precipitates or aggregates must exist to account for the oscillations on the nanoindentation curves. Above all, the PLC point out pinning of dislocations. The TEM is a common tool to examine the dislocations structure.

2.3.2. Characterization of the dislocation structure by TEM

In this section, TEM is used to image the interaction of dislocation with the microstructure. Here, dislocation/precipitate interactions were detected via the observations of dislocation pinning and loops. The thin foil was extracted within the indented area shown in **Figure 5-33**. The pinning phenomenon is illustrated in **Figure 5-36**.

Two different regions are enlarged but both highlight the pinning of dislocations as seen in **Figure 5-36b** and **d**. In both cases, the pinning is caused by the largest precipitates presented earlier (≈20nm).

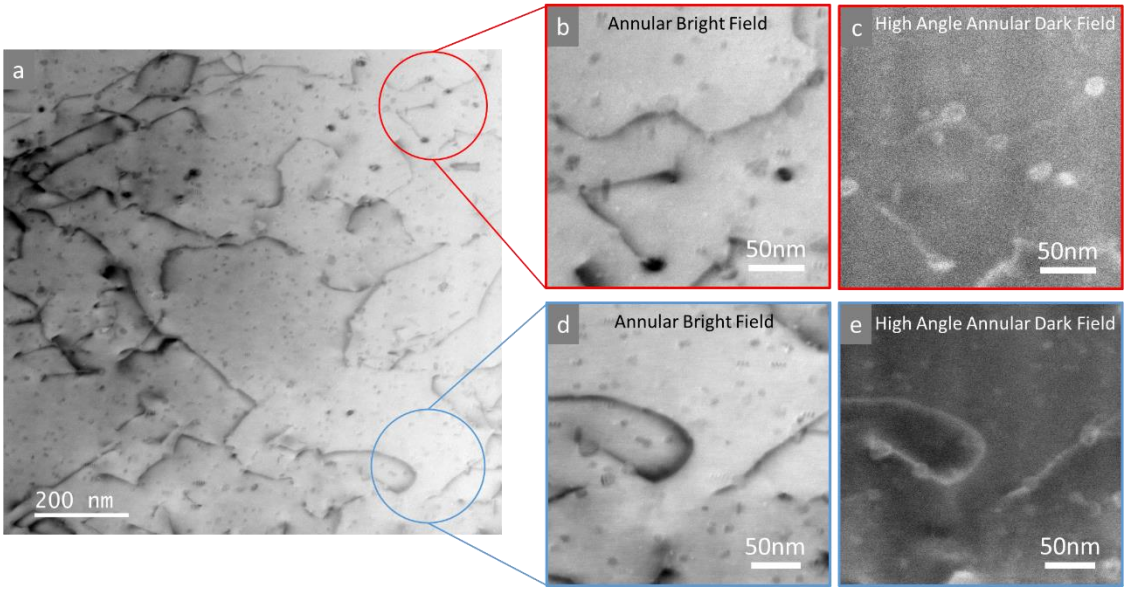

Figure 5-36. (a) Annular Bright Field STEM image in the dendritic phase. (b) and (c) Annular bright Field and High Angle Annular Bright Field images respectively of the encircled region in red. (d) and (e) Annular bright Field and High Angle Annular Bright Field images respectively of the encircled region in blue.

Dislocations loops are additional proofs of dislocation/precipitates interaction and results from the encirclement of a precipitates by a moving dislocation leaving a loop behind. **Figure 5-37** illustrates this phenomenon in two different regions indicated by the white circles. The diameter of the loops is close to 20nm suggesting again that the dislocation interacted with the bigger precipitates (Orowan looping mechanism)

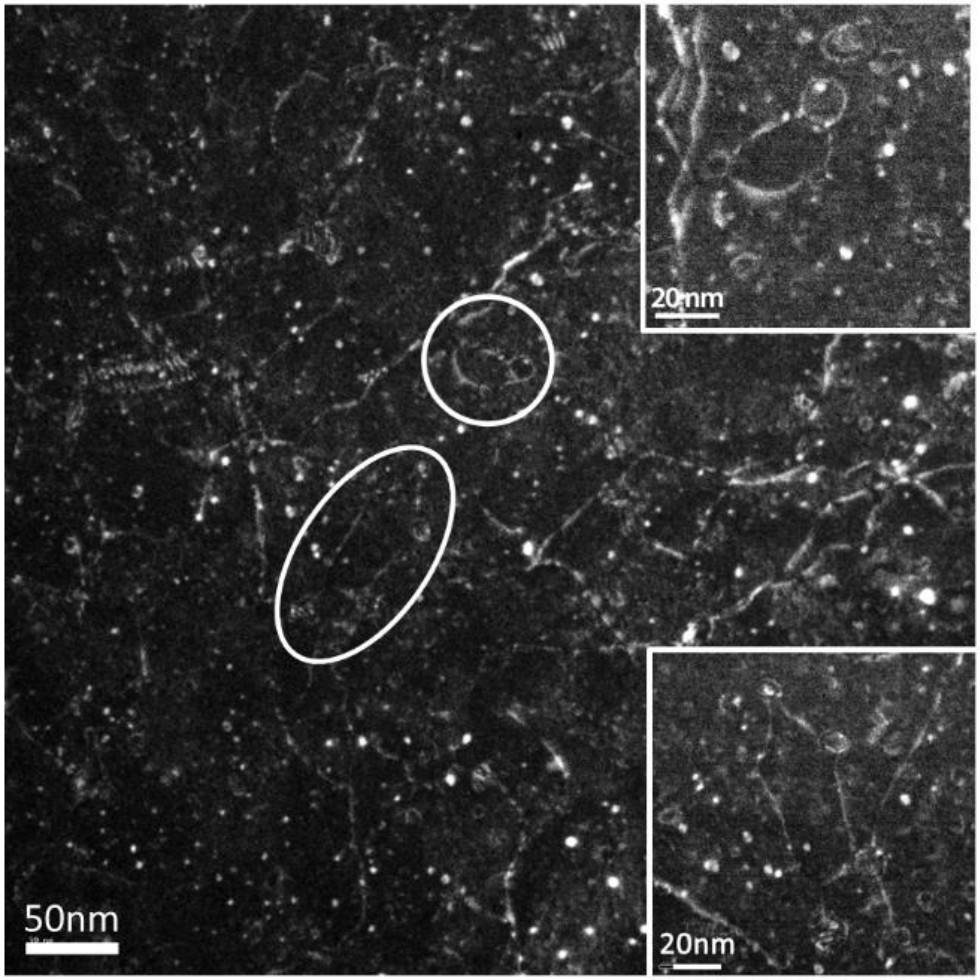

Figure 5-37. Dark field TEM images in the dendritic phase highlighting the interaction of dislocations with the precipitates by the presence of dislocation loops

The precipitate/dislocation interaction is a classic strengthening mechanisms in casting alloys in which the motion of dislocations is stopped or slowed down by the presence of precipitates. Therefore, the images shown give information about the fundamental plastic mechanisms of the ductile dendritic phase and suggest a possible way for improvement of the mechanical properties of the foam by optimizing the precipitation by specific annealing treatment.

Summary of the PLC effect characterized by nanoindentation

In this work, the presence of precipitates was shown using both TEM observations and nanoindentation. However, the nanoindentation suggests the presence of very fine precipitates or clusters not observable in thin foil presented in **Figure 5-10**. The nature and size of these precipitates could be characterized by optimizing the thin foil preparation. Thus, the plastic behavior of the cell wall could be better understood.

Additionally, the nanoindentation proved to be a good qualitative tool to characterize the microstructure because of the very local information it provides about the microstructure and possible plastic behavior.

3. Conclusion of the chapter

This chapter intended to characterize the mechanical properties of a complex composite material with various interfaces through various techniques. The structure and microstructures of the foam was characterized at different levels coupling tomography and microscopy techniques. The multiscale nature of the material was demonstrated and a highly inhomogeneous structure at all scales was revealed. Because of this multiscale structure, several techniques were used to characterize the mechanical properties of the foam.

In-situ micro X-ray Computed Tomography tests of foam samples under progressive compressive loading were carried out to study the evolution of the structure while deforming. The deformation mechanisms strongly reflected the cellular structure. The deformation

initiates in the lower density region located in the middle of the sample and propagates towards the higher density region at the base of the material.

The mechanical properties of the microstructure were characterized by using the nanoindentation cartography method on individual cell walls. First, the microstructural characterization revealed an inhomogeneous microstructure within a single cell wall. The different phases logically have dissimilar hardness values but more surprisingly, the deconvolution of the hardness data revealed dissimilar average hardness between the dendritic and eutectic aluminum inducing despite the fact that the phase diagram predict the same composition. In addition to the natural interfaces present in the material, the method developed here also revealed an interface within the ductile aluminum solid solution. The dissimilar mechanical properties could ultimately lead to complex fracture mechanisms. This work gives valuable information regarding those mechanisms.

The benefit of the nanoindentation technique was extended by looking at the indentation curve instead of only use the device as a hardness measuring technique. The instabilities on the indentation curve (i.e. PLC effect) demonstrate the presence of nano-precipitates or clusters of atoms in the aluminum phase. This phenomenon represents a material instability that results macroscopically in severe strain localization, reduction in ductility and formation of striations on the surfaces of sheet metals during forming processes. The analysis of the microstructure by TEM confirmed the presence of precipitates but their size and space distribution could not explain the instabilities. Unfortunately, the thin foil was not

appropriate for observations at a lower scale. However, evidences of dislocation interactions were found by the presence of several dislocation pinning and loops. It confirms the analysis of the indentation curve and supports the use of nanoindentation to obtain microstructural information at very low scale.

Throughout this chapter, the structures and microstructures were showed to affect the mechanical properties and at various degree to affect the macroscopic deformation of the foam. The different methods developed for the characterization of this complex composites material were successful and gave new insights on the role of the microstructural interfaces in the deformation of the foam. Without doubt, this method could be applied to other complex materials.

CHAPTER SIX

Summary and conclusions

Interfaces are responsible for many of the magnetic, electrical, optical and mechanical properties of materials. The focus of this work was to bring a novel approach in the characterization of the local mechanical properties of interfaces of two commercially available materials. The use of "real materials' as opposed to material designed in a laboratory gives more value to this work since they are usually more complex because not specifically designed for our experiments. Throughout this work, the relationship between microstructure and mechanical properties was assessed.

First, the notion of coating and adhesion was addressed by characterizing the hardness and microstructure of a 17-4PH steel substrate subjected to a grit blasting surface treatment followed by the deposition of a cermet Cr_3C_2-NiCr coating deposited by high velocity oxy-fuel (HVOF). Nanoindentation cartography and microscopy imaging of the substrate at the coating/substrate interface were performed. Cracks nucleating from the edge of residual grits were also observed suggesting that failure could preferentially occur in the layer affected by the grit blasting and not at the coating substrate interface.

Obviously, other factors could be more critical in understanding the failure of such systems. Failure in the coating or at the interface is more likely to occur. However, in a process of improving the performance of the coating, the local investigation of the impact of the substrate surface preparation is critical. In addition, in light of the results presented in this work, the nanoindentation cartography method couple to high resolution imaging techniques could enable to reinterpret the adhesion problems of thermal spray coating deposited on grit blasted substrate.

Then, the mechanical properties of a multiscale composite material were characterized. The material is an aluminum foam used in energy absorbing structure. The characterization of the foam revealed a complex multiscale microstructure. Several SEM and OM images of the microstructure illustrated the inhomogeneity of the microstructure within individual cell walls. The SiC particles distribution, dendrite size, eutectic Si platelets size and shape were shown to differ greatly. It suggests possible divergent mechanical behaviors within a single cell wall but most importantly within the entire structure.

The aluminum accounts for the ductility of the foam and its properties are critical in defining the deformation behavior of the foam. Therefore, most of the efforts were oriented towards the characterization of the ductile aluminum phases (eutectic and dendritic). The presence of silicon in solution in varying concentrations and even of silicon in the form of precipitates in the eutectic and dendritic phases resulted in different mechanical properties and an active dislocation/precipitate interaction. As a result, strain localization and

ultimately nucleation of cracks can develop at the eutectic/dendritic interface. Additionally, the unveiled PLC effect represents a material instability, which macroscopically results in severe strain localization and reduction of ductility.

This work exposed several prospects for a further characterization of the foam. The characterization of the microstructure, its evolution during plastic deformation and how it controls the mechanical properties were initiated but not completed. To do so, the cross section of foam samples was carefully polished and conventionally compressed. Because the cross section was polished, the evolution of the microstructure as the strain increase was characterized. As shown in **Figure 6-1**, slip lines inside the dendritic phase were observed. More interestingly, **Figure 6-1b** shows the slip lines propagating towards the dendritic/eutectic interface. The resolution is not enough to assess the contribution of the eutectic phase on the propagation of plasticity but experiments using atomic force microscopy at the interface would answer whether the slip lines propagates in the eutectic phase or are arrested by it.

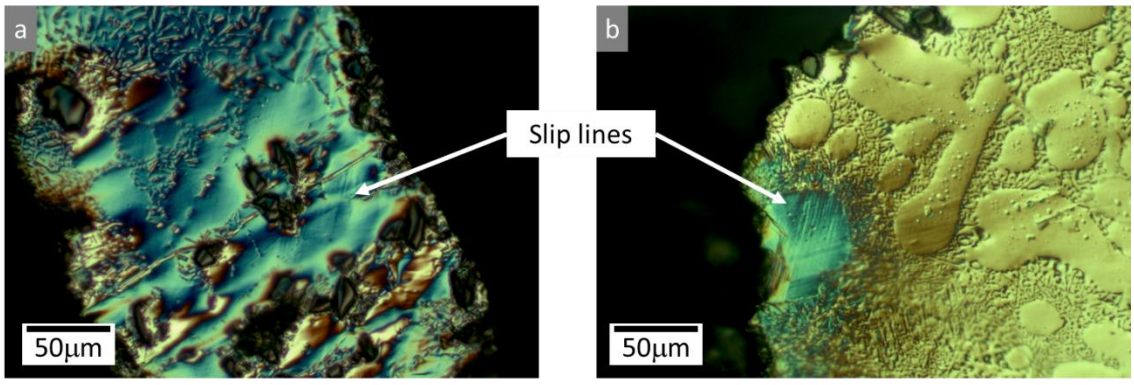

Figure 6-1. Slip lines observed in the dendritic phase after 10% compressive strain

The use of AFM could also be extended by looking at the plasticity around nanoindentation imprints and crack initiation sites. At last, the role of the SiC particles was excluded from this study but play an essential role in the propagation of cracks and their characterization would give further insights on the contribution of the microstructure to the deformation of cell walls.

To conclude, the method developed in this work showed great results even on a complex composite material like an aluminum foam. The nanoindentation cartography coupled to imaging techniques highlighted the role of the microstructure on the deformation behavior of both materials. It also confirmed the importance of locally characterize a material to understand its macroscopic behavior. Despite the complexity of the materials tested, the method proved to be versatile enough and could be implemented for other materials.

References

[1] B. Delmon, "Understanding Interfaces," in *Interfaces in New Materials*, Springer, Dordrecht, 1991, pp. 1–11.

[2] I. E. Reimanis, B. J. Dalgleish, and A. G. Evans, "The fracture resistance of a model metal/ceramic interface," *Acta Metallurgica et Materialia*, vol. 39, no. 12, pp. 3133–3141, Dec. 1991.

[3] M. D. Banea and L. F. M. da Silva, "Adhesively bonded joints in composite materials: An overview , Adhesively bonded joints in composite materials: An overview," *Proceedings of the IMechE*, vol. 223, no. 1, pp. 1–18, Jan. 2009.

[4] J. G. Williams, M. E. Donnellan, M. R. James, and W. L. Morris, "Properties of the interphase in organic matrix composites," *Materials Science and Engineering: A*, vol. 126, no. 1, pp. 305–312, Jun. 1990.

[5] C. R. F. Azevedo, "Failure analysis of a crude oil pipeline," *Engineering Failure Analysis*, vol. 14, no. 6, pp. 978–994, Sep. 2007.

[6] Interfaces in New Materials, P. Grange, B. Delmon, Université catholique de Louvain, Université catholique de Louvain, and Workshop Interfaces in New Materials, Eds., *Interfaces in new materials*. .

[7] R. Phillips, J. Kondev, and J. Theriot, *Physical Biology of the Cell*. Garland Science, 2013.

[8] R. Wiesendanger, *Scanning Probe Microscopy and Spectroscopy: Methods and Applications*. Cambridge University Press, 1994.

[9] H. S. Gupta *et al.*, "Two different correlations between nanoindentation modulus and mineral content in the bone–cartilage interface," *Journal of Structural Biology*, vol. 149, no. 2, pp. 138–148, Feb. 2005.

[10] A. Hodzic, Z. H. Stachurski, and J. K. Kim, "Nano-indentation of polymer–glass interfaces Part I. Experimental and mechanical analysis," *Polymer*, vol. 41, no. 18, pp. 6895–6905, Aug. 2000.

[11] M. A. Monclus, T. J. Young, and D. D. Maio, "AFM indentation method used for elastic modulus characterization of interfaces and thin layers," *J Mater Sci*, vol. 45, no. 12, pp. 3190–3197, Jun. 2010.

[12] G. M. Odegard, T. C. Clancy, and T. S. Gates, "Modeling of the mechanical properties of nanoparticle/polymer composites," *Polymer*, vol. 46, no. 2, pp. 553–562, Jan. 2005.

[13] M. Elices, G. V. Guinea, J. Gómez, and J. Planas, "The cohesive zone model: advantages, limitations and challenges," *Engineering Fracture Mechanics*, vol. 69, no. 2, pp. 137–163, Jan. 2002.

[14] R. Prasher, "Thermal Interface Materials: Historical Perspective, Status, and Future Directions," *Proceedings of the IEEE*, vol. 94, no. 8, pp. 1571–1586, Aug. 2006.

[15] S.-Y. Fu, X.-Q. Feng, B. Lauke, and Y.-W. Mai, "Effects of particle size, particle/matrix interface adhesion and particle loading on mechanical properties of particulate–polymer composites," *Composites Part B: Engineering*, vol. 39, no. 6, pp. 933–961, Sep. 2008.

[16] M. D. Thouiess, O. Sbaizero, L. S. Sigl, and A. G. Evans, "Effect of Interface Mechanical Properties on Pullout in a SiC-Fiber-Reinforced Lithium Aluminum Silicate Glass-Ceramic," *Journal of the American Ceramic Society*, vol. 72, no. 4, pp. 525–532.

[17] A. G. Evans, G. B. Crumley, and R. E. Demaray, "On the mechanical behavior of brittle coatings and layers," *Oxid Met*, vol. 20, no. 5–6, pp. 193–216, Dec. 1983.

[18] B. Miller, P. Muri, and L. Rebenfeld, "A microbond method for determination of the shear strength of a fiber/resin interface," *Composites Science and Technology*, vol. 28, no. 1, pp. 17–32, Jan. 1987.

[19] C.-H. Hsueh, "Interfacial debonding and fiber pull-out stresses of fiber-reinforced composites," *Materials Science and Engineering: A*, vol. 123, no. 1, pp. 1–11, Jan. 1990.

[20] "ASTM C633 - 13(2017) Standard Test Method for Adhesion or Cohesion Strength of Thermal Spray Coatings." [Online]. Available: https://www.astm.org/Standards/C633.htm. [Accessed: 19-Jul-2018].

[21] "ASTM D4541 - 17 Standard Test Method for Pull-Off Strength of Coatings Using Portable Adhesion Testers." [Online]. Available: https://www.astm.org/Standards/D4541.htm. [Accessed: 19-Jul-2018].

[22] A. L. Robertson and K. W. White, "Microscale fracture mechanisms of a Cr3C2-NiCr HVOF coating," *Materials Science and Engineering: A*, vol. 688, pp. 62–69, Mar. 2017.

[23] G. Miranda, S. Madeira, F. S. Silva, and O. Carvalho, "A nanoindentation study on Al3Ni interface of Ni reinforced aluminum-silicon composite," *Mechanics of Advanced Materials and Structures*, vol. 24, no. 10, pp. 871–874, Jul. 2017.

[24] S. S. M. Kartheek, K. V. Vamsi, B. Ravisankar, K. Sivaprasad, and S. Karthikeyan, "Microstructural and Nanoindentation Studies Across Diffusion-bonded Interfaces in Al/Cu Metal Intermetallic Laminates," *Procedia Materials Science*, vol. 6, pp. 709–715, Jan. 2014.

[25] L. Pawłowski, *The science and engineering of thermal spray coatings*. Chichester, England; Hoboken, NJ: Wiley, 2008.

[26] "About HVOF - High Velocity Oxygen Fuel and overview systems." [Online]. Available: https://www.fst.nl/systems/hvof-coating/. [Accessed: 27-Feb-2018].

[27] P. Fauchais, A. Vardelle, M. Vardelle, and M. Fukumoto, "Knowledge concerning splat formation: An invited review," *J Therm Spray Tech*, vol. 13, no. 3, pp. 337–360, Sep. 2004.

[28] V. V. Sobolev, J. M. Guilemany, J. Nutting, and S. Joshi, *High velocity oxy-fuel spraying: theory, structure-property relationships and applications*. London: Maney, 2004.

[29] J. Wigren, "Technical note: Grit blasting as surface preparation before plasma spraying," *Surface and Coatings Technology*, vol. 34, no. 1, pp. 101–108, Jan. 1988.

[30] M. Mellali, A. Grimaud, A. C. Leger, P. Fauchais, and J. Lu, "Alumina grit blasting parameters for surface preparation in the plasma spraying operation," *J Therm Spray Tech*, vol. 6, no. 2, pp. 217–227, Jun. 1997.

[31] S. Amada, T. Hirose, and T. Senda, "Quantitative evaluation of residual grits under angled blasting," *Surface and Coatings Technology*, vol. 111, no. 1, pp. 1–9, Jan. 1999.

[32] S. Kumar, G. Bae, and C. Lee, "Influence of substrate roughness on bonding mechanism in cold spray," *Surface and Coatings Technology*, vol. 304, pp. 592–605, Oct. 2016.

[33] Y.-Y. Wang, C.-J. Li, and A. Ohmori, "Influence of substrate roughness on the bonding mechanisms of high velocity oxy-fuel sprayed coatings," *Thin Solid Films*, vol. 485, no. 1, pp. 141–147, Aug. 2005.

[34] S. Barriuso, J. Chao, J. A. Jiménez, S. García, and J. L. González-Carrasco, "Fatigue behavior of Ti6Al4V and 316 LVM blasted with ceramic particles of interest for medical devices," *Journal of the Mechanical Behavior of Biomedical Materials*, vol. 30, pp. 30–40, Feb. 2014.

[35] L. Fu and D. Li, "Surface Nanocrystalline of Martensite Steel Induced by Sandblasting at High Temperature," *Adv. Eng. Mater.*, vol. 15, no. 6, pp. 476–479, Jun. 2013.

[36] X. S. Guan, Z. F. Dong, and D. Y. Li, "Surface nanocrystallization by sandblasting and annealing for improved mechanical and tribological properties," *Nanotechnology*, vol. 16, no. 12, p. 2963, 2005.

[37] M. Multigner, E. Frutos, J. L. González-Carrasco, J. A. Jiménez, P. Marín, and J. Ibáñez, "Influence of the sandblasting on the subsurface microstructure of 316LVM stainless steel: Implications on the magnetic and mechanical properties," *Materials Science and Engineering: C*, vol. 29, no. 4, pp. 1357–1360, May 2009.

[38] X. Tang and D. Y. Li, "Production of alloyed nanocrystalline surfaces by combined punching, sandblasting and recovery treatments," *Scripta Materialia*, vol. 58, no. 12, pp. 1090–1093, Jun. 2008.

[39] X. Y. Wang and D. Y. Li, "Mechanical, electrochemical and tribological properties of nano-crystalline surface of 304 stainless steel," *Wear*, vol. 255, no. 7, pp. 836–845, Aug. 2003.

[40] S. Suresh, *Fatigue of materials*. 1998.

[41] T. Hanlon, Y.-N. Kwon, and S. Suresh, "Grain size effects on the fatigue response of nanocrystalline metals," *Scripta Materialia*, vol. 49, no. 7, pp. 675–680, Oct. 2003.

[42] Y. C. Wang, F. Liang, H. F. Tan, B. Zhang, and G. P. Zhang, "Enhancing fatigue strength of high-strength ultrafine-scale Cu/Ni laminated composites," *Materials Science and Engineering: A*, vol. 714, pp. 43–48, Jan. 2018.

[43] W. Trompetter, M. Hyland, D. McGrouther, P. Munroe, and A. Markwitz, "Effect of substrate hardness on splat morphology in high-velocity thermal spray coatings," *J Therm Spray Tech*, vol. 15, no. 4, pp. 663–669, Dec. 2006.

[44] L. Lu and A. K. Dahle, "Iron-rich intermetallic phases and their role in casting defect formation in hypoeutectic Al-Si alloys," *Metall and Mat Trans A*, vol. 36, no. 3, pp. 819–835, Mar. 2005.

[45] Y. C. Lee, A. K. Dahle, D. H. StJohn, and J. E. C. Hutt, "The effect of grain refinement and silicon content on grain formation in hypoeutectic Al–Si alloys," *Materials Science and Engineering: A*, vol. 259, no. 1, pp. 43–52, Jan. 1999.

[46] P. S. Mohanty and J. E. Gruzleski, "Grain refinement mechanisms of hypoeutectic Al Si alloys," *Acta Materialia*, vol. 44, no. 9, pp. 3749–3760, Sep. 1996.

[47] H. Ye, "An overview of the development of Al-Si-Alloy based material for engine applications," *J. of Materi Eng and Perform*, vol. 12, no. 3, pp. 288–297, Jun. 2003.

[48] S. G. Shabestari, "The effect of iron and manganese on the formation of intermetallic compounds in aluminum–silicon alloys," *Materials Science and Engineering: A*, vol. 383, no. 2, pp. 289–298, Oct. 2004.

[49] L. F. Mondolfo, *Aluminum alloys: structure and properties*. London: Butterworths, 1979.

[50] F. Stadler, H. Antrekowitsch, W. Fragner, H. Kaufmann, E. R. Pinatel, and P. J. Uggowitzer, "The effect of main alloying elements on the physical properties of Al–Si foundry alloys," *Materials Science and Engineering: A*, vol. 560, pp. 481–491, Jan. 2013.

[51] J. R. Davis, *Aluminum and Aluminum Alloys*. ASM International, 1993.

[52] J. G. Kaufman and E. L. Rooy, *Aluminum Alloy Castings: Properties, Processes, and Applications*. ASM International, 2004.

[53] A. Guinier, "Structure of Age-Hardened Aluminium-Copper Alloys," *Nature*, vol. 142, no. 3595, pp. 569–570, Sep. 1938.

[54] G. D. Preston, "Structure of Age-Hardened Aluminium-Copper Alloys," *Nature*, vol. 142, no. 3595, p. 570, Sep. 1938.

[55] J. P. Lynch, L. M. Brown, and M. H. Jacobs, "Microanalysis of age-hardening precipitates in aluminium alloys," *Acta Metallurgica*, vol. 30, no. 7, pp. 1389–1395, Jul. 1982.

[56] J. L. Murray and A. J. McAlister, "The Al-Si (Aluminum-Silicon) system," *Bulletin of Alloy Phase Diagrams*, vol. 5, no. 1, p. 74, Feb. 1984.

[57] L. Liu, A. M. Samuel, F. H. Samuel, H. W. Doty, and S. Valtierra, "Characteristics of α-dendritic and eutectic structures in Sr-treated Al—Si casting alloys," *Journal of Materials Science*, vol. 39, no. 1, pp. 215–224, Jan. 2004.

[58] P. R. Goulart, J. E. Spinelli, W. R. Osório, and A. Garcia, "Mechanical properties as a function of microstructure and solidification thermal variables of Al–Si castings," *Materials Science and Engineering: A*, vol. 421, no. 1, pp. 245–253, Apr. 2006.

[59] S. Seifeddine, S. Johansson, and I. L. Svensson, "The influence of cooling rate and manganese content on the β-Al5FeSi phase formation and mechanical properties of Al–Si-based alloys," *Materials Science and Engineering: A*, vol. 490, no. 1, pp. 385–390, Aug. 2008.

[60] C. H. Cáceres, C. J. Davidson, and J. R. Griffiths, "The deformation and fracture behaviour of an Al Si Mg casting alloy," *Materials Science and Engineering: A*, vol. 197, no. 2, pp. 171–179, Jul. 1995.

[61] Z. Jefferies and R. S. Archer, *The science of metals*. New York : McGraw-Hill, 1924.

[62] J. A. Horwath and L. F. Mondolfo, "Dendritic growth," *Acta Metallurgica*, vol. 10, no. 11, pp. 1037–1042, Nov. 1962.

[63] R. E. Spear and G. R. Gardner, "Dendrite cell size," *Transactions of the American Foundrymen's Society*, vol. 71, pp. 209–215, 1963.

[64] V. Metan, K. Eigenfeld, D. Räbiger, M. Leonhardt, and S. Eckert, "Grain size control in Al–Si alloys by grain refinement and electromagnetic stirring," *Journal of Alloys and Compounds*, vol. 487, no. 1, pp. 163–172, Nov. 2009.

[65] W. D. Griffiths and D. G. McCartney, "The effect of electromagnetic stirring during solidification on the structure of Al-Si alloys," *Materials Science and Engineering: A*, vol. 216, no. 1, pp. 47–60, Oct. 1996.

[66] Q. G. Wang, "Microstructural effects on the tensile and fracture behavior of aluminum casting alloys A356/357," *Metall and Mat Trans A*, vol. 34, no. 12, pp. 2887–2899, Dec. 2003.

[67] Q. G. Wang, C. H. Caceres, and J. R. Griffiths, "Damage by eutectic particle cracking in aluminum casting alloys A356/357," *Metall and Mat Trans A*, vol. 34, no. 12, pp. 2901–2912, Dec. 2003.

[68] M. M. Makhlouf and H. V. Guthy, "The aluminum–silicon eutectic reaction: mechanisms and crystallography," *Journal of Light Metals*, vol. 1, no. 4, pp. 199–218, Nov. 2001.

[69] S. D. McDonald, K. Nogita, and A. K. Dahle, "Eutectic nucleation in Al–Si alloys," *Acta Materialia*, vol. 52, no. 14, pp. 4273–4280, Aug. 2004.

[70] P. Aladar, "Alloy," US1387900 A, 16-Aug-1921.

[71] S.-Z. Lu and A. Hellawell, "The mechanism of silicon modification in aluminum-silicon alloys: Impurity induced twinning," *MTA*, vol. 18, no. 10, pp. 1721–1733, Oct. 1987.

[72] M. Timpel *et al.*, "The role of strontium in modifying aluminium–silicon alloys," *Acta Materialia*, vol. 60, no. 9, pp. 3920–3928, May 2012.

[73] M. Makhloul, "On the Mechanism of Modification of the Aluminum-Silicon Eutectic by Strontium: The Role of Nucleation," *International Journal of Metalcasting*, vol. 4, no. 1, pp. 47–50, Jan. 2010.

[74] B. M. Thall and B. Chalmers, "Modification in aluminum-silicon alloys," *J. Inst. Met.*, vol. 78, pp. 79–97, 1949.

[75] B. M. Thall and B. Chalmers, "Modification in aluminum-silicon alloys," *J. Inst. Met.*, vol. 78, pp. 79–97, 1950.

[76] ASM International, D. M. Stefanescu, and ASM International, Eds., *ASM Handbook Volume 15: Casting - ASM International*, [10. ed.], 4. print. Materials Park, Ohio: ASM International, 1998.

[77] J. Banhart, "Manufacturing routes for metallic foams," *JOM*, vol. 52, no. 12, pp. 22–27, Dec. 2000.

[78] O. Prakash, H. Sang, and J. D. Embury, "Structure and properties of Al SiC foam," *Materials Science and Engineering: A*, vol. 199, no. 2, pp. 195–203, Aug. 1995.

[79] A. T. Alpas and J. Zhang, "Effect of SiC particulate reinforcement on the dry sliding wear of aluminium-silicon alloys (A356)," *Wear*, vol. 155, no. 1, pp. 83–104, May 1992.

[80] T. Ozben, E. Kilickap, and O. Çakır, "Investigation of mechanical and machinability properties of SiC particle reinforced Al-MMC," *Journal of Materials Processing Technology*, vol. 198, no. 1, pp. 220–225, Mar. 2008.

[81] P. R. Onck, R. van Merkerk, A. Raaijmakers, and J. T. M. De Hosson, "Fracture of open- and closed-cell metal foams," *J Mater Sci*, vol. 40, no. 22, pp. 5821–5828, Nov. 2005.

[82] L. J. Gibson and M. F. Ashby, *Cellular solids: structure and properties*. 1997.

[83] M. F. Ashby, Ed., *Metal foams: a design guide*. Boston: Butterworth-Heinemann, 2000.

[84] E. Andrews, W. Sanders, and L. J. Gibson, "Compressive and tensile behaviour of aluminum foams," *Materials Science and Engineering: A*, vol. 270, no. 2, pp. 113–124, Sep. 1999.

[85] H. Bart-Smith, A.-F. Bastawros, D. R. Mumm, A. G. Evans, D. J. Sypeck, and H. N. G. Wadley, "Compressive deformation and yielding mechanisms in cellular Al alloys determined using X-ray tomography and surface strain mapping," *Acta Materialia*, vol. 46, no. 10, pp. 3583–3592, Jun. 1998.

[86] L. J. Gibson, "Mechanical Behavior of Metallic Foams," *Annual Review of Materials Science*, vol. 30, no. 1, pp. 191–227, 2000.

[87] M. Hakamada, Y. Asao, T. Kuromura, Y. Chen, H. Kusuda, and M. Mabuchi, "Density dependence of the compressive properties of porous copper over a wide density range," *Acta Materialia*, vol. 55, no. 7, pp. 2291–2299, Apr. 2007.

[88] N. Tuncer, G. Arslan, E. Maire, and L. Salvo, "Influence of cell aspect ratio on architecture and compressive strength of titanium foams," *Materials Science and Engineering: A*, vol. 528, no. 24, pp. 7368–7374, Sep. 2011.

[89] I. Jeon and T. Asahina, "The effect of structural defects on the compressive behavior of closed-cell Al foam," *Acta Materialia*, vol. 53, no. 12, pp. 3415–3423, Jul. 2005.

[90] C. Motz and R. Pippan, "Deformation behaviour of closed-cell aluminium foams in tension," *Acta Materialia*, vol. 49, no. 13, pp. 2463–2470, Aug. 2001.

[91] I. Jeon, K. Katou, T. Sonoda, T. Asahina, and K.-J. Kang, "Cell wall mechanical properties of closed-cell Al foam," *Mechanics of Materials*, vol. 41, no. 1, pp. 60–73, Jan. 2009.

[92] S. Youssef, E. Maire, and R. Gaertner, "Finite element modelling of the actual structure of cellular materials determined by X-ray tomography," *Acta Materialia*, vol. 53, no. 3, pp. 719–730, Feb. 2005.

[93] N. Babcsan *et al.*, "Characterisation of ALUHAB Aluminium Foams with Micro-CT," *Procedia Materials Science*, vol. 4, pp. 69–74, Jan. 2014.

[94] J. Lázaro, E. Solórzano, M. A. Rodríguez-Pérez, and A. R. Kennedy, "Effect of solidification rate on pore connectivity of aluminium foams and its consequences on mechanical properties," *Materials Science and Engineering: A*, vol. 672, pp. 236–246, Aug. 2016.

[95] M. Saadatfar *et al.*, "Structure and deformation correlation of closed-cell aluminium foam subject to uniaxial compression," *Acta Materialia*, vol. 60, no. 8, pp. 3604–3615, May 2012.

[96] A. E. Markaki and T. W. Clyne, "The effect of cell wall microstructure on the deformation and fracture of aluminium-based foams," *Acta Materialia*, vol. 49, no. 9, pp. 1677–1686, May 2001.

[97] P. Schüler, R. Frank, D. Uebel, S. F. Fischer, A. Bührig-Polaczek, and C. Fleck, "Influence of heat treatments on the microstructure and mechanical behaviour of open cell AlSi7Mg0.3 foams on different lengthscales," *Acta Materialia*, vol. 109, pp. 32–45, May 2016.

[98] M. A. Islam *et al.*, "Investigation of microstructural and mechanical properties of cell walls of closed-cell aluminium alloy foams," *Materials Science and Engineering: A*, vol. 666, pp. 245–256, Jun. 2016.

[99] E. W. Andrews, G. Gioux, P. Onck, and L. J. Gibson, "Size effects in ductile cellular solids. Part II: experimental results," *International Journal of Mechanical Sciences*, vol. 43, no. 3, pp. 701–713, Dec. 2001.

[100] R. Steiner, *ASM Handbook, Volume 1: Properties and Selection: Irons, Steels, and High-Performance Alloys*. A S M International, 1990.

[101] L. Salvo *et al.*, "X-ray micro-tomography an attractive characterisation technique in materials science," *Nuclear Instruments and Methods in Physics Research Section B: Beam Interactions with Materials and Atoms*, vol. 200, pp. 273–286, Jan. 2003.

[102] S. R. Stock, "Recent advances in X-ray microtomography applied to materials," *International Materials Reviews*, vol. 53, no. 3, pp. 129–181, May 2008.

[103] B. K. Bay, T. S. Smith, D. P. Fyhrie, and M. Saad, "Digital volume correlation: Three-dimensional strain mapping using X-ray tomography," *Experimental Mechanics*, vol. 39, no. 3, pp. 217–226, Sep. 1999.

[104] H. Toda, E. Maire, S. Yamauchi, H. Tsuruta, T. Hiramatsu, and M. Kobayashi, "In situ observation of ductile fracture using X-ray tomography technique," *Acta Materialia*, vol. 59, no. 5, pp. 1995–2008, Mar. 2011.

[105] E. Ferrié, J.-Y. Buffière, W. Ludwig, A. Gravouil, and L. Edwards, "Fatigue crack propagation: In situ visualization using X-ray microtomography and 3D simulation using the extended finite element method," *Acta Materialia*, vol. 54, no. 4, pp. 1111–1122, Feb. 2006.

[106] R. Ketcham, *X-ray Computed Tomography (CT)*. [Online]. Available: https://serc.carleton.edu/research_education/geochemsheets/techniques/CT.html.

[107] J. L. Hay and G. M. Pharr, "Instrumented Indentation Testing," in *ASM Handbook, Volume 8: Mechanical Testing and Evaluation*, A S M International, 2000, pp. 232–243.

[108] I. N. Sneddon, "The relation between load and penetration in the axisymmetric boussinesq problem for a punch of arbitrary profile," *International Journal of Engineering Science*, vol. 3, no. 1, pp. 47–57, May 1965.

[109] R. B. King, "Elastic analysis of some punch problems for a layered medium," *International Journal of Solids and Structures*, vol. 23, no. 12, pp. 1657–1664, Jan. 1987.

[110] J. Woirgard and J.-C. Dargenton, "An alternative method for penetration depth determination in nanoindentation measurements," *Journal of Materials Research*, vol. 12, no. 9, pp. 2455–2458, Sep. 1997.

[111] G. M. Pharr and A. Bolshakov, "Understanding nanoindentation unloading curves," *Journal of Materials Research*, vol. 17, no. 10, pp. 2660–2671, Oct. 2002.

[112] F.-J. Ulm, M. Vandamme, C. Bobko, J. A. Ortega, K. Tai, and C. Ortiz, "Statistical Indentation Techniques for Hydrated Nanocomposites: Concrete, Bone, and Shale," *Journal of the American Ceramic Society*, vol. 90, no. 9, pp. 2677–2692, Sep. 2007.

[113] C. Tromas, J. C. Stinville, C. Templier, and P. Villechaise, "Hardness and elastic modulus gradients in plasma-nitrided 316L polycrystalline stainless steel investigated by nanoindentation tomography," *Acta Materialia*, vol. 60, no. 5, pp. 1965–1973, Mar. 2012.

[114] N. X. Randall, M. Vandamme, and F.-J. Ulm, "Nanoindentation analysis as a two-dimensional tool for mapping the mechanical properties of complex surfaces," *Journal of Materials Research*, vol. 24, no. 3, pp. 679–690, Mar. 2009.

[115] C. Tromas, M. Arnoux, and X. Milhet, "Hardness cartography to increase the nanoindentation resolution in heterogeneous materials: Application to a Ni-based single-crystal superalloy," *Scripta Materialia*, vol. 66, no. 2, pp. 77–80, Jan. 2012.

[116] J. Goldstein, Ed., *Scanning electron microscopy and X-ray microanalysis: a text for biologists, materials scientists, and geologists*, 2nd ed. New York: Plenum Press, 1992.

[117] G. C. Soltz, "The Effect of Substrate Contaminates on the Life of Epoxy Coatings Submerged in Sea Water:," Defense Technical Information Center, Fort Belvoir, VA, Mar. 1991.

[118] A. W. Momber, *Blast cleaning technology*. Berlin: Springer Verlag, 2008.

[119] M. Multigner *et al.*, "Superficial severe plastic deformation of 316 LVM stainless steel through grit blasting: Effects on its microstructure and subsurface mechanical properties," *Surface and Coatings Technology*, vol. 205, no. 7, pp. 1830–1837, Dec. 2010.

[120] T. S. Price, P. H. Shipway, and D. G. McCartney, "Effect of cold spray deposition of a titanium coating on fatigue behavior of a titanium alloy," *J Therm Spray Tech*, vol. 15, no. 4, pp. 507–512, Dec. 2006.

[121] M. Baleani, M. Viceconti, and A. Toni, "The Effect of Sandblasting Treatment on Endurance Properties of Titanium Alloy Hip Prostheses," *Artificial Organs*, vol. 24, no. 4, pp. 296–299, Apr. 2000.

[122] R. N. Caron and G. Krauss, "The tempering of Fe-C lath martensite," *MT*, vol. 3, no. 9, pp. 2381–2389, Sep. 1972.

[123] G. Krauss and A. R. Marder, "The morphology of martensite in iron alloys," *Metallurgical Transactions*, vol. 2, no. 9, pp. 2343–2357, Sep. 1971.

[124] S. Morito, H. Tanaka, R. Konishi, T. Furuhara, and T. Maki, "The morphology and crystallography of lath martensite in Fe-C alloys," *Acta Materialia*, vol. 51, no. 6, pp. 1789–1799, Apr. 2003.

[125] M. Gross and L. Motivans, "Bimetallic MIM Medical Components - ASM International," in *Medical Device Materials*, 2004, pp. 403–407.

[126] P.-H. Gao, C.-J. Li, G.-J. Yang, Y.-G. Li, and C.-X. Li, "Influence of substrate hardness on deposition behavior of single porous WC-12Co particle in cold spraying," *Surface and Coatings Technology*, vol. 203, no. 3, pp. 384–390, Nov. 2008.

[127] J. W. M. Jr, C. Kinney, K. Pytlewski, and Y. Adachi, "Microstructure and cleavage in lath martensitic steels," *Sci. Technol. Adv. Mater.*, vol. 14, no. 1, p. 014208, 2013.

[128] X. Mao, D. Li, Z. Wang, X. Zhao, and L. Cai, "Surface nanocrystallization by mechanical punching process for improving microstructure and properties of Cu-30Ni alloy,"

Transactions of Nonferrous Metals Society of China, vol. 23, no. 6, pp. 1694–1700, Jun. 2013.

[129] D. Tumbajoy-Spinel *et al.*, "Assessment of mechanical property gradients after impact-based surface treatment: application to pure α-iron," *Materials Science and Engineering: A*, vol. 667, pp. 189–198, Jun. 2016.

[130] X. Wu, N. Tao, Y. Hong, B. Xu, J. Lu, and K. Lu, "Microstructure and evolution of mechanically-induced ultrafine grain in surface layer of AL-alloy subjected to USSP," *Acta Materialia*, vol. 50, no. 8, pp. 2075–2084, May 2002.

[131] K. Lu and J. Lu, "Nanostructured surface layer on metallic materials induced by surface mechanical attrition treatment," *Materials Science and Engineering: A*, vol. 375–377, pp. 38–45, Jul. 2004.

[132] J. T. BEALS and M. S. THOMPSON, "Density gradient effects on aluminium foam compression behaviour," p. 6.

[133] R. Surace, D. Filippis, L. A. C, E. Niini, A. D. Ludovico, and J. Orkas, "Morphological Investigation of Foamed Aluminum Parts Produced by Melt Gas Injection," *Advances in Materials Science and Engineering*, 2009. [Online]. Available: https://www.hindawi.com/journals/amse/2009/506024/. [Accessed: 11-Jun-2018].

[134] D. P. H. Hasselman and R. M. Fulrath, "Effect of Small Fraction of Spherical Porosity on Elastic Moduli of Glass," *Journal of the American Ceramic Society*, vol. 47, no. 1, pp. 52–53.

[135] A. R. Boccaccini, G. Ondracek, and E. Mombello, "Determination of stress concentration factors in porous materials," *JOURNAL OF MATERIALS SCIENCE LETTERS*, vol. 14, pp. 534–536, 1995.

[136] D. Bouchard and J. S. Kirkaldy, "Prediction of dendrite arm spacings in unsteady- and steady-state heat flow of unidirectionally solidified binary alloys," *Metallurgical and Materials Transactions B*, vol. 28, no. 4, pp. 651–663, Aug. 1997.

[137] M. Bamberger, B. Z. Weiss, and M. M. Stupel, "Heat flow and dendritic arm spacing in chill-cast Al–Si alloys," *Materials Science and Technology*, vol. 3, no. 1, pp. 49–56, Jan. 1987.

[138] A. Claverie and N. Cherkashin, "On the origin of dislocation loops in irradiated materials: A point of view from silicon," *Nuclear Instruments and Methods in Physics Research Section B: Beam Interactions with Materials and Atoms*, vol. 374, pp. 82–89, May 2016.

[139] Z. Yang, N. Sakaguchi, S. Watanabe, and M. Kawai, "Dislocation Loop Formation and Growth under *In Situ* Laser and/or Electron Irradiation," *Scientific Reports*, vol. 1, p. 190, Dec. 2011.

[140] P. Lv, Z. Zhang, X. Wang, X. Hou, and Q. Guan, "Blue photoluminescent Si nanocrystals prepared by high-current pulsed electron beam irradiation," *RSC Adv.*, vol. 3, no. 39, pp. 17998–18001, Sep. 2013.

[141] G. M. Pharr, W. C. Oliver, and D. S. Harding, "New evidence for a pressure-induced phase transformation during the indentation of silicon," *Journal of Materials Research*, vol. 6, no. 6, pp. 1129–1130, Jun. 1991.

[142] A. Kailer, Y. G. Gogotsi, and K. G. Nickel, "Phase transformations of silicon caused by contact loading," *Journal of Applied Physics*, vol. 81, no. 7, pp. 3057–3063, Apr. 1997.

[143] S. Murali, K. S. Raman, and K. S. S. Murthy, "Effect of Iron Impurity and a Cd Trace Addition on the Delayed Ageing of Al-7Si-0.3 Mg Casting Alloy," *Cast Metals*, vol. 4, no. 1, pp. 31–36, Jan. 1991.

[144] A. T. Joenoes and J. E. Gruzleski, "Magnesium Effects on the Microstructure of Unmodified and Modified Al-Si Alloys," *Cast Metals*, vol. 4, no. 2, pp. 62–71, Apr. 1991.

[145] C.-L. Chen, A. Richter, and R. C. Thomson, "Mechanical properties of intermetallic phases in multi-component Al–Si alloys using nanoindentation," *Intermetallics*, vol. 17, no. 8, pp. 634–641, Aug. 2009.

[146] J. T. M. De Hosson *et al.*, "In situ TEM nanoindentation and dislocation-grain boundary interactions: a tribute to David Brandon," *Journal of Materials Science*, vol. 41, no. 23, pp. 7704–7719, Dec. 2006.

[147] H. Ovri and E. T. Lilleodden, "New insights into plastic instability in precipitation strengthened Al–Li alloys," *Acta Materialia*, vol. 89, pp. 88–97, May 2015.

[148] Z. Kovacs, N. Q. Chinh, and J. Lendvai, "Portevin–Le Chaˆtelier type plastic instabilities in depth sensing macro-indentation_," *Materials Science and Engineering A*, p. 6, 2002.

[149] B. Gan and S. Tin, "Compositional dependence of serrated flow in nickel binary solid solutions during high-temperature microindentation," *Philosophical Magazine*, vol. 94, no. 17, pp. 1982–1991, Jun. 2014.

[150] H. Ovri and E. T. Lilleodden, "Temperature dependence of plastic instability in Al alloys: A nanoindentation study," *Materials & Design*, vol. 125, pp. 69–75, Jul. 2017.

Appendix A - Investigation of the Mg content on the nanoindentation measurement

In an effort to characterize the complex microstructure of the aluminum foam, a study of the effect of Mg content was initiated. To do so, a map of Mg content was made using the same method explained in chapter 4 for the Si content (based on individual EDS scans - see page 145 for the results on Si content). The EDS measurements were then coupled with nanoindentation results obtained from the nanoindentation cartography method. The maps shown in **Figure A-1** were made on a longitudinal section of a primary dendritic arm. This configuration allows exploring the role of the crystallographic orientation of the dendrite on the hardness and Mg content measurements. The step size of the indentations array was chosen larger at 5µm and the maximum penetration depth is 150nm. The different dendritic arms were numbered from 1 to 7 (see **Figure A-1a**) and will be referred by their number in the rest of the section.

The hardness map is illustrated in **Figure A-1b**. In the arms 1, 2, 3 and 4, the hardness is distributed homogeneously ranging between 1200 and 1700MPa. In the arms 5, 6 and 7, the hardness actually follows the opposite trend compared to what was presented in **Figure 5-27**. The hardness is higher at the edge of the dendrite compared to the core. As illustrated

by **Figure A-1e**, it arises from the presence of Mg rich precipitates. Those precipitates are easily discernable on the optical micrograph in **Figure A-1a**. Their chemical composition was confirmed by EDS as seen in **Figure A-1e** in which the yellow color corresponds to where Mg was detected.

The influence of Mg was illustrated. The presence of Mg in the solid solution increases the hardness measurements up to 1700MPa. From the EDS measurements, it seems that magnesium is not present uniformly in the Al solid solution. Instead, Mg preferably precipitates Mg traces are only found around those precipitates. Moreover, an effect of the dendritic crystallographic orientation could explain the different distribution of hardness observed in **Figure 5-27** and **Figure A-1**. Obviously, the optical images showed in **Figure 5-27** and **Figure A-1** illustrate two configurations of the dendritic phase. Moreover, the formation of a dendrite is a complex process involving the diffusion of atoms during solidification. Therefore, the distribution of hardness could be the result of silicon being distributed preferentially.

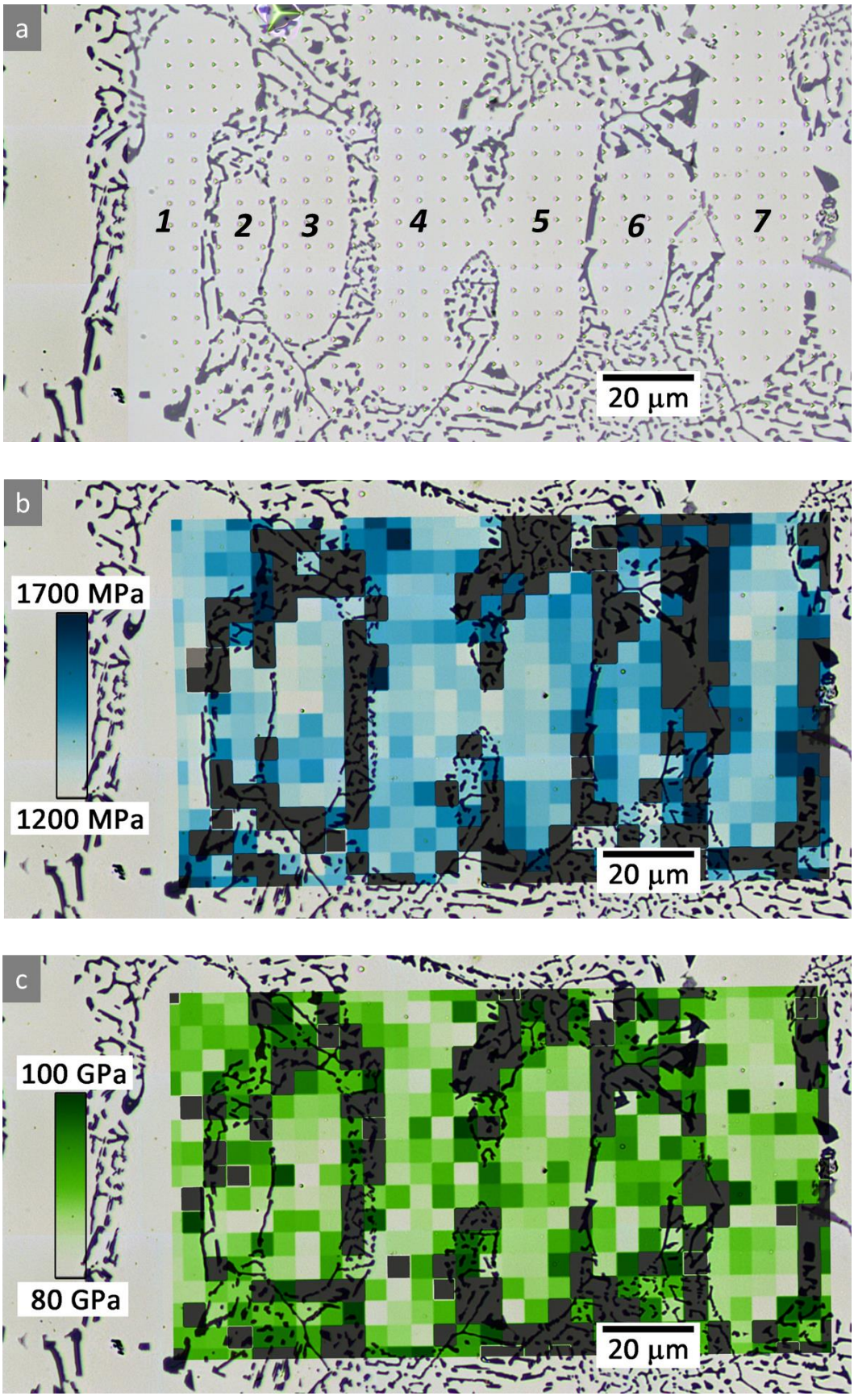
a
1
2
3
4
5
6
7
20 µm
b
1700 MPa
1200 MPa
20 µm
c
100 GPa
80 GPa
20 µm

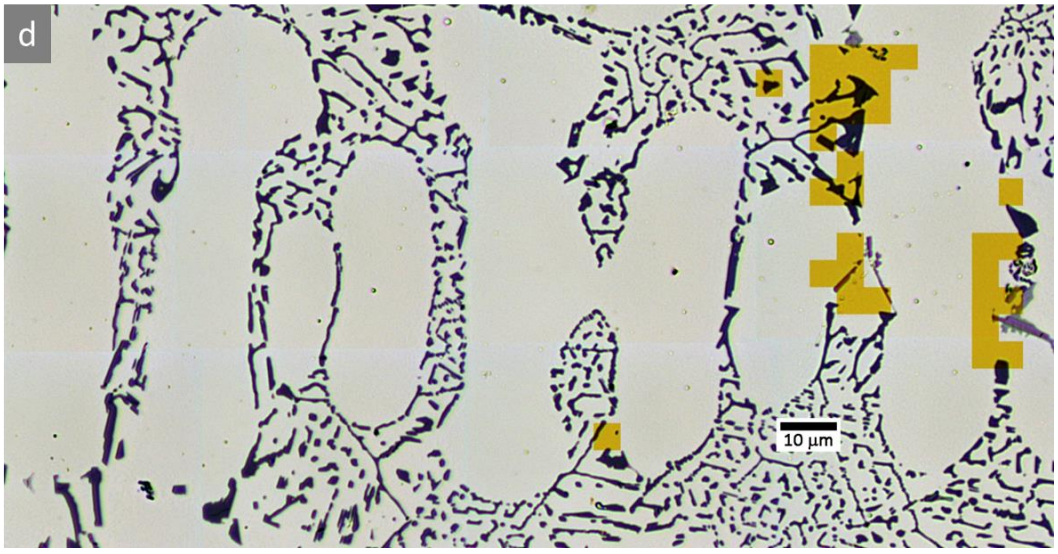

Figure A-1. Results of the investigation of the effect of Mg on the hardness measurements. (a) Optical micrograph of the surface after indentation. The array is constituted of 17x30 indentations. The step size is 5um. (b) Nanohardness map (c) Young's modulus map (d) Mg map.